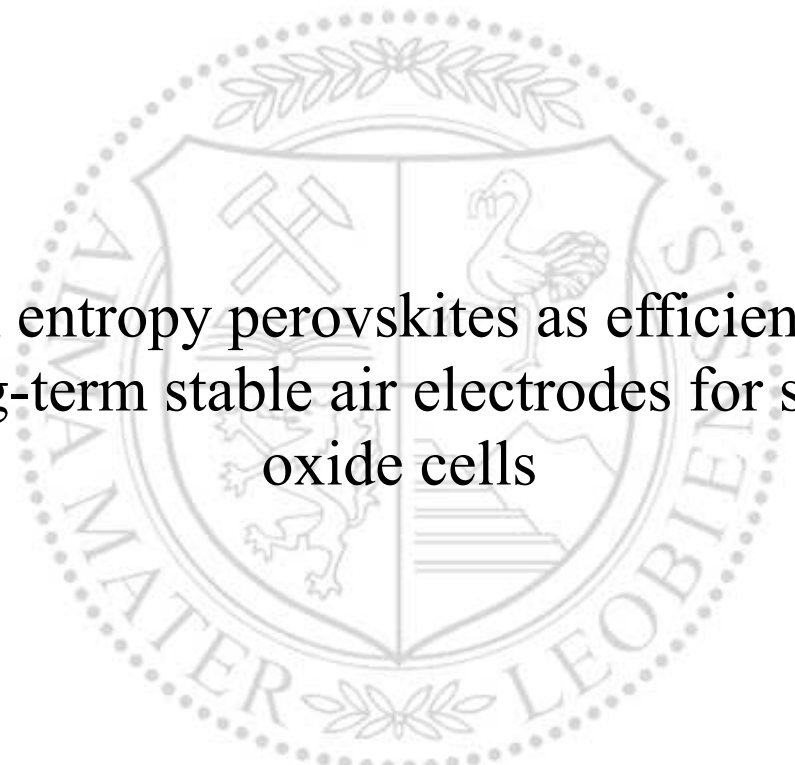Chair of Physical Chemistry

Doctoral Thesis

High entropy perovskites as efficient and long-term stable air electrodes for solid oxide cells

Dipl.-Ing. Patrick Pretschuh, BSc

June 2024

**EIDESSTATTLICHE ERKLÄRUNG**

Ich erkläre an Eides statt, dass ich diese Arbeit selbstständig verfasst, andere als die angegebenen Quellen und Hilfsmittel nicht benutzt, den Einsatz von generativen Methoden und Modellen der künstlichen Intelligenz vollständig und wahrheitsgetreu ausgewiesen habe, und mich auch sonst keiner unerlaubten Hilfsmittel bedient habe.

Ich erkläre, dass ich den Satzungsteil „Gute wissenschaftliche Praxis" der Montanuniversität Leoben gelesen, verstanden und befolgt habe.

Weiters erkläre ich, dass die elektronische und gedruckte Version der eingereichten wissenschaftlichen Abschlussarbeit formal und inhaltlich identisch sind.

Datum  29.06.2024

Unterschrift Verfasser/in
Patrick Pretschuh

# Acknowledgements

I would like to thank all my colleagues at the Chair of Physical Chemistry and the project team at Materials Center Leoben Forschung GmbH for the continuous support during the thesis and the fruitful discussions about and beyond all research topics.

My special thanks go to my supervisors Edith Bucher and Andreas Egger for their excellent expertise, guidance and advice. I am honoured to have conducted the research for this thesis in their research group. Besides these two, many others, who will receive my thanks personally, contributed to the success of the thesis.

# Abstract

Solid oxide cells (SOC) are a key technology for large-scale green hydrogen production due to their high efficiency. However, widespread commercial application faces considerable challenges. In particular, these are challenges in achieving simultaneously long-term stability and high performance, which affects cost efficiency. The key component of the technology that links both properties is the air electrode. High performance materials often suffer from chemical instability and are prone to react with impurities in the air stream or other cell components. There are also morphological challenges, particularly in electrolysis mode, with delamination of the air electrode layer due to increased interfacial oxygen partial pressures. The search for more stable electrodes that exhibit fast oxygen exchange kinetics and high electronic conductivity remains one of the key priorities towards technology industrialization.

This thesis investigates high entropy perovskites (HEP) as air electrode materials for SOC, focusing primarily on the solid oxide electrolysis cell (SOEC) mode of operation. The air electrode is tailored to replace the critical element cobalt with the sustainable and cost effective element iron, while maintaining chemical stability and high power densities. Structural analysis provides insights into phase purity and crystal structure using X-ray powder diffraction and Rietveld refinement. Oxygen exchange kinetics and electrical dc-conductivity are analyzed by 4-point dc-conductivity (relaxation) experiments. Electrochemical performance is assessed by cell tests including current density-voltage curves and electrochemical impedance spectroscopy. Results are correlated with advanced analyses of the cell components' morphology and elemental distribution by field emission scanning electron microscope (FESEM) and energy dispersive X-ray (EDX) imaging. Long-term tests with 5x5 cm² cells are carried out to assess the stability of the air electrode under application-relevant conditions.

The results of the thesis confirm the long-term stability of HEP as air electrodes in SOEC mode and its potential to outperform state of the art equivalents. It is successfully demonstrated that full cells with $La_{0.2}Pr_{0.2}Nd_{0.2}Sm_{0.2}Sr_{0.2}CoO_{3-\delta}$ (LPNSSC) and $La_{0.2}Pr_{0.2}Nd_{0.2}Sm_{0.2}Sr_{0.2}FeO_{3-\delta}$ (LPNSSF) air electrodes can be maintained in electrolysis mode for several hundred hours at constant, high electrolysis currents. After a run-in phase, LPNSSF shows a continuous degradation of 0.8% 1,000 $h^{-1}$, while LPNSSC exhibits constant cell voltage during the individual test phases. Compared to the state of the art air electrode material $La_{0.6}Sr_{0.4}CoO_{3-\delta}$, LPNSSC shows less formation of secondary phases, no delamination and higher current densities at same test conditions.

Trends in oxygen exchange kinetics and electronic conductivity are discussed with respect to the influence of temperature, oxygen partial pressure, and cobalt-to-iron substitution. These fundamental insights on mass- and charge transport properties are used to improve electrode performance of LPNSSF by an innovative composite/current-collector approach. The results of this thesis highlight the potential of HEP as promising air electrode materials for SOC and are an incentive for further research into this class of materials to advance production of green hydrogen.

# Kurzfassung

Festoxidzellen (SOC) sind aufgrund ihres hohen Wirkungsgrades eine Schlüsseltechnologie für die großtechnische Erzeugung von grünem Wasserstoff. Hinsichtlich der breiten kommerziellen Anwendung der Technologie stellen sich jedoch große Herausforderungen. Diese betreffen vor allem die gleichzeitige Erreichung von Langzeitstabilität und hohen Leistungen, was sich auf die Kosteneffizienz auswirkt. Die Schlüsselkomponente der Technologie, die beide Eigenschaften miteinander verbindet, ist die Luftelektrode. Hochleistungsmaterialien leiden oft unter chemischer Instabilität und reagieren leicht mit Verunreinigungen im Luftstrom oder anderen Zellkomponenten. Außerdem gibt es morphologische Probleme, insbesondere im Elektrolysebetrieb, bei dem die Luftelektrodenschicht aufgrund erhöhter Sauerstoffpartialdrücke an der Grenzfläche delaminiert. Die Suche nach stabileren Elektroden, die eine rasche Sauerstoffaustauschkinetik und eine hohe elektronische Leitfähigkeit aufweisen, bleibt eine der wichtigsten Prioritäten auf dem Weg zur Industrialisierung der Technologie.

In dieser Arbeit werden hochentropiestabilisierte Perowskite (HEP) als Luftelektrodenmaterialien für SOC untersucht, wobei der Forschungsschwerpunkt auf dem Elektrolysemodus (SOEC) zur Wasserstofferzeugung liegt. Gleichzeitig wird der Ansatz verfolgt Kobalt, welches als kritischer und kostenintensiver Rohstoff gilt durch Eisen zu ersetzen. Dabei sollen hohe Leistungsdichten erhalten bleiben und die chemische Stabilität verbessert werden. Synthetisierte neue Materialien werden mittels Röntgenpulver-diffraktometrie und Rietveld-Verfeinerung hinsichtlich ihrer Phasenreinheit untersucht. Die weitere Charakterisierung umfasst die Sauerstoffaustauschkinetik, welche zusammen mit der elektronischen Leitfähigkeit mittels 4-Punkt-Gleichstromleitfähigkeits-(Relaxations-)Experimenten bestimmt wird. Zelltests dienen zur Bestimmung der elektrochemischen Leistung über Stromdichte-Spannungs-Kennlinien und elektrochemischer Impedanzspektro-skopie. Die Ergebnisse werden mit Morphologienalysen mittels Feldemissions-Raster-elektronenmikroskop (FESEM) und energiedispersiver Röntgenspektroskopie (EDX) zur Analyse der Elementverteilung korreliert. Um die Stabilität der Luftelektrode unter anwendungsrelevanten Bedingungen zu beurteilen, werden Langzeittests mit 5x5 cm² Zellen durchgeführt.

Die Ergebnisse der Arbeit bestätigen die Langzeitstabilität von HEP als Luftelektroden im Elektrolysebetrieb und ihr Potenzial, den Stand der Technik zu übertreffen. Es wird gezeigt, dass hohe Leistungsdichten mit Vollzellen mit $La_{0.2}Pr_{0.2}Nd_{0.2}Sm_{0.2}Sr_{0.2}CoO_{3-\delta}$ (LPNSSC) und $La_{0.2}Pr_{0.2}Nd_{0.2}Sm_{0.2}Sr_{0.2}FeO_{3-\delta}$ (LPNSSF) Luftelektroden für mehrere hundert Stunden aufrechterhalten werden können. LPNSSF zeigt nach einer Einlaufphase eine kontinuierliche Degradation von 0,8% 1.000 $h^{-1}$, während LPNSSC eine weitgehend konstante Zellspannung aufweist. Im Vergleich zum Standardmaterial $La_{0.6}Sr_{0.4}CoO_{3-\delta}$, zeigt LPNSSC bei gleichen Testbedingungen eine geringere Tendenz zur Bildung von Sekundärphasen, keine Delamination und höhere Stromdichten.

Trends in der Sauerstoffaustauschkinetik und der elektronischen Leitfähigkeit werden im Hinblick auf den Einfluss von Temperatur, Sauerstoffpartialdruck und Kobalt-Eisen-Substitution diskutiert. Diese grundlegenden Erkenntnisse werden genutzt, um die Elektrodenleistung von LPNSSF durch einen innovativen Ansatz über die Verwendung von Kompositen bzw. Stromsammlerschichten zu verbessern. Die Ergebnisse dieser Arbeit unterstreichen das Potenzial von HEP als Luftelektrodenmaterialien für SOC und sind ein Anreiz für weitere Forschungsarbeiten zu dieser Materialklasse, um die Produktion von grünem Wasserstoff voranzutreiben.

# Table of contents

# 1  Introduction

Global economic regions are beginning to establish the first hydrogen industries. With the availability of the resource at competitive prices, demand will naturally rise. Initially, hydrogen from fossil sources - referred to as gray, blue, or turquoise hydrogen - could be available in larger quantities. However, only green hydrogen, per definition obtained from the electrolysis of water using renewable energy, is sustainable and emission-free. Solid oxide electrolysis could become the primary technique for hydrogen production for several reasons. The main advantages are high efficiency and fast kinetics. These factors are attributed to the high operating temperatures of up to 800°C, which however also pose technical challenges. The scientific background behind this is examined in detail in the thesis. The more efficient an electrolysis system is, the more economically it can be operated, as the raw material requirement per installed kW of electrolysis power decreases. Of course, this presupposes that the use of critical and cost-intensive raw materials can be kept low. As the electrolysis power increases, the challenge of hydrogen storage also decreases, since the energy carrier could be produced on demand for some industrial applications.

Innovative materials must be developed with a focus on the core topics of solid oxide electrolysis cell technology: power density, long-term stability, and substitution of critical raw materials. As a key component of the cell, the air electrode should be addressed. Delamination of the air electrode is a critical degradation mechanism for SOECs that concerns long-term stability. It is induced by elevated internal oxygen pressure near the interface of the air electrode with the electrolyte. Furthermore, strontium (Sr) segregation represents one of the primary causes of air electrode degradation in state of the art perovskites. In recent years, interest in a relatively new material class has grown: high entropy stabilized perovskites. In this approach, five or more elements are incorporated into the A and/or B-site of the perovskite structure ($ABO_3$). This material class is supposed to show particular stability, which could be induced by the distortion of the crystal lattice. To achieve high process efficiency, the air electrode material must exhibit fast oxygen exchange kinetics, along with adequate ionic and electronic conductivities. New material classes could, in principle, exhibit properties or trends regarding elemental composition that may deviate from known correlations. However, it can be assumed that, similar to state of the art (low entropy) perovskite air electrodes, the critical element cobalt (Co) on the B-site of the crystal structure will promote cell performance.

Nonetheless, systematic experimental validation and a deeper understanding of the structure-property relationships are required, given the limited availability of material data for HEP. In the direction of utilizing more sustainable raw materials and improving cost effectiveness, this thesis investigates the cell performance and material characteristics in regard of oxygen exchange kinetics and electronic conductivity with progressive substitution of Co by Fe. In long-term tests under application-relevant conditions, the stability of the air electrode is evaluated, and its performance is correlated with the air electrode morphology. The results are compared with state of the art electrodes.

# 2 Scope of the thesis

The aim of this thesis was to develop highly efficient and long-term stable solid oxide cell air electrodes by application of the novel material class of high entropy perovskites. Common failure mechanisms, especially those occurring in electrolysis mode, should be avoided through optimized elemental composition and innovative developments in electrode morphology and cell design. The achieved highest performance should finally be maintained as much as possible when substituting critical elements from the perovskite structure with sustainable and cost effective raw materials.

The research work began with an intensive literature research on solid oxide cells, their power densities, degradation mechanisms of the air electrode, and the properties of high entropy stabilized perovskites. The results of the literature review are summarized in Chapter 3. It was decided that developments in HEP should be based on state of the art electrode materials. This provided the necessary amount of comparative data from the literature, which allowed the performance of the new developments to be assessed. With consideration of the objectives of the work, three central research questions were defined:

*Research question 1: Do air electrodes based on high entropy perovskites prove long-term stable in SOEC operation mode?*

*Research question 2: Can air electrodes based on high entropy perovskites outperform their state of the art (low entropy) analogs?*

*Research question 3: Which trends in oxygen exchange kinetics and electronic conductivity do the high entropy perovskites in concern show when substituting Co with Fe?*

A customized process flow was developed to make the methodology of the research work as efficient and structured as possible. This is presented in Chapter 4 and explained via use cases.

Chapter 5 summarizes and evaluates the obtained results, and provides answers to the research questions presented above.

# 3  Fundamentals

## 3.1  Solid oxide cell technology

This chapter discusses the global use of hydrogen and its role in various industries. Additionally, it explains how SOEC technology is considered a promising method for hydrogen production due to its high operating temperatures and associated high kinetic efficiency. Finally, the operating principles of SOECs as well as their challenges and opportunities for the future are described.

### 3.1.1  Necessity and superiority

The global use of hydrogen has steadily increased from 18.5 Mt in 1975 to 95 Mt in 2022 [1,2]. The chemical industry needs it as feedstock for the production. Hydrogen serves as a key component in various high-volume chemicals, whether in organic or inorganic forms. It is utilized as a reactant, either in molecular form or bound within molecules, to facilitate obtaining desired products. A significant global process involving hydrogen is the production of ammonia for nitrogen-based fertilizers. Ammonia, as a carbon-free energy carrier, is being considered as a promising substitute for traditional hydrogen storage systems. In addition to its role as a reactant, hydrogen functions as a reduction agent in various industrial sectors, including the chemical and metals industries. It aids in converting precursor molecules, alloys, or ores into the desired end products [3]. The blast furnace route accounts for over 80% of ore-based steel production and consumes around 18 GJ t$^{-1}$ of energy derived from coal. It exhibits an emission intensity of roughly 1870 kg $CO_2$ per ton of liquid steel, taking into account pellet making, steel rolling, and finishing steps [4]. Depending on calculation basis, the steel sector is responsible for at least 7% of global anthropogenic $CO_2$ emission. Beside carbon capture and storage, hydrogen provides the only sustainable way of reducing ores [5]. Thereby many process routes are currently in development, while the usage of hydrogen in the iron and steel subsector currently already accounts for 10% of the total industrial demand [6,7]. Taking into account the possibilities in mobility and power generation sector as well, the future demand for hydrogen is expected to rise up to 500 Mt per year in 2050 [2].

Globally, hydrogen is presently predominantly produced through steam reforming of natural gas and petroleum, or by coal gasification. These methods, which are based on fossil raw materials, cover the majority of the world's hydrogen requirements [8]. The remaining amount is derived from refineries and conversion processes. In fact, production from water electrolysis was only about 0.1% of the global production in 2022. This emphasizes that low carbon emission production is still in its infancy. However, the installed capacity and the quantity of announced projects have been experiencing rapid growth in recent years. As of the year 2022, the worldwide installed capacity of water electrolysers for hydrogen production had nearly reached 700 MW. The alkaline electrolysers comprised 60% of the installed capacity, and proton exchange membrane (PEM) electrolysers representing approximately 30% [2]. According to projections, there is an anticipated shift in the next few years, where PEM electrolysers are expected to gain market share comparable to alkaline electrolysers. However, for numerous upcoming projects the final decision about the electrolyser technology

has not been published. Presently, SOEC account for less than 1% of the installed capacity [3,8].

Nevertheless, the SOEC technology shows some features that will favor that technique for high volume hydrogen production. While in theory all the production technologies would be able to exhibit the same efficiency, SOEC benefits from its high operational temperatures of 600 – 850 °C in sense of kinetics. Electrolysers can be operated in thermoneutral condition, which means the system produces just enough thermal energy, so that the endothermic water split reaction is held at constant temperature. The efficiency at this point would be 100%, neglecting any thermal or processing losses. The cell voltage of the thermoneutral state ($U_{th}^0$) can be calculated according to Eq. 1, where $\Delta H_R$ is the reaction enthalpy at a specific temperature, see also Figure 1 (a), and F denotes Faraday's constant.

$$U_{th}^0 = \frac{\Delta H_R}{2\,F} \qquad\qquad \text{(Eq. 1)}$$

At standard conditions, the thermoneutral voltage is 1.23 V. It rises to 1.29 V (steam) at 800°C, and would be 1.48 V for liquid water in alkaline electrolysis and PEM. The mole stream of hydrogen produced ($\dot{n}_{H2}$), however, solely depends on the applied current according to Eq. 2.

$$\dot{n}_{H2} = \frac{I}{2\,F} \qquad\qquad \text{(Eq. 2)}$$

The relation of applied current and resulting cell voltage for alkaline electrolysis, PEM and SOEC is shown in Figure 1 (b). Following Ohm's law, the lower the cell resistance, the slighter the increase in cell voltage will be, when more current is applied. Lowering the cell resistance by improving the cell kinetics and electrical conductivity, is a main task of the present thesis and the approaches are explained in the following chapters [9].
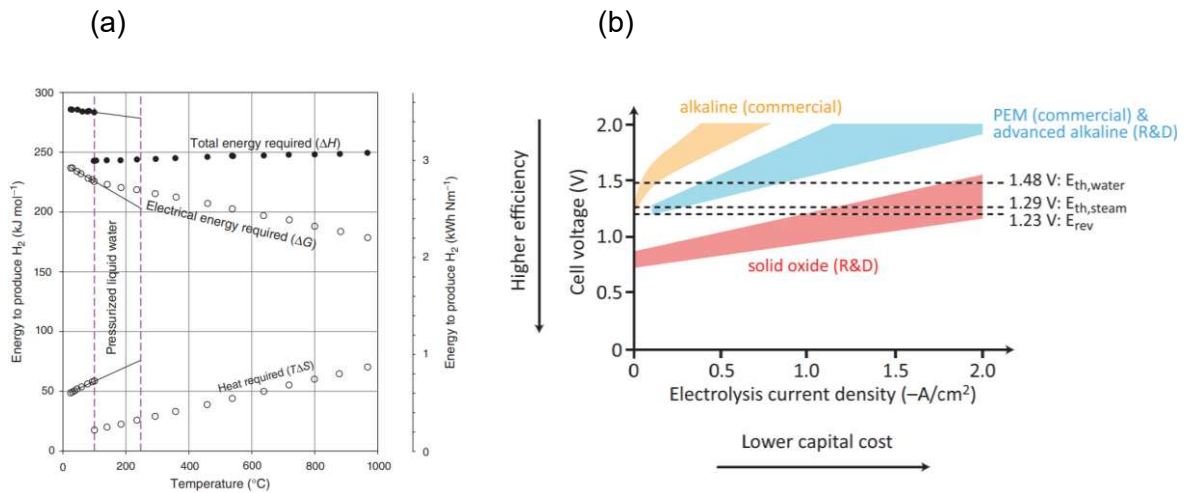
Figure 1: Temperature dependence of $\Delta H_R$, $\Delta G_R$ und $T\Delta S_R$ (a) [9] and polarization curves of various state of the art water electrolysis cells (b). $E_{th,water}$ and $E_{th,steam}$ represent the thermoneutral voltages for water and steam electrolysis, respectively. $E_{rev}$ denotes the reversible potential for water electrolysis at standard conditions [10].

As it can be derived from Figure 1 (b), SOEC technology reaches $U_{th}^{0}$ at much higher current densities than the other technologies. This means, that significantly more hydrogen can be produced per active cell area at highest efficiency. In other words, the productivity of the technology is superior to state of the art technologies. The main reason for that is the open circuit voltage (OCV), which is the potential at zero current and is calculated according to the Nernst equation (Eq. 3 [11]).

$$OCV = \frac{\Delta G_R^{0}}{2\,F} - \frac{R\,T}{2\,F}\,\ln\frac{p(H_2O)}{p(H_2)\,\sqrt{p(O_2)}} \tag{Eq. 3}$$

$\Delta G_R^{0}$ … Gibbs free reaction energy at standard conditions
R  … universal gas constant
p(c) … partial pressure of the respective component c

The Gibbs free reaction energy for the water splitting reaction decreases at higher temperatures which leads to the lowest OCV for SOEC as shown in Figure 1. In order to achieve high production rates, Alkaline and PEM electrolysis will more likely be operated at a cell voltage above thermoneutral state. In this case, more heat than necessary for the heat consuming chemical reaction is generated, resulting in an exothermic operational mode. In contrast, SOEC may also be operated below 1.29 V if external heat sources are available. This offers the possibility of utilizing waste heat to produce hydrogen. For instance, metallurgical processes often produce waste heat with high potential for further usage. This is one reason why future SOEC could be efficiently integrated at steel production sites [12].

### 3.1.2 Working principle

SOC are versatile electrochemical devices that can switch between converting electrical energy into chemical energy (SOEC mode) and converting chemical energy into electrical energy (SOFC mode). Essentially, for some applications the cells may serve both as fuel cells and electrolysis cells. Due to this reversible functionality, these types are commonly known as Reversible Solid Oxide Cells (RSOC). In SOEC configuration, steam interacts with electrons from an external power source at the fuel electrode (SOEC cathode). This interaction results in the production of $H_2$ as well as oxygen ions. These oxygen ions then traverse through an ion-conducting, gas-tight electrolyte driven by the electric field to reach the air electrode (SOEC anode). There, the oxygen ions are oxidized to molecular oxygen and release electrons. In Solid Oxide Fuel Cells (SOFC), the reverse reactions occur, generating electricity that can be supplied to an external consumer. Between the air electrode and the electrolyte, an ion-conducting diffusion barrier layer is deposited to prevent any chemical sidereactions between the two components. Further explanations about the materials are given in Chapter 3.2. The operating principles of SOFC and SOEC are shown in Figure 2.
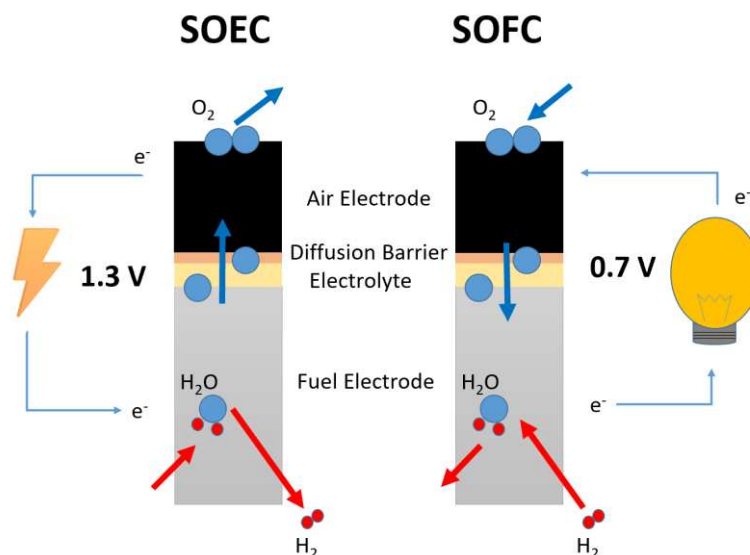


Figure 2: Operating principle of solid oxide cells in electrolysis mode (right) and fuel cell mode (left).

To ensure the mechanical stability of an SOC, the electrolyte (electrolyte supported cell, ESC) or one of the electrodes has a greater layer thickness than the other components. This particular component provides the SOC with the necessary mechanical robustness. In case of electrode supported cells, anode supported cells (ASC), referred to the denotation of the fuel electrode in fuel cell mode, are more commonly utilized than cathode supported cells (CSC). ASCs show cost effectiveness and superior mechanical properties of the materials involved. In addition to these three options, SOC can also be designed as metal-supported cells. In this configuration, the mechanical stability is provided by an additional electrochemically inactive metal layer [13,14].

In contrast to the OCV, which is a function of temperature and partial pressures, the operational voltage is also dependent on the current density. The operation of SOC can be characterized through voltage-current density curves. In case of the electrolysis mode, an example of such an operational curve is given in Figure 3. Current densities are denoted as "negative", which means, electrical energy is supplied to the cell.
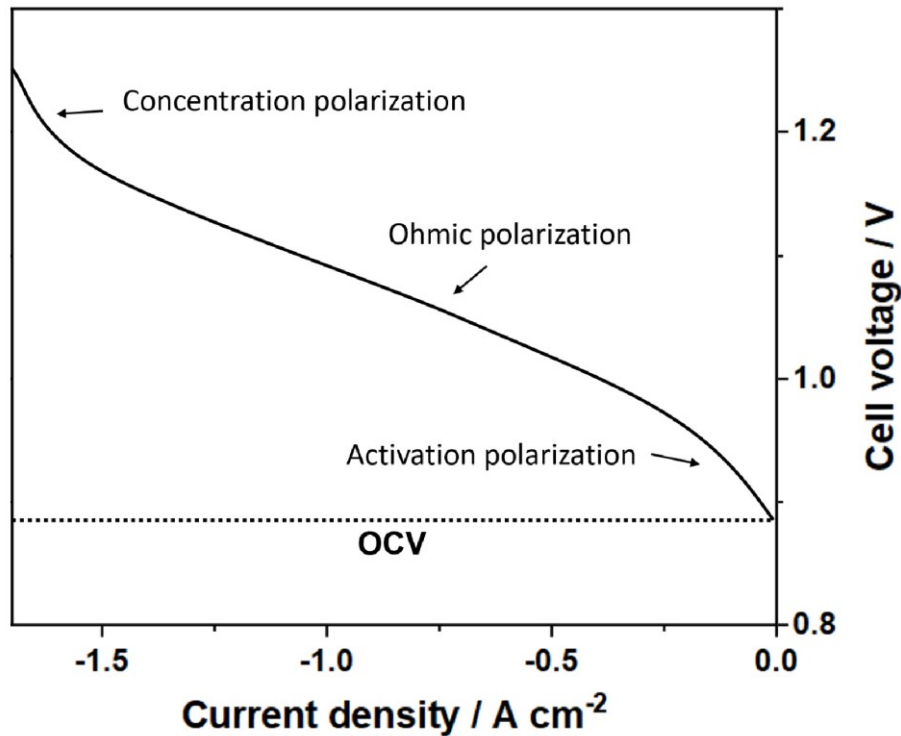


Figure 3: Example of a current density – voltage curve of a solid oxide cell in electrolysis mode including polarization losses. OCV corresponds to 800°C and 90 % $H_2$ and 10 % $H_2O$.

When a cell is subjected to a current, there is a change in cell potential due to polarization effects. As the amount of hydrogen produced is only dependent on the current, the higher the cell voltage becomes, the more electrical energy will be converted to heat. Polarization effects, which influence the operational voltage, can be distinguished by different origins. The effect of activation polarization dominates in regions of low current densities. Overcoming energetic barriers attributable to the inertia of electrode kinetics is essential for facilitating ion and current flow. At moderate current densities, ohmic resistances of the single cell components are responsible for overpotentials. The conductivity of the cell materials is limited. As a consequence, the internal electric resistance comprises the resistance associated with both ionic and electronic charge transport within the electrolyte, fuel, and air electrode. The thicker the layer within the cell, the higher will be its contribution to the overall ohmic polarization $\eta_\Omega$ [15].

$$\eta_\Omega = \mathrm{i}\,\mathrm{r} = \mathrm{i}\left(\sum_c \rho_c\,\mathrm{L}_c\right) + \mathrm{R}_{contact} \qquad \text{(Eq. 4)}$$

$\mathrm{R}_{contact}$ ... contact resistance

$\rho_c$ ... specific component resistance

$\mathrm{L}_c$ ... layer thickness

i ... current density

At high current densities, losses occur due to concentration polarization. Gas transport losses, caused by concentration polarization, occur when gaseous reactants provided during the electrochemical reaction are consumed at the electrodes. This consumption leads to the establishment of a concentration gradient and a subsequent loss in potential. As a result of the continuous consumption of reactants, which is $H_2O$ in this case, the cell potential decreases. In this way, a reduction in the partial pressure of the gas causes the overpotential. The porous electrode material is unable to sustain the initial concentration of the gases. To some extent, the effect can be tackled by optimizing the microstructure of the electrodes, which can enhance gas supply and removal of the products. Losses, associated with concentration polarization, are also termed gas transport losses [15].

### 3.1.3  Operating conditions

In industrial environments, single SOC are combined to stacks. In these, typically 30 to 100 cells are interconnected in series via metallic or ceramic interconnects. These interconnects play a crucial role by providing both electrical contact and gas separation between the cells, while also ensuring the distribution of gas across the electrodes. The stacked units are further organized into modules and integrated into systems. Following Eq. 2, a stack incorporating 55 single cells with 100 cm² active area operated at 1 A cm⁻² would produce ~0.2 kg $H_2$ per hour. A hydrogen car has a consumption of about 1 kg $H_2$ per 100 km. The comparison between production rate and demand gives an impression of how important the kinetics, expressed by current density, of the electrolyser is. Other approaches to increase production rates would be to increase the cell size and active area, or to build stacks with even more single cells. Scalability is another significant obstacle to the advancement of SOEC. Obtaining crucial information about the inner workings of the stack would be essential for designing the most efficient SOEC system. The intricate and compact structure of an SOEC stack hinders precise inner stack measurements which is a challenge for modelling [16].

The electrochemical efficiency of SOEC stacks is influenced not solely by the cell activity. Further factors like the functionality of other stack components such as metallic interconnects, glass sealings, and flow channels come into play. Long-term operation introduces alterations in the properties of these components: Interconnects undergo corrosion and creep, glass crystallizes, electrodes coarsen and accumulate impurities while ions interdiffuse. Importantly, these cell components exhibit strong interactions with each other [17]. Due to the necessity of gas channels in stack components for fuel and air supply, full-area electrical contact with both electrodes is not feasible. Typically, on the fuel side, a net/mesh is employed to connect the

fuel electrode to the interconnect, simultaneously serving as a fuel channel distributor. On the air electrode side, channeled metals or ceramics are utilized. This design results in regions with no (or limited) air flow and areas lacking electrical contact. In many cases, additional layers are incorporated to enhance electronic conduction (further explained in Chapter 3.2.1). On the fuel side, nickel (Ni) paste is sometimes applied to the cell, while on the air side, a highly conductive layer consisting solely of the underlying electrode material functions as a current collector [18].

In order to evaluate the performance of single cells, it is therefore of great importance to be aware of the operating conditions of cell stacks. This includes not only stack build up or impurities originating from stack components, but also operating conditions like steam conversion rates, humidity, operating voltage and temperature. Otherwise, improvements that are demonstrated at cell level might not be relevant at stack level. It has been shown that higher steam humidification accelerates stack degradation due to microstructural changes within the fuel electrode. Also high steam conversion rates result in fast degradation [19,20]. In addition, higher operation temperatures lead to higher degradation rates as well [21]. Based on recent stack test parameters summarized by [19], SOEC stacks are capable of reaching current densities up to -0.9 A cm$^{-2}$ at maximum feed humidity of 80%. Steam conversion rates reach 75% at moderate degradation level. Long-term operation in SOFC mode has been successfully demonstrated over several years with a voltage degradation rate of 0.5% kh$^{-1}$. However, SOEC stacks still face several issues that lead to higher degradation. It is proposed that commercial SOEC stacks should prove degradation rates below 1% kh$^{-1}$ [22]. In recent years, degradation rates have successfully been improved as shown in Figure 4. In the majority of documented tests, degradation rates currently stay below 1% kh$^{-1}$ [17]. However, depending on the test conditions, reported rates still reach up to 1.5% kh$^{-1}$ [23].

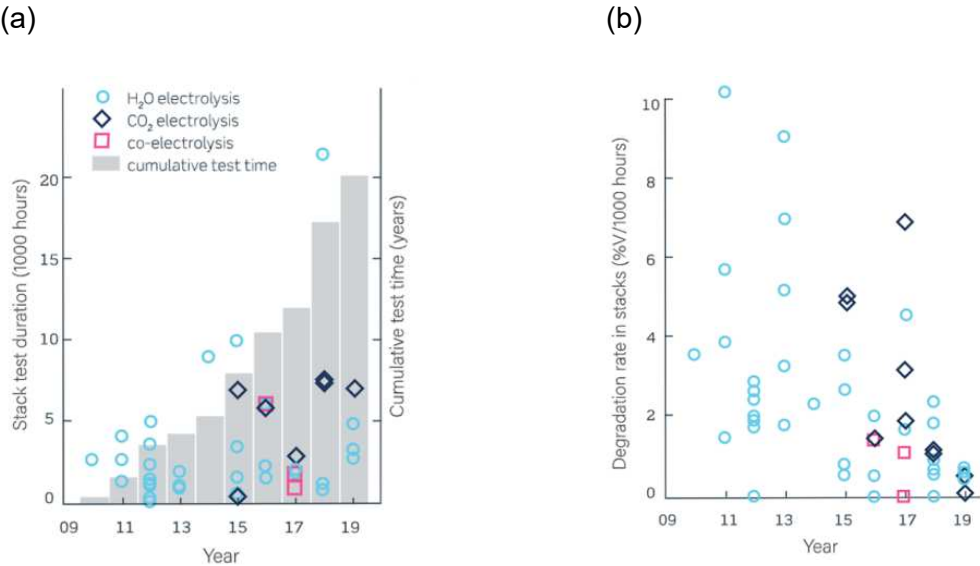(a)                                                        (b)



Figure 4: Progress made in durability of SOEC in terms of test duration (a) and degradation rates (b) [17].

## 3.2 Cell components in solid oxide technology

This chapter provides insights into the critical aspects of SOC components with a focus on the air electrode. The overview includes design, materials, and challenges of the single components related to long-term performance and stability.

### 3.2.1 Air electrode

The SOC air electrode is the core topic of interest of the present thesis. Beside a summary about the component and its requirements especially in terms of microstructure, the most common degradation mechanisms are described.

#### 3.2.1.1 Functionality and requirements

At the air electrode, the exchange of oxygen takes place, usually with the ambient air. In fuel cell mode, oxygen molecules are reduced to oxide ions at the air electrode, which are then transferred to the ion-conductive electrolyte. In electrolysis mode, the reverse process takes place, where oxygen is released at the air electrode. Eq. 5 shows, from left to right, the air electrode half-reaction in the SOFC mode, and from right to left, the half-reaction at an air electrode in the SOEC mode (Kröger-Vink notation) [18].

$$O_2 + 4\,e' + 2\,V_O^{\bullet\bullet} \rightleftharpoons 2\,O_O^\times \qquad\text{(Eq. 5)}$$

The air electrode has to fulfil several criteria, especially high mixed ionic-electronic conductivity as well as chemical stability. Values used as guidelines, are around 100 S cm$^{-1}$ for electronic and 10$^{-3}$ S cm$^{-1}$ for ionic conductivity at the targeted operational temperature, to ensure efficient electron and oxygen ion transport across the electrode. In terms of conductivity, there is a categorization either as n-type or p-type conductor. N-type conductors require an oxygen deficiency to generate electrons, making them unstable under oxidizing conditions such as ambient air. P-type electronic conductors remain stable in air, as they require an excess of oxygen to generate holes [23,24]. The air electrode should also exhibit a suitable thermal and mechanical compatibility with other components at both operating and preparation (sintering) temperatures. The material's thermomechanical characteristics need to match those of the electrolyte to prevent stresses during heating or cooling. There is a potential for delamination when there is a mismatch between the electrode material and the electrolyte. Moreover, the mentioned high level of electrical conductivity is crucial for performance in long-term industrial applications. The critical attributes of the air electrode include catalytic activity in the oxygen reduction or oxidation reaction. The reaction process includes several steps, where each could be potentially rate limiting, which influences the overall cell performance. The processes involved include mass and charge transfer at the electrode/electrolyte interface, solid-state bulk diffusion and surface diffusion, surface adsorption/desorption, and gas diffusion. Finally yet importantly, used materials should be cost effective and sustainable [23,25,26].

In addition to material properties, the electrode performance is highly influenced by the microstructure, which includes parameters such as thickness, porosity, tortuosity, and particle size as well as particle interconnection of the electrode, as well as adhesion to the electrolyte.

Figure 5 gives an indication about the importance of the microstructure and the necessity of open porosity of a mixed ionic-electronic conducting (MIEC) air electrode material.
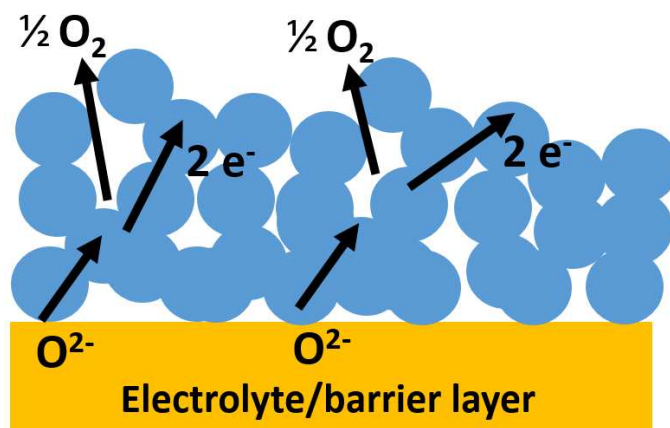


Figure 5: Oxygen ion transport to the air electrode and oxidation at double phase boundaries. The electric circuit is closed via current collection.

The morphology of the chosen material is mostly determined by synthesis, sinter processes and fabrication techniques. The optimal microstructure depends on the characteristics of the applied material. Nanostructured materials have been proposed as a method for enhancing gas diffusivity in the electrode and extending the specific surface area of the porous electrode structure. Optimized microstructure may even enable operation at lower temperatures [23].

<u>Current collector layer</u>

Enhanced electrochemical performance is linked to an improved electrical contact between the current collector and the electrode, leading to a decrease in ohmic resistance. The thinner the air electrode, or the lower its conductivity, the more important it is to apply an additional highly conductive layer on top of the air electrode. This is referred to as current collector layer (CCL) that optimizes electrical current transport from a mesh to the SOC. When operated with CCL, a thickness of the functional air electrode of at least 10 μm should be sustained. In contrast, the CCL can reach up to 50 μm for the best performance. If the thickness of the current collector is insufficient in comparison to the distance between the contact points of the mesh, it cannot be guaranteed that the current is effectively collected from the entire interface area. However, too thick layers might block gas diffusion and therefore should be as porous as possible [23,27,28].

## 3.2.1.2 Materials

The majority of air electrode materials are perovskites. These oxides consist of at least three elements: The $A^{n+}$ and $B^{m+}$ cations, as well as the $O^{2-}$ anions. Figure 6 shows the structure of an $ABO_3$ perovskite. The A-site cation is typically a rare-earth or alkaline-earth ion, with a larger ionic radius than the B-site cation, which is typically a transition metal. Perovskites can have diverse physical properties that are influenced by their structure and chemical composition.

Ideally, A and B cations have a combined charge of n+m = 6. The B cation is surrounded by 6 oxygen ions, and the A cations are coordinated by 12 oxygen ions. Both types of cations may be substituted by cations of different valence. If the electroneutrality condition (n+m) results in a sum less than six, the charges are compensated by the formation of defects, e.g. oxygen vacancies.
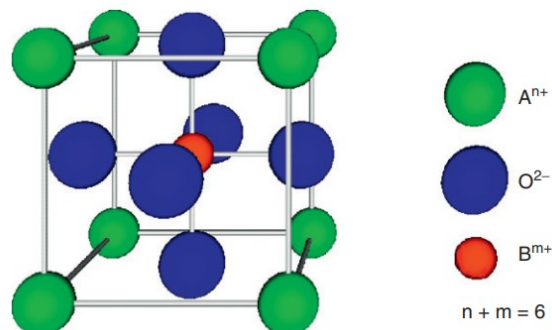


Figure 6: Structure of an $ABO_3$ perovskite [29].

Selected perovskites meet important requirements regarding SOC air electrodes such as high mixed conductivity, excellent catalytic activity, chemical stability, and/or good cost effectiveness.

One of the frequently used materials is lanthanum strontium manganite (LSM, $La_{1-x}Sr_xMnO_{3-\delta}$). Substituting a $La^{3+}$ ion with a $Sr^{2+}$ ion at the A-site results in the creation of an electron hole at the B-site to preserve electroneutrality. In this way, the electronic conductivity increases with additional Sr within the lattice and reaches a maximum of up to 490 S cm$^{-1}$ at x = 0.5 [30,31]. This acceptor-substitution however barely affects oxygen vacancy concentration. The chemical oxygen diffusion coefficient in A-site substituted LSM therefore remains rather low in the range of $10^{-11}$ cm² s$^{-1}$ [32]. As a consequence, the oxygen redox reaction is restricted to the LSM-electrolyte-gas interface. To compensate this effect, LSM is primarily applied in the form of a composite with a good ionic conductor such as YSZ. The composite shows a significant increase in triple phase boundaries where the air electrode, electrolyte, and gas phase intersect. The combination lowers the overall electronic conductivity but enhances stability [33]. The performance of LSM-YSZ composite electrodes is adequate in the high-temperature range. At temperatures below 750°C, however, catalytic activity becomes relatively poor and the ionic conductivity of YSZ decreases. Consequently, development of electrode materials for lower temperatures focusses on MIEC perovskites.

For MIEC, the reaction zone is extended to the entire air electrode surface, as shown in Figure 4. State of the art materials are lanthanum strontium cobalt oxides ($La_{1-x}Sr_xCoO_{3-\delta}$, LSC). In LSC, replacing lanthanum ($La^{3+}$) with strontium ($Sr^{2+}$) improves both oxygen ion conductivity and electronic conductivity through the generation of electron holes and oxygen vacancies. Despite LSC showing great electrochemical performance, the TEC mismatch to the electrolyte or diffusion barrier material could be an obstacle for long-term operation [34-36]. Doping the B-site with iron (Fe) ions lowers the TEC, which is one of the reasons why the lanthanum strontium ferrite series (LSCF, $La_{1-x}Sr_xCo_{1-y}Fe_yO_{3-\delta}$) is another important MIEC class for SOC

air electrodes [37]. However, the ionic conductivity in LSCF is reliant on the substitution of Co with Fe, and decreases with increasing Fe content. Increased Sr and Co contents lead to higher oxygen permeability and higher oxide ion mobility. This was associated with the lower oxygen ion binding energy of Co and the elevated concentration of oxygen vacancies resulting from the substitution of $La^{3+}$ with $Sr^{2+}$ [23,38]. A serious concern about Sr containing air electrodes is their reactivity with the electrolyte. The most notable by-product is $SrZrO_3$ (SZO), which forms mainly during the sintering process. The formation of this isolating reaction phase leads to degradation of cell performance [39]. Measures mitigating this process are described in Chapter 3.2.2.1.

An alternative material class for air electrodes are rare earth nickelates. The nickelate structure $Ln_{n+1}Ni_nO_{3n+1}$ (n = 1) is composed of alternating $Ln_2O_2$ rock salt layers and polyhedral $NiO_2$ square plane layers, with interstitial oxygen present in the rock salt layers. It can be described as a Ruddelsden-Popper (RP) phase of first order where perovskite and rock salt layers alternate. Rare-earth nickelates exhibit high ionic and satisfactory electronic conductivities. The ionic conductivity in these primarily occurs through oxygen interstitials within the rock salt layers of the crystal structure [40,41]. Similar to perovskites, there is the option to substitute rare-earth nickelates and thus to influence their material properties. Undoped nickelate compounds exhibit certain drawbacks in their application as SOC air electrode materials, such as inadequate phase stability or insufficient electronic conductivity. By partially substituting Ni with other 3d transition metals, specific material properties can be tailored [42]. $La_2NiO_{4+\delta}$ (LNO) and $Pr_2NiO_{4+\delta}$ (PNO) have been considered as most promising electrode candidates. PNO exhibits superior electrochemical performance, characterized by the lowest polarization resistance ($R_P$), enhanced ionic and electronic conductivity, and higher diffusivities compared to LNO. This distinction is particularly noticeable at intermediate temperatures below 700 °C. In contrast, LNO shows better stability at high temperatures [23,43-45]. PNO can be stabilized through substitution with rare earth and alkaline earth metals. Specifically, praseodymium (Pr) can be partially replaced by neodymium (Nd) or La, aiming to preserve the favorable electrode properties of PNO as much as possible. Investigations with $La_{2-x}Pr_xNiO_{4+\delta}$ where $2 \geq x \geq 0$ indicate a decrease in electrode performance with increasing La content. Stabilization of the Pr-nickelate is achieved at x = 0.5 [42].

### 3.2.1.3 Degradation mechanisms

The mentioned materials exhibit impressive capabilities as air electrodes for SOC, but they face challenges due to degradation effects. The most critical degradation mechanisms include the formation of secondary phases during operation and the delamination of the air electrode, especially in electrolysis mode.

Surface deactivation

The stability and performance of cells are significantly influenced by interface effects. This is characterized by unfavorable reactions caused by element segregation/interdiffusion. At the electrode/electrolyte interface, microstructural alterations, interfacial reactions or micropore formation can be caused. Surface segregation, influenced by factors like lattice structure,

operating temperature, ion mobility, polarization, and composition/stoichiometry, results in the deterioration of surface functionality [46,47].

Perovskites, with their typical composition of larger A-site and smaller catalytically active B-site cations, experience segregation of the larger A-site cation to the interfaces, forming insulating oxides or RP layers. This segregation impedes the contact of the B-site cation with reactants, hindering oxygen and charge transfer. Recent studies on A-cation segregation highlight the importance of a suitable choice of A-site to address these challenges [23]. The explanation of thermodynamic and kinetic conditions governing surface segregation and transitions among potential surface phases/structures on perovskite oxides remains insufficient. An example for A-site cations that segregate to the electrode surface is Sr, which passivates the air electrode surface via the formation of SrO [48]. As pointed out, Sr is most commonly present in state of the art electrodes. It is suggested that surface charging plays an important role in the Sr segregation mechanism. This assumption is supported by the evidence that varying the surface charge by variation of Sr content has an influence on the segregation mechanism [49,50]. However, this electrostatic contribution alone does not explain the extensive segregation observed in materials like LSM [49]. Investigations about other influencing factors resulted in the assumption that higher air humidity drives Sr particle growth at the electrode surface [48,51]. Recent ideas to minimize the segregation, target optimizing perovskite composition and microstructure at the surface [50]. At some conditions, a deficiency in Sr within the perovskite structure might suppress the effect [52]. In addition, it is assumed that diffusion of Sr within the bulk is minor and the observations of rapid surface enrichments can only be explained by grain boundary diffusion. Therefore, increasing the particle size of air electrodes might be a promising strategy [53]. Reducing the cation size mismatch at the perovskite A-site e.g. by using calcium ($Ca^{2+}$) instead of $Sr^{2+}$ might be another strategy suppressing the segregation effect. Still, there is a driving force that facilitates cation enrichment at the electrode surface even with Ca [54,55].

Another key degradation mechanism related to A-site ion segregation towards the surface of the air electrode is chromium (Cr) poisoning. Within an SOC system, metallic components that contain chromium are used, e.g. interconnects or heat exchangers. Cr is volatile and deposits at the air electrode surface. Especially in moist air, $CrO_3$ or $CrO_2(OH)_2$ reacts with Sr to $SrCrO_4$ [56-58]. On the other hand, it has been reported that $H_2O$ may react with Cr accumulations at the air electrode to reactivate targeted areas [59].

Segregated A-site cations are also prone to react with sulphur (S). Electrically isolating $SrSO_4$ crystals accumulate at the air electrode surface even in an atmosphere containing only a few ppm sulphur. It has been demonstrated that thermal treatment can partially regenerate the original perovskite structure [60-62]. However, the thermal treatment results in a reduction in catalytic activity and thus performance [63].
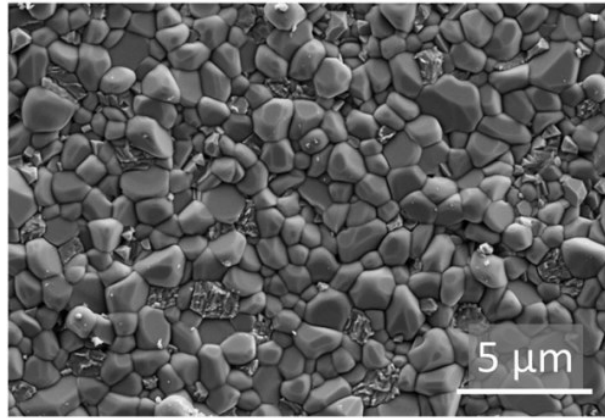
Figure 7: SrSO$_4$ crystals on a degraded La$_{0.6}$Sr$_{0.4}$CoO$_{3-\delta}$ surface [63].

Notable other consequences of Sr segregation include the formation of SrCO$_3$. Like other secondary phases, the carbonate reduces the active surface area. The formation occurs when surface SrO reacts with CO$_2$ present in air, especially when the SOC is cooled to ambient temperature [64]. In addition, it has been observed that the formation of SZO at the electrode/electrolyte interface during operation is significantly increased in electrolysis mode, while it seems to be negligible in fuel cell mode [65].

Electrode delamination

During electrolysis, a gradient in oxygen partial pressure occurs across the electrode/electrolyte interface. The buildup of high oxygen partial pressures at the interface of the electrolyte to the air electrode accelerates degradation via the generation of oxygen gas bubbles at the interface, which result in delamination or microstructural changes [66,67]. It is assumed that oxygen may be liberated especially within defects at the electrode/electrolyte interface [68]. This phenomenon could be attributed to the electrode's reduced capacity to conduct oxide ions and the electrolyte's enhanced ability to release oxygen. Over time, a high oxygen partial pressure may accumulate, leading to the delamination of the electrode. Observations also led to the theory that even the very low partial electronic conductivity of the electrolyte can be sufficient to form molecular oxygen within nanopores in the material. In case of increasing pressure, cracks may occur [67,69]. On the other hand, it is suggested to tailor electronic conductivity of the electrolyte to minimize the tendency for high pressure buildup at the interface. This may be accomplished by applying a thin layer (equal or below a micron) of a material that solely conducts O$^{2-}$ while possessing high electronic resistance onto the underlying electrolyte on the side of the air electrode [70].
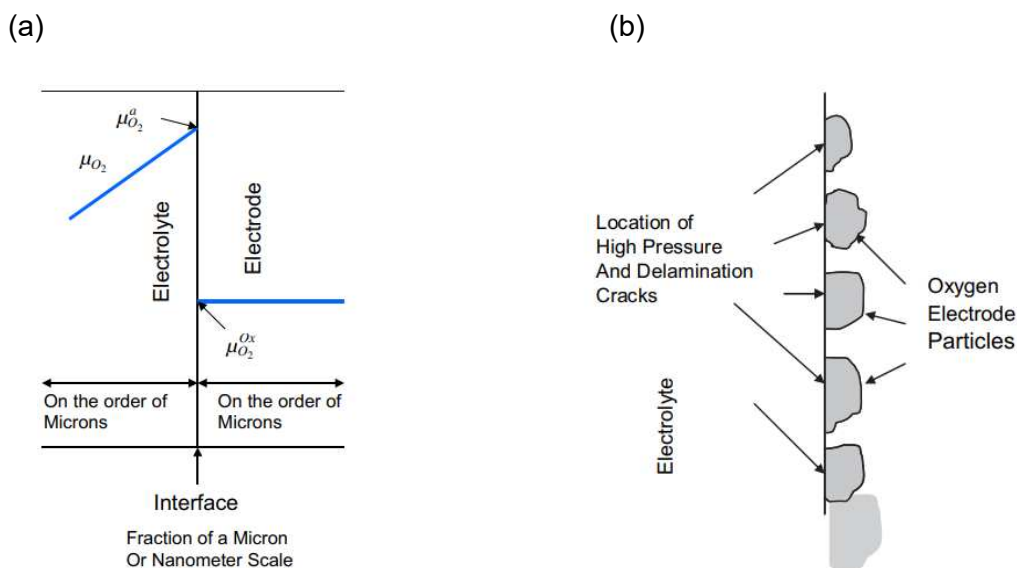
Figure 8: Illustration of abrupt increase in oxygen chemical potential via high oxygen pressure at the electrolyte/air electrode interface (a) and schematic of development of cracks/voids within the structure (b) [70].

## 3.2.2 Other components

In this chapter, the SOC components that are not in the main focus of the present study are being reviewed.

### 3.2.2.1 Electrolyte

The electrolyte of an SOC serves several important functions. Firstly, it ensures the gas tightness of the cell to avoid failures caused by leakage. If applied within an ESC, the mechanical strength should be sufficiently high to effectively withstand stress. In any case, the electrolyte acts as an electronic isolator. The material should possess negligible electronic conductivity but high ionic conductivity. Electrons are intended to flow exclusively through the external power source or, in the case of a fuel cell, through a consumer. The charge transport is predominantly ionic, which means it shall account for > 99% of the total conductivity. A decrease in the ionic transport number adversely affects the SOC efficiency, leading to an internal leakage current within the electrolyte. In the majority of state of the art electrolyte materials, oxide-ion conduction follows a vacancy migration mechanism, whereby oxide ions hop through the crystal lattice using vacancies on the oxygen sub-lattice. Electrolyte materials are usually doped with lower-valence elements. The substitution of $Zr^{4+}$ with trivalent cations such as yttrium ($Y^{3+}$) or scandium ($Sc^{3+}$) creates oxygen vacancies through charge compensation. Through these vacancies, the oxides transform into oxygen ion conductors. The migration enthalpy of oxygen vacancies is strongly dependent on the migration path from one lattice positon to the next one. Therefore, oxides crystallizing in the fluorite structure show the highest ionic conductivities and are most frequently used. The fluorite structure can be

characterized as a face-centred cubic arrangement of metal ions, where the tetrahedral sites are filled by oxygen ions.

Yttria-stabilised zirconia (YSZ) is the most commonly used solid electrolyte material in solid oxide cells. Main advantages of YSZ are its compatibility to common fuel electrode materials in terms of thermal expansion coefficient, as well as low costs. The addition of Y serves to stabilise the cubic fluorite phase, as well as to increase the concentration of oxygen vacancies, as shown in Kröger-Vink notation in Eq. 6. Consequently, the ionic conductivity is increased [18].

$$Y_2O_3 + 2\,Zr_{Zr}^{\times} +\ O_O^{\times} \rightarrow 2\,Y_{Zr}' + V_O^{\bullet\bullet} + 2\,ZrO_2 \tag{Eq. 6}$$
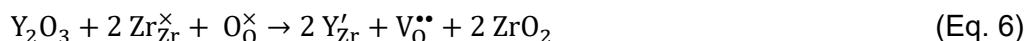
Undoped zirconia ($ZrO_2$) occurs in the monoclinic phase at room temperature. As the temperature increases, $ZrO_2$ experiences phase transitions, first to a tetragonal and then to a cubic structure. The introduction of di- or trivalent dopants into zirconia can stabilise the higher symmetry phases at lower temperatures [71]. For $ZrO_2$ with around 8 mol% $Y_2O_3$, highest conductivity is achieved. Substitution beyond this limit results in unfavorable defect association effects [72]. An example of an electrolyte material, which shows higher ionic conductivity than YSZ, is scandia-doped zirconia (ScSZ). The ionic radius of $Sc^{3+}$ is closer to that of $Zr^{4+}$ than that of $Y^{3+}$. However due to price and availability issues the usage of SzSZ as electrolyte is rather limited [73-75].

In addition to requirements concerning performance and short-term compatibility of electrolytes, some aspects have to be considered regarding long-term stability. While low porosity is an important attribute for gas tightness, dense microstructure is also important for structural stability during electrolysis operation. Pores may develop in the electrolyte due to the generation of molecular oxygen within pre-existing defects. This mechanism of pore formation is shown in Figure 9. The central part depicts the YSZ electrolyte, flanked by a composite air electrode on the right and the fuel electrode on the left. A magnified view on the right focuses on the YSZ electrolyte, where holes are formed within the grain boundaries of the YSZ at the air electrode interface. The mechanism is driven by high oxygen partial pressure due to high electrolysis current. The pores not only increase cell resistance but also account for fractures that frequently can be observed after long-term electrolysis [68].
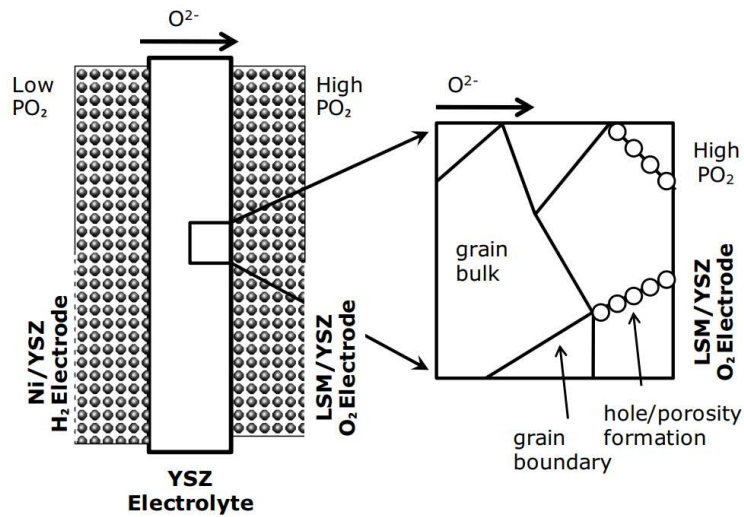
Figure 9: Illustration of porosity formation within the SOC electrolyte due to high current densities in electrolysis mode [68].

While YSZ shows chemical stability in contact with state of the art fuel electrodes, it tends to react with the air electrode to form unwanted secondary phases, as mentioned in Chapter 3.2.1.2. To mitigate the formation of SZO, a Zr-free ion-conducting interlayer is applied in between the air electrode and the electrolyte, e.g. doped $CeO_2$. Gadolinium (Gd)-doped ceria (GDC, Eq. 7) is usually co-sintered with the YSZ electrolyte and densified at high temperatures. A disadvantage is the formation of an interdiffusion zone between GDC and YSZ, which raises the internal resistance of the cell due to its lower ionic conductivity, and thus leads to lower cell efficiency. The GDC microstructure remains porous, and is therefore not able to completely prevent the SZO formation. However, the higher the sintering temperatures are, the more significant is the occurrence of a dense interdiffusion zone, which can also block SZO formation. In this way, manufacturing is a trade-off between the thickness of a poorly conducting GDC/YSZ interdiffusion zone and an isolating SZO layer [76].

$$Gd_2O_3 + 2\,Ce_{Ce}^{\times} + O_O^{\times} \rightarrow 2\,Gd_{Ce}' + V_O^{\bullet\bullet} + 2\,CeO_2 \qquad\qquad \text{(Eq. 7)}$$
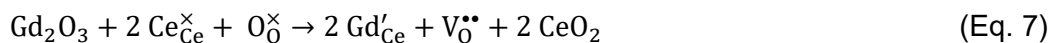
GDC would also be an opportunity as electrolyte material. Similar to $ZrO_2$, cerium oxides exhibit a fluorite structure. The cubic phase remains stable at room temperature, primarily attributed to the larger ionic radius of the $Ce^{4+}$ ions. GDC exhibits a higher oxygen diffusion coefficient than YSZ. However, utilizing doped ceria as an electrolyte is limited to the temperature range below 600°C, since at higher temperatures and especially at low oxygen partial pressures, $Ce^{4+}$ ions are partially reduced to $Ce^{3+}$, which induces undesired partial electronic conductivity [77,78].

Another oxygen-ionic conductor is δ-$Bi_2O_3$, which crystallizes in a fluorite structure. This material demonstrates high oxygen-ion conductivity, even without the need for doping, owing to the presence of 25% vacancies at anion sites. Despite its lower sintering temperatures compared to zirconia and ceria, stabilized bismuth oxide encounters challenges such as material instability, reactivity, and reduction to metallic Bi under fuel conditions. Efforts to

prevent phase transformations and enhance stability face challenges in terms of compatibility with other SOC components and potential cost implications compared to alternative air electrode materials [18,79,80].

### 3.2.2.2    Fuel electrode

At the fuel electrode, hydrogen is oxidized in fuel cell mode or is produced through electrolysis using water in electrolysis mode. In general, SOC technology is capable of processing various kinds of fuels aside from hydrogen, like carbon oxides or hydrocarbons, which is not within the scope of this thesis. In SOFC operation, oxygen ions are transported to the fuel electrode, where they oxidize hydrogen or carbon monoxide. Figure 10 (a) illustrates the reaction mechanism in SOFC mode. The reversible operation allows for the opposite direction of oxygen ion transport in the electrolysis mode. In the SOEC mode, oxygen ions are generated from the water supplied to the fuel electrode.

$$H_2 + O_O^\times \rightleftharpoons H_2O + V_O^{\bullet\bullet} + 2\,e' \qquad\qquad \text{(Eq. 8)}$$

Requirements for fuel electrode materials comprise high electronic conductivity, good stability in reducing environment, good thermal compatibility with other cell components, and high electrocatalytic efficiency for oxidation reactions. Additionally, the material should be optimized in terms of porosity to facilitate the transport of gases (Figure 10 (b)). The combination of these factors plays a crucial role in enhancing the performance of SOFCs by minimizing the polarization losses associated with the oxidation reaction [18,81].
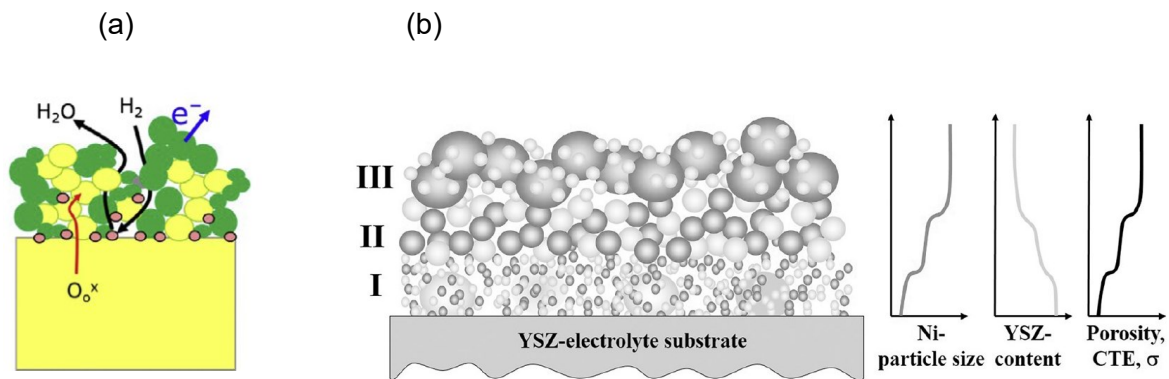


Figure 10: Illustration of oxidation reaction at the fuel electrode in SOFC mode (left) and its microstructural buildup (right) [18].

Hardly any materials fulfil all the mentioned requirements. Most state of the art fuel electrodes are fabricated from composites of Ni and YSZ. Nickel exhibits exceptional electrocatalytic activity in steam electrolysis, but it possesses only electronic conductivity. To facilitate the transport of electrons, oxide ions, and gas species to and from the electrode, nickel is often combined with an ionic conductor like YSZ. These composite electrodes are referred to as cermets. However, despite showing great characteristics in meeting most of the fuel electrode criteria, Ni-YSZ cermets still face some challenges. When subjected to SOEC-relevant

temperatures, nickel metal is prone to oxidation in the presence of steam. Therefore, a portion of the product gas has to be recycled in order to sustain reducing environment [82].

In addition, there are some disadvantages in using Ni regarding its high mobility at operating temperatures above 650°C. Therefore, it is quite challenging to maintain the optimal Ni structure over many years of operation. Microstructural changes observed in the anode, a porous cermet composed of Ni and YSZ, is the coarsening and agglomeration of the Ni particles. The enlargement of Ni particles typically follows two fundamental mechanisms. One of these is Ostwald ripening. It is a process involving the migration of single atoms or molecules, where Ni atoms are released from one Ni particle, migrate across the support or through the vapor phase and are captured then by another particle [83,84]. The second one is Ni particle migration over the support followed by merging with other Ni clusters [85]. In the absence of additional driving forces, both mechanisms depend on the transport of Ni, driven by the surface energy difference between small and large particles. This dynamics lead to the growth of larger Ni particles, while the smaller ones diminish and eventually vanish, resulting in an overall coarsening of the microstructure [84]. There are also indications that fuel electrode degradation is additionally driven by the electrochemical potential during operation. The hypothesis is that the potential drives Ni migration in the form of NiOH or $Ni(OH)_2$ [85].

Hence, there is a need to explore alternative cermet-based anodes to address these issues. Ceramics emerge as the most effective combination of electronic and ionic conductors in reducing atmospheres. Material classes such as modified zirconia, strontium titanate, and lanthanum chromite exhibit sufficient catalytic activity for oxidation of hydrocarbon fuels and demonstrate resistance to adverse conditions [86-88]. Additionally, Cu–CGO anodes have the potential to serve as anodes for SOC since Cu facilitates the release of electrons on the anode side. Consequently, this leads to an increase in conduction within the circuit [88].

## 3.3 High entropy perovskites

This chapter introduces the material class of high entropy perovskites (HEP). The origin of their potentially special properties is evaluated, while the later subchapters review application areas.

### 3.3.1 Definition

Perovskites such as LSC and LSCF are among the most important materials for solid oxide air electrodes as they exhibit fast oxygen exchange kinetics and high electronic conductivity. However, their insufficient long-term stability is a critical issue. As pointed out, A-site cation segregation leads to the formation of electronically insulating phases. To address this issue in material development, the concept of HEP represents a promising and intriguing new approach.

First reported by [89], high entropy oxides, which include HEP, are a promising approach in addressing evolving technological demands. Insights from the development of High entropy alloys revealed that the stability of phases in the solid state can be significantly influenced by the configurational entropy ($S_{config}$) of the crystal structure. This concept is transferred to oxides. Specifically, the concept of stabilizing solid phases aims at utilizing the advantageous property of high configurational entropy in the crystal. Higher configurational entropy can be achieved by increasing the number of different elements at a specific site in the crystal lattice (A- or B-site, or anion site) of the compound. Gradually increasing the elements in the system leads to an increase in configurational entropy, reaching a maximum at an equimolar distribution of ions/atoms [90]. The configurational entropy can be calculated according Eq. 9 [91]. High entropy perovskites show a configurational entropy ≥ 1.5 R. Between 1.5 R and 1 R, perovskites are called medium entropy perovskites (MEP).

$$S_{config} = -R\left[\left(\sum_{a=1}^{n} x_a \ln x_a\right)_{A-site} + \left(\sum_{b=1}^{n} x_b \ln x_b\right)_{B-site} + 3\left(\sum_{c=1}^{n} x_c \ln x_c\right)_{O-site}\right]$$

(Eq. 9)

$x_a$ ... molar fraction of the respective cation at the A-site
$x_b$ ... molar fraction of the respective cation at the B-site
$x_c$ ... molar fraction of the anion, in the present case oxygen

According to the equation, it takes at least 5 different cations in equal distribution to meet the 1.5 R. Table 1 lists a selection of ions, which can be incorporated into the perovskite structure in order to tailor properties that are relevant for the application as SOC air electrode. Their Shannon radii are given corresponding to their coordination number, which is 12 at the A-site and 6 at B-site [92]. As pointed out in Chapter 3.2.1.2, typical A-site cations include rare earth and alkaline earth elements, while transition metals are frequently used on the B-site.

Table 1: Shannon radii of selected ions, which can be applied in HEP [92].

| A-site cation (XII) | Ionic radius [Å] | B-site cation (VI) | Ionic radius [Å] |
|---|---|---|---|
| $Ba^{2+}$ | 1.61 | $In^{3+}$ | 0.80 |
| $Nd^{3+}$ | 1.27 | $Fe^{3+}$ | 0.65 |
| $Sm^{3+}$ | 1.24 | $Al^{3+}$ | 0.54 |
| $Pr^{3+}$ | 1.28 (extrapolated) | $Ga^{3+}$ | 0.62 |
| $Ca^{2+}$ | 1.34 | $Zr^{4+}$ | 0.72 |
| $Sr^{2+}$ | 1.44 | $Co^{3+}$ | 0.61 |
| $La^{3+}$ | 1.36 | $Ni^{3+}$ | 0.60 |
| $Gd^{3+}$ | 1.24 (extrapolated) | $Sc^{3+}$ | 0.75 |
| $Ce^{3+}$ | 1.34 | $Y^{3+}$ | 0.90 |
| | | $Nb^{3+}$ | 0.72 |
| | | $Zn^{2+}$ | 0.74 |
| | | $Cr^{3+}$ | 0.62 |
| | | $Hf^{4+}$ | 0.71 |
| | | $Sn^{4+}$ | 0.69 |
| | | $Ti^{3+}$ | 0.67 |
| | | $Mn^{3+}$ | 0.65 |

### 3.3.2 Properties of high entropy materials

There are several approaches in explaining the special properties that are ascribed to high entropy materials. One of those is directly related to its definition: The elevated configurational entropy lowers the Gibbs free energy, especially at high temperature. Following Eq. 10 [90], the perovskite structure is stabilized with increasing entropy term.

$$\Delta G_{mix} = \Delta H_{mix} - T\,\Delta S_{config}$$
(Eq. 10)

Another factor is the "cocktail effect", which may lead to unforeseen characteristics, including the simultaneous improvement of contrasting properties [93]. Initially suggested for high entropy alloys, it introduces a beneficial aspect to material design. It emphasizes that the properties of multicomponent compositions, are not only controlled by the fundamental properties of the single elements following the rule of mixture, but also by additional quantities arising from the interactions among these elements. In short, the material properties surpass the weighted average performance of individual components. Therefore, this effect holds significant importance in the functionalized application of high entropy oxides. Electronic structures at the atomic scale can induce the cocktail effect, which might be related to increased electronic conductivity of high entropy stabilized materials [94-96].

Lattice distortion is another effect that could explain extraordinary material properties. It can be defined by the deviation from the ideal Goldschmidt tolerance factor (t) close to 1, and is calculated by means of the average ionic radii of the perovskite as given in Eq. 11 [97].

$$t = \frac{r_A + r_O}{\sqrt{2}\,(r_B + r_O)} \qquad\qquad \text{(Eq. 11)}$$

$r_A$... average ionic radius of A-site elements

$r_B$... average ionic radius of B-site elements

$r_O$... ionic radius of the oxygen ion

In Goldschmidt's perovskite structure formalism, the parameter t ranges approximately from 0.77 to 1.05, with the "ideal" cubic perovskite occurring at t around 1.00. When t exceeds 1, the material is frequently linked to high dielectric or ferroelectric properties. Conversely, for t below 1, the material is often associated with low-symmetry characteristics [98,99]. The pronounced dispersity and stress field disorder of HEP are ascribed to variations in cation sizes. This phenomenon can decelerate undesirable cation diffusion within the HEP lattice, thereby enhancing the stability of HEP [52,100,101].

Another characteristic feature of high entropy oxides are their optimized and narrow band gaps. The band gap is described as the separation between the valence and conduction bands. Unlike the valence band, the conduction band does not contain electrons in the ground state. The band gap is therefore considered as the energetic difference between the two bands and determines the conductivity of materials, as it describes the potential difference and the ability to transport electrons from one band to another [102].

### 3.3.3 Application as air electrode

High entropy stabilization and the cocktail effect may enhance properties that could make HEP the first choice material as SOC air electrode. In the recent years, the first compositions have been synthesized and electrochemically tested. It has been tried to evaluate differences in chemical stability compared to state of the art perovskites. This subchapter gives an overview of the recent results in HEP research, which may also be compared with research results of the present study.

One of these tests includes $La_{0.2}Pr_{0.2}Nd_{0.2}Sm_{0.2}Sr_{0.2}MnO_{3-\delta}$, (HE-LSM), a high entropy equivalent of LSM. XRD measurements revealed, as expected, that the gradual substitution of $La^{3+}$ by $Pr^{3+}$, $Nd^{3+}$, and $Sm^{3+}$ resulted in a change in the crystal structure from LSM (hexagonal) to HE-LSM with the orthorhombic space group *Pnma*. Electrochemical characterization is done with an ASC substrate in fuel cell mode. The current density at 0.7 V reaches 0.9 A cm⁻². The performance is within the same range as LSM but below LSC air electrode cells [52,103,104]. A durability test is conducted in which a relatively small cathodic polarization of -0.2 A cm⁻² is applied for a maximum of 100 h at 700 °C. Pre- and post-test SEM images of the air electrode surface are compared. Due to the observation of fine particles formed at the surface, the conclusion is drawn that HE-LSM shows less Sr segregation than LSM [52]. However, no evidence is delivered that these particles contain Sr.

An example for a HEP composition with a configurational entropy above 1.5 R is $La_{0.2}Pr_{0.2}Nd_{0.2}Sm_{0.2}Ba_{0.1}Sr_{0.1}Co_{0.2}Fe_{0.6}Ni_{0.1}Cu_{0.1}O_{3-\delta}$. The electronic conductivity is compared with $La_{0.8}Sr_{0.2}FeO_{3-\delta}$ (LSF82), where the HEP reaches 635 S cm$^{-1}$ at 800 °C, while LSF82 remains below 100 S cm$^{-1}$ (Figure 11). The characteristics of the electronic conductivity of the HEP show a continuous increase towards higher temperatures, while that of LSF82 peaks in the range of 600 °C. However, it is not clear whether the increase in electronic conductivity results from the increased configurational entropy, or is simply a consequence of the incorporation of Co (as well as Ni and Cu) on the B-site.

(a)                                                        (b)
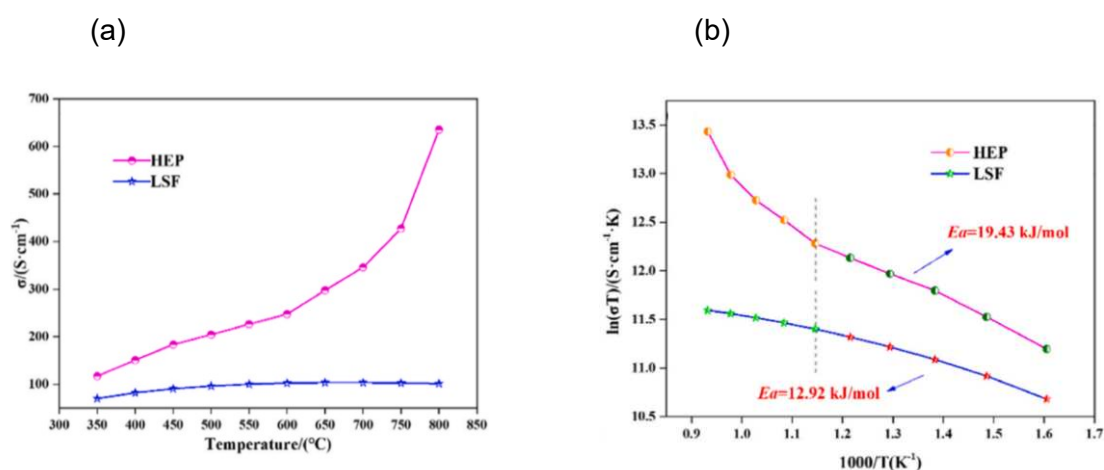


Figure 11: Comparison of electronic conductivity (a) and Arrhenius plot (b) of $La_{0.2}Pr_{0.2}Nd_{0.2}Sm_{0.2}Ba_{0.1}Sr_{0.1}Co_{0.2}Fe_{0.6}Ni_{0.1}Cu_{0.1}O_{3-\delta}$ and LSF82 [105].

Furthermore, electrochemical impedance spectroscopy (EIS) is conducted with symmetric cells. The principles of this measurement method are explained in detail in Chapter 3.4.2.2. Despite exhibiting higher electronic conductivity, the ohmic resistance of the HEP seems to be higher than that of LSF82. However, the polarization resistance is lower with the HEP cell than for LSF82, which shows that the redox activity is higher. The current density in SOFC mode at 800 °C and 0.7 V reaches 0.8 A cm$^{-2}$ [105].

B-site high entropy stabilized $La_{1-x}Sr_xCo_{0.2}Cr_{0.2}Fe_{0.2}Mn_{0.2}Ni_{0.2}O_{3-\delta}$ (x = 0, 0.1, 0.2, 0.3) is investigated within a study varying the Sr content of the composition. The electronic conductivity for x = 0.3 remains rather low at 16 S cm$^{-1}$. The current density at 0.7 V and 800 °C is below 0.5 A cm$^{-2}$, but was determined with an ESC and can therefore not be compared with the above mentioned results. No impedance spectroscopy data is given for the full cell test and therefore no conclusions regarding the origin of the performance can be drawn [106].

For medium entropy perovskites, the configurational entropy is between 1 R and 1.5 R. $SrFe_{0.25}Ti_{0.25}Co_{0.25}Mn_{0.25}O_{3-\delta}$ (SFTCM25) and $SrFe_{0.5}Ti_{0.2}Co_{0.2}Mn_{0.1}O_{3-\delta}$ (SFTCM5221) also show low electronic conductivity with 11 and 24 S cm$^{-1}$ respectively. However, the bulk diffusion coefficients are considered high enough for application as air electrode with a $D_{chem}$ in the range of 10$^{-5}$ cm$^2$ s$^{-1}$. At symmetrical cell level, the polarization resistance is measured for 140 h, during which a continuous increase is observed. As the increase is less for SFTCM25, which

shows higher configurational entropy, the authors claim this might be an evidence of the entropy stabilization effect. Despite the effect, provided SEM images might show structures attributable to Sr-segregation [107]. These results seem similar to those observed in [52].

## 3.4 Characterization techniques

### 3.4.1 Electronic conductivity and conductivity relaxation measurements

Material properties that are determined within this work include the electronic dc-conductivity, as well as the chemical surface exchange coefficient ($k_{chem}$) and the chemical bulk diffusion coefficient ($D_{chem}$) of oxygen. In this study, bar shaped samples are employed to determine the electrical dc-conductivity (EC) in linear 4-point geometry. Two contacts are used as current contacts, while the other two represent voltage probes. These probes carry no current, especially when a voltmeter with high internal resistance is used. This separation eliminates the contributions of contact and lead resistances, impacting only the burden voltage of the current-carrying contacts and not the potential of the probes. The sample must exhibit homogeneity in thickness and density, indicating an absence of isolated holes. Additionally, the contacts must be positioned along the length of the sample as shown in Figure 12.
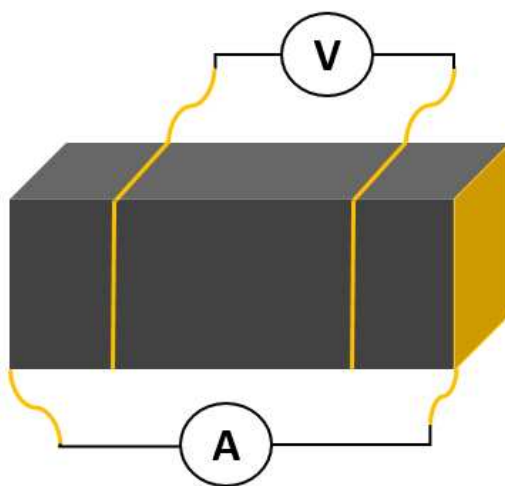


Figure 12: Bar shaped sample with measurement configuration for electronic dc-conductivity and conductivity relaxation measurements.

The distance between the voltage probes should be as large as possible to obtain maximum voltage signals. However, the probes should also maintain a certain distance from the current-carrying contacts to ensure homogenization of the current paths. Due to these opposing tendencies, the probes are contacted symmetrically at a distance of approximately one-third of the bar length. The electronic conductivity is determined via the specific resistance. A current is introduced at the edges of the bar. The potential difference is then measured between the two inner contacts.

The oxygen exchange kinetics is characterized using the dc-conductivity relaxation technique. The experiments can be done with the same bar shaped samples and measurement configuration as the electronic conductivity measurements. The sample is brought into equilibrium with its surrounding gas phase at a specific temperature and a given oxygen partial pressure. In this geometry, oxygen diffusion can occur in two directions through the sample. Due to the complete coverage of the faces of the bar shaped samples with gold sheets, oxygen

diffusion is blocked along this specific direction. The electronic conductivity of the sample is recorded over time. The obtained relaxation curve is described by Eq. 12.

$$\bar{\sigma}_t = \frac{\sigma_t - \sigma_0}{\sigma_\infty - \sigma_0}$$

(Eq. 12)

$\sigma_0$… equilibrium conductivity before $pO_2$ change

$\sigma_t$… conductivity at a certain time

$\sigma_\infty$… equilibrium conductivity after the $pO_2$ change

$\bar{\sigma}_t$… normalized conductivity

Once equilibrium is reached, the oxygen partial pressure in the gas phase is abruptly changed, either increased or decreased. If the oxygen partial pressure is increased, the material takes up oxygen, and a new equilibrium is established after a certain time. Conversely, the sample releases oxygen when the partial pressure is decreased. The change in oxygen content also alters the concentration of electronic charge carriers in the sample, affecting the electronic conductivity of the material. Diffusion coefficients and surface exchange coefficients of oxygen can be determined through nonlinear regression of the conductivity transient during the relaxation process. The principle is applicable only to minor changes in $pO_2$, while the change in conductivity should be significantly larger than the signal noises. The evaluation of $k_{chem}$ and $D_{chem}$ does not follow a strict physical correlation. In an ideal scenario, when both surface exchange and diffusion play comparable roles in the conductivity relaxation, both kinetic parameters can be derived simultaneously from the relaxation behavior. However, depending on sample geometry, it is possible for the relaxation process to be primarily influenced by either the surface exchange reaction or the diffusion within the solid. In other words, the oxygen exchange kinetics can be controlled either by surface processes or bulk diffusion, ultimately determining the rate of the reaction. The equations for fitting the obtained relaxation curves to obtain the kinetic parameters are given elsewhere [108,109].

### 3.4.2 Electrochemical characterization

Two different measurement setups are used within this work for electrochemical characterization: A Probostat (NORECS) and a FuelCon (Horiba) system.

The Probostat setup is used for short-term electrochemical characterization of button cells (symmetrical and full cells). The upper part of the system is shown in Figure 13. It comprises two concentric alumina tubes. The inner tube provides support for the cell and contains gas feed channels. This alumina part is attached onto a flexible spring construction at the button. In this way, mechanical load improves current collection. The outer tube separates the inner from the outer gas area. The SOC is positioned on top of the inner alumina tube. On each side of the cell, metallic meshes are used for current supply. Platinum wires, welded or mechanically

attached to the meshes, lead downward to connect with the system's electronics. Gas feed at the outer gas area is established with an outlet directly on top of the SOC. Gas tightness is ensured by a circular gold sealing mounted directly onto the outer tube. The SOC is held in place by an alumina disk attached to springs at the lower part of the Probostat.
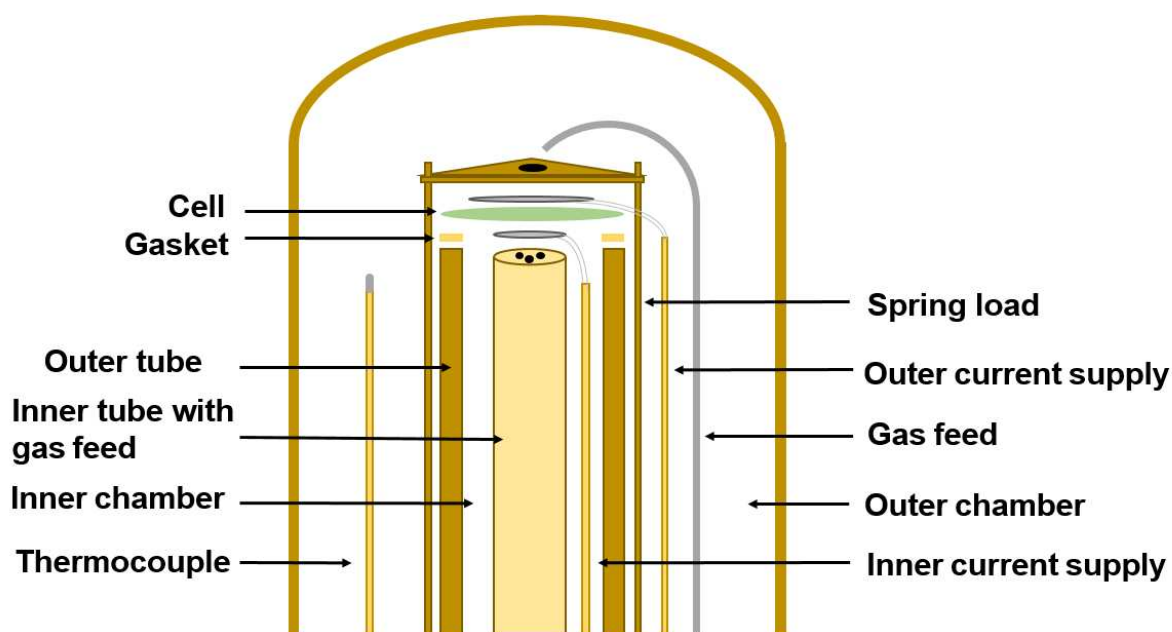


Figure 13: Top part of a Probostat setup for symmetrical and full cell testing.

Larger 5x5 cm² cells, especially for long-term electrolysis tests, are evaluated within a Horiba FuelCon Evaluator test setup. While the working principle corresponds to that of the Probostat, there are two main differences concerning gas flow and sealing. While in the ProboStat, the gas flow passes radially over the cells from the top, it is introduced horizontally in the FuelCon setup. This results in the possibility of varying gas compositions prevailing at different ends of the cells. Furthermore, no gold seals are used in the FuelCon test stand. Gas tightness is exclusively ensured through form-fitting alumina components, as well as mechanical load.

### 3.4.2.1 Current-voltage curves

As explained in Chapter 3.1.2, SOC exhibit certain irreversible processes that limit the energy conversion from chemical to electrical or vice versa. These processes judge the ratio between desired energy form (chemical or electrical energy) and heat produced. The limiting effects are subject to the current density applied to the system. Therefore, to judge the electrochemical performance of an SOC it is essential to assess the voltage response of the system when a current is applied. The result is a current-voltage curve, denoted as i-V curve, when using current densities. Other losses may be attributed to the experimental test setup. An important factor is gas leakage. While the electrolyte ensures gas tightness within the SOC, sealing is very important within the test setup as well. Leakage is an explanation for deviation of the experimentally measured OCV from the theoretical value obtained from the Nernst equation

(Eq. 3). In addition, partial enrichment of hydrogen at the air electrode can lead to reduction and phase decomposition of the air electrode material. The other way round, even spatially limited oxidizing conditions may oxidize Ni within the fuel electrode, which can result in cracks.

The electrochemical characteristics can be recorded in two different ways. The first is the galvanostatic mode, whereby a sweep in current intensities is executed and the system's voltage response is observed. This mode is used within this work for short-term characterization. It is important to vary the current as slowly as possible. Otherwise, capacitive effects within the test setup may influence the resulting i-V curve. Apart from the electrochemical insights gleaned from an i-V curve, it can also serve as a tool to monitor alterations in cell or electrode resistance during long-term stability experiments. For this purpose, the potentiostatic mode is used, where the voltage is controlled, and the resulting current output from the system is measured [110].

### 3.4.2.2 Electrochemical impedance spectroscopy

EIS is an analysis method for electrochemical systems. This method is employed, among other things, for studying ionic, electronic as well as charge transport processes in electrodes and electrolytes. Similar to other spectroscopic analysis methods, response signals in EIS are evaluated, which arise due to a defined signal function. The perturbation function used in EIS is an alternating current or alternating voltage signal, which provides a characteristic response signal altered by the studied cell. EIS is typically conducted over a wide frequency range from mHz to MHz and shown as Nyquist or Bode plot. The interpretation of impedance spectra is challenging, especially when characterizing full cells. Electrical equivalent circuits (EEC) are created for easier interpretation. In electrochemistry, they consist of ideal and non-ideal electrical elements such as resistors, capacitors, inductors, or constant-phase elements (CPEs), which are connected in series and/or in parallel. An important criterion for the validity of the EEC in describing an electrochemical system is that by adjusting the free parameters of the electrical elements (fitting), a good match with the experimentally determined frequency response can be achieved [111]. An example for an EEC, which is used within the present work, is shown in Figure 14.
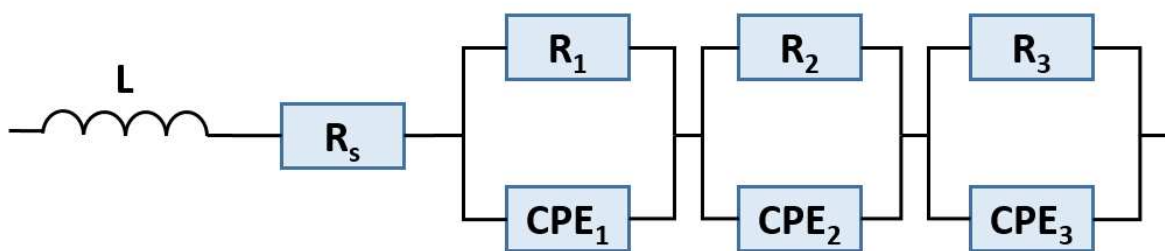


Figure 14: Electrical equivalent circuit with three constant phase elements, R denotes an ohmic resistance while L is an inductance.

The inductance L primarily accounts for the inductance of the measurement cables. The influence of L is noticeable in the high-frequency measurement range of impedance spectra as a tail-like section parallel to the imaginary axis. The horizontal offset of the spectrum from the diagram origin is described by the resistance $R_s$. This parameter essentially consists of contributions from the electrolyte and the contacts, however there may be an additional influence on this ohmic resistance part originating from the electrodes. The polarization resistance $R_{pol}$ of an SOC comprises the sum of the other listed serial resistance elements, in case of Figure 14 these are $R_1$ to $R_3$. CPEs are used within the equivalent circuit instead of capacities. Due to inhomogeneity in current flows, these elements describe the capacitive processes more accurately. As the nomenclature of this circuit element indicates, its phase angle is not a function of the frequency. The mathematical expression for the impedance of a CPE used within this work is given in Eq. 13.

$$Z = \frac{1}{Q\,(j\,\omega)^n}$$

(Eq. 13)

$Q$… parameter containing capacitance information

$j$ … $\sqrt{-1}$

$\omega$… angular frequency

Typically, the exponent n of the CPE can range from 0 to 1. The specific value of the exponent n characterizes different circuit elements represented by the CPE element. When n equals 1, the equation gives the impedance of a pure capacitor, while for n equal to 0, the impedance of an ideal resistor is derived. For each pair of parallel CPE and R elements, an effective capacity $C_{eff}$ can be calculated according Eq. 14 [112].

$$C_{eff} = Q^{\frac{1}{n}}\left(\frac{1}{R}\right)^{\frac{1-n}{n}}$$

(Eq. 14)

The R || CPE element results in a semicircle within the complex plane. The closer the exponent n gets to 0, the more the semicircle is depressed. An equivalent circuit with 3 R || CPE elements is meant to fit an impedance spectrum with 3 semicircles. Figure 15 shows an example for such a spectrum, which is recorded on a cell with Ni-YSZ fuel electrodes.
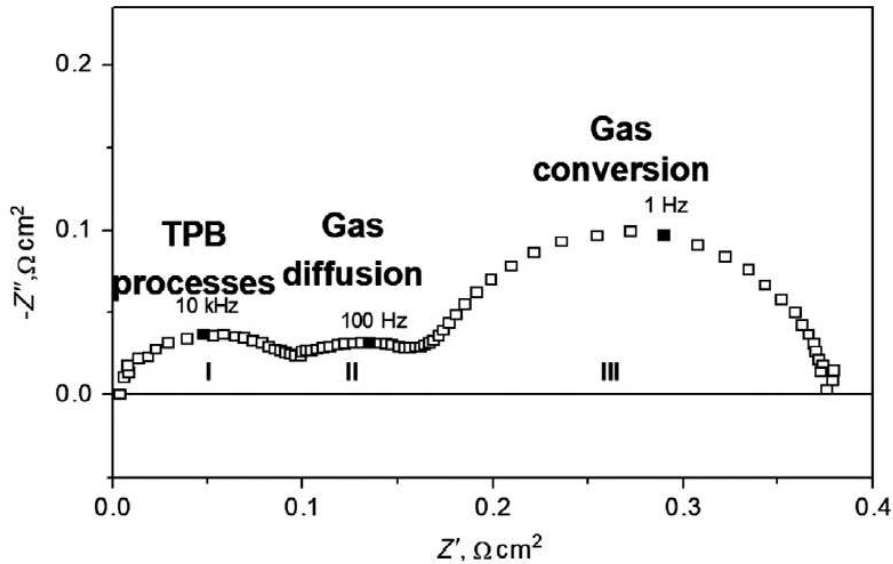
Figure 15: Impedance spectrum of Ni/YSZ fuel electrodes in three-electrode setup at 1,000°C described by [113].

As indicated by Figure 15, the semicircles originate from different processes correlated to the cell reactions. Lenser et al. [18] describe the spectrum in case of the fuel electrode, where the semicircle at the highest frequencies is typically associated with the electrochemical reaction at the triple phase boundaries. Impedance arcs at medium frequencies (with peak frequencies at 10–100 Hz) are attributed to gas diffusion and resulting concentration changes within the porous electrode. These two contributions depend on the electrode material and microstructure. A more extensive conversion arc, commonly observed in a lower frequency range around 1 Hz, is linked to gas composition changes outside the porous electrode and thus relies on gas flow characteristics in the stack design and test setup [18]. In case of the air electrode, [107] ascribes the low-frequency semi circles to molecular oxygen diffusion and the adsorption process. Processes in medium frequency range between 10 and 100 Hz can be originating from charge transfer processes. The arcs at frequencies in the kHz range can be related to oxygen ion transport from the air electrode to the electrolyte or vice versa [107].

Symmetrical cells are highly valuable for understanding the attributes of fuel and air electrodes, respectively. Nevertheless, relying on symmetric cells for single electrode studies does not allow accurate predictions of the full cell performance. While data from symmetric cells can be interpreted qualitatively, their use in a quantitative manner is not advisable. When comparing the impedance measurements of electrode resistance between symmetrical cells and full cells, it is observed that the cumulative polarization resistances from symmetrical cells are higher than those from full cells. The variation in electrode characteristics can be attributed to differences in microstructure or impurity levels resulting from manufacturing processes. This highlights the importance of thoroughly characterizing electrodes at the full cell level [114].

At full cell level, it is however challenging to attribute arcs to the performance of specific cell components. An example is given in [114] and Figure 16, wherein cells with LSM/YSZ air

electrode and Ni/YSZ fuel electrode are investigated. The two full cells show completely different characteristics although both are manufactured identically. The $R_s$ of the worse performing cell is notably higher compared to that of the superior cell. Besides the difference in $R_s$, an increase in both $R_{p,cathode}$ and $R_{p,anode}$ is also noted. Impedance measurements are conducted at temperatures of 850, 800, 750, and 700 °C. For the worse performing cell, $R_s$ accounts for 23% of the total resistance at 700 °C and for 30% at 850 °C. In contrast, the well performing cell exhibits a different behavior, with $R_s$ contributing only 14% to the total resistance at both high and low temperatures. The observed differences between the two cells primarily originate from variations in microstructure. In the underperforming cell, significant agglomerations of YSZ are detected within the composite air electrode. These agglomerations lead to an elevation in the polarization resistance of the air electrode, as they reduce the effective TPB length per unit cell area. Additionally, due to their substantial size, a shadowing effect occurs on the anode side, further increasing the polarization resistance of the anode. Two explanations are provided for the increase in $R_s$: First, there is a considerable electrical loss associated with in-plane transport in the electrolyte. Second, these flaws introduce in-plane currents in the air electrode, creating an $R_s$ that exhibits weak temperature dependence [114].
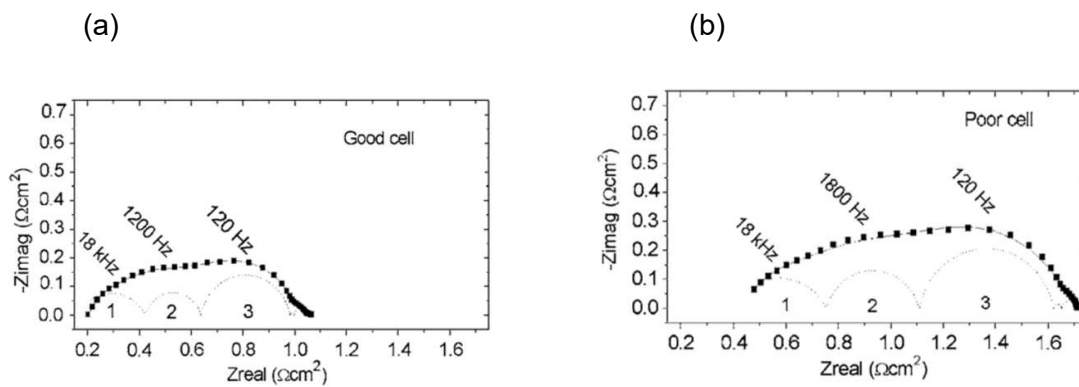


Figure 16: EIS of two similarly manufactured full cells with LSM/YSZ air electrode (a) and Ni/YSZ fuel electrode (b). The semicircles show the fit using three R || CPE elements [114].

The association of the polarization resistances with the specific electrodes is done by variations in gas feed. It is observed which of the arcs is affected by changes either at the air or fuel electrode side. At lower frequencies, when the concentration disturbance extends into the flow channel, the behavior is significantly influenced by the flow rate or the geometry of the test setup. At very high flow rates and constant composition of the gas, only pore diffusion is observed as impedance [115].

# 4 Research strategy

This chapter describes the approach of the present thesis. Initially an overview about the different steps of the development process is given. The introduction is followed by a more specific section about the applied measures to adapt the general research strategy to the high entropy perovskites in concern.

## 4.1 Definition of the research process flow

The methodology for the development process is divided into 5 main steps, which can partially be executed in parallel as shown in Figure 17. The first part is the choice of material, which mainly concerns the active air electrode material. The synthesis of the targeted material is followed by a calcination process to remove volatile compounds from the obtained powder. To check if the targeted structure was obtained, an XRD analysis is performed followed by Rietveld refinement. From the diffractogram, conclusions can be drawn as to whether the calcination temperature needs to be adjusted. Higher temperatures or compacting the powder before heating could contribute to the formation of the desired structure since it facilitates cation diffusion. This is followed by processing of the powder to adjust its morphology to the desired microstructure and paste viscosity. In the course of paste preparation, additives such as pore formers can also be added to the active powder. Via screen printing, the paste is applied to a substrate. Initially, symmetric cells are manufactured, using a relatively thick GDC pellet as an electrolyte to give the cell mechanical stability. On both sides the same electrode layer is printed. Through impedance measurements and mechanical assessment of the adhesion of the sintered electrodes, first conclusions about the expected performance of the material can be drawn. SEM analyses at this stage enable adjustments to the microstructure. The use of symmetric cells before full cells offers several advantages: (i) the experiments are more cost effective; (ii) production can be entirely carried out with the available laboratory equipment; (iii) the surfaces of the GDC pellets can be ground if necessary and thus the substrates can be reused; (iv) the tests are quick and efficient to implement; (v) there is no need for a reduction process or seals in general. Then, the most successful electrode designs are transferred from symmetric cells to full cells. Two formats are examined: button cells with a substrate diameter of 2 cm and a square cell format with 5 cm side lengths. Both types of substrates are of commercial origin, while the air electrodes are printed in-house. Full button cells are used to verify the electrochemical performance at full cell level. Short-term tests are conducted, in which i-V characteristics are recorded in both the SOEC and SOFC modes. Impedance measurements serve to identify the resistance contributions of individual cell components. In general, EIS was performed under load to obtain comprehensive information about the cell behavior, which is not sufficiently possibly at OCV [116]. The most promising approaches are further investigated through long-term studies. A practical operating condition is selected and it is maintained for several hundred hours to simulate application-relevant conditions. Post-test analysis primarily involves SEM and EDX. Additionally, characterization of fundamental material parameters is conducted, including oxygen exchange kinetics and electronic conductivity. A schematics of the research process including various analysis methods is given in Figure 17.
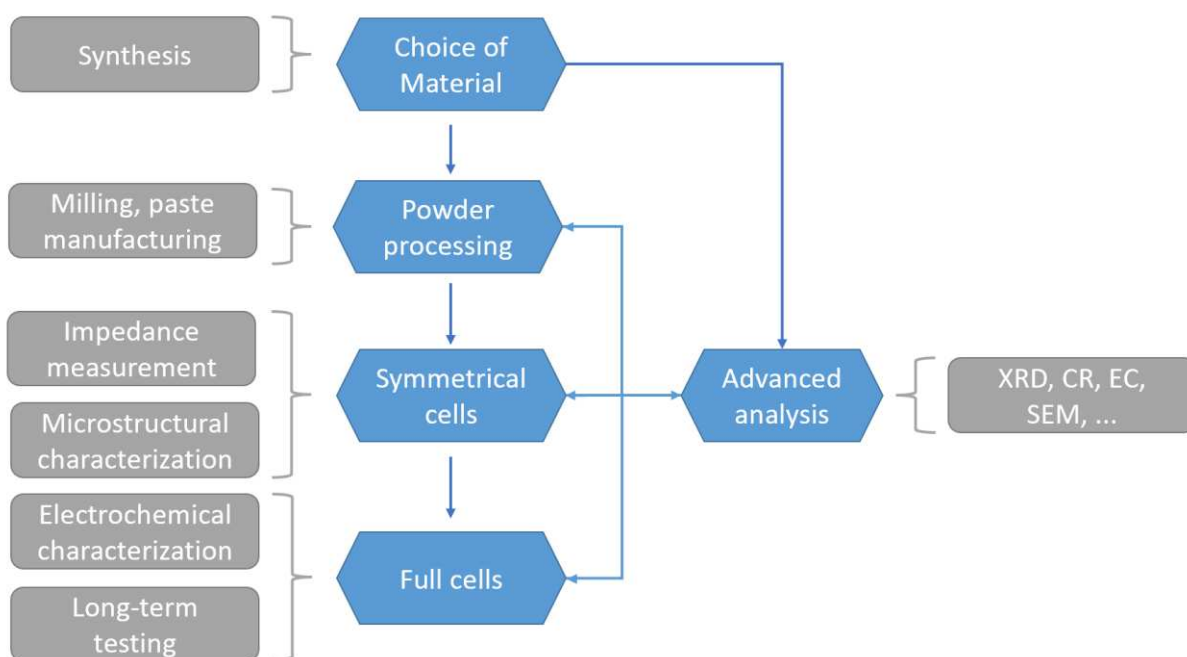
Figure 17: Illustration of the research process within the present doctoral thesis.

## 4.2 Application of the process flow within the thesis

The research within the thesis was based on the above shown process and applied to the class of HEP. Various criteria were taken into account when determining the elemental composition of the perovskites. In each case, the overriding goal was achieving both high power densities and good long-term stability. According to the available literature, stabilization effects and enhanced conductivity, which are attributed to high entropy perovskites seem to occur particularly in compounds that contain 5 or more elements on the A-site [94,117,118]. As shown in Table 1, the variety of elements with appropriate ionic radius for occupying the perovskite lattice's A-site is mostly limited to lanthanides and alkaline earth elements. Additionally, trends regarding the expected surface exchange coefficient or stability of perovskites containing certain elements, available in the literature, were taken into account during the selection process [119]. Doping with $Sr^{2+}$ or $Ba^{2+}$ enhances oxygen diffusion via creating vacancies, while Co at the B-site increases electronic conductivity and catalytic activity [120-122]. Because of these conclusions, the decision was made to investigate the high entropy stabilized compounds $La_{0.2}Pr_{0.2}Nd_{0.2}Sm_{0.2}Sr_{0.2}Co_xFe_{1-x}O_{3-\delta}$ ($0 \leq x \leq 1$), which are HEP analogs of the low entropy $La_{0.8}Sr_{0.2}Co_xFe_{1-x}O_{3-\delta}$ series. High current densities are reported for perovskites with solely Co at the B-site [35,104]. Therefore, the approach of this thesis was first to explore the limits of high entropy perovskites $La_{0.2}Pr_{0.2}Nd_{0.2}Sm_{0.2}Sr_{0.2}CoO_{3-\delta}$ (LPNSSC). To answer the initially raised research questions, Co was then substituted with Fe towards less critical elemental compositions. These perovskites were extensively investigated as SOC air electrode and exhibit a solid benchmark for novel high entropy compounds.

In order to validate the processing workflow and setup for cell testing, commercial $La_{0.6}Sr_{0.4}Co_{0.2}Fe_{0.8}O_{3-\delta}$ (LSCF6428) powder (prepared by EMPA, Switzerland) was used to manufacture full cells as benchmark. A comparison between experimental results and literature data of LSCF6428 is shown in Figure 18 (a). All the cells were tested using diluted Pt-paste as contacting agent at the air electrode. The cell labelled "Sinter++" was sintered at 1200°C, while "Sinter+" and "Sinter-" correspond to 1080 and 1060°C, respectively. A SEM cross section image of the cell "LSCF Sinter++" is shown in Figure 18 (b). A continuous layer of SZO was formed in between the YSZ electrolyte and the GDC barrier. Therefore, the electrochemical performance was the worst of all cells tested.

(a)                                                            (b)
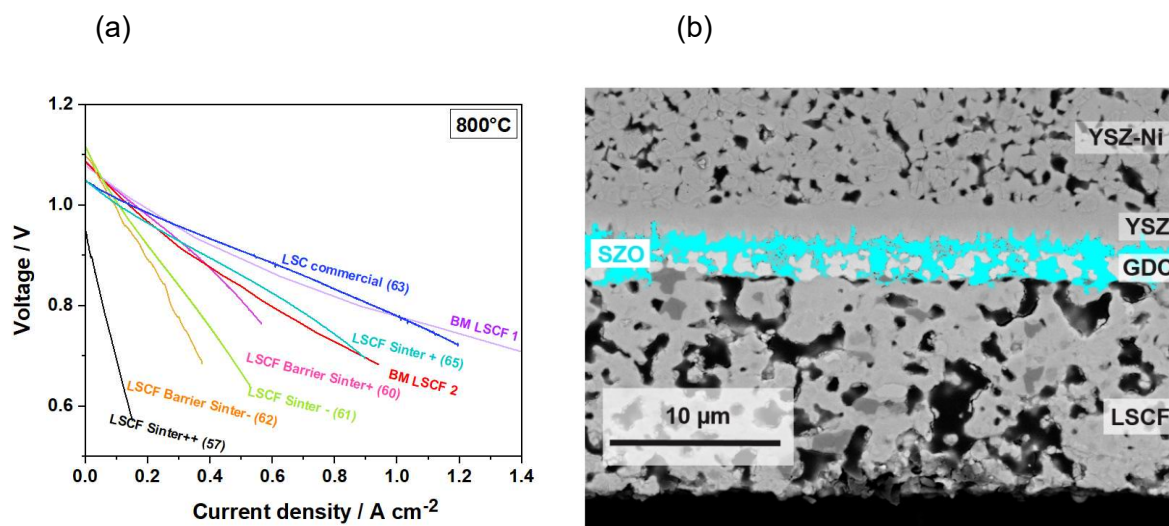


Figure 18: Progress in cell testing in SOFC mode to meet the benchmarks (BM) of commercial LSC and LSCF based cells (a). Numbers in brackets are internal nomenclature. Terms after the air electrode material refer to different sintering temperatures, which are described in the text. Data of benchmark cells BM LSCF 1 [123] and BM LSCF 2 [124] is taken from literature. The SEM image shows an example of a cross section of cell "LSCF Sinter++" with distinct SZO formation (b). Coloring was added for better differentiation.

In order to avoid SZO formation, it was tried to pre-sinter the cell substrate at 1400°C to densify the diffusion barrier layer as suggested in literature [76]. These samples are labelled with "Barrier" in Figure 18. However, the strategy turned out to be inefficient and had even a negative influence on electrochemical performance. Among the cells with in-house prepared air electrodes, "LSCF Sinter+" performed best and meets the benchmark for LSCF6428 cells set by [124]. A commercially available cell with LSC air electrode showed similar current densities as a higher literature benchmark [123]. These results not only verified the cell testing equipment, but also created awareness that even minor changes in sintering temperature can have an impact on cell performance. This highlights the necessity of manufacturing and testing symmetrical cells. As quick and economic opportunity for pre-testing this method is a key part of the development process shown in Figure 17.

An example of a study with symmetrical cells aiming at defining the most suitable sintering temperature is shown in Figure 19. Various cells with LPNSSC air electrodes were evaluated

using the principle introduced in Chapter 3.4.2. In this case, a minimum of the mean polarization resistance was found for cells sintered at 1070°C. Below this temperature, there is a risk of insufficient adhesion between the active layer and the GDC substrate. It should be noted that the effect of SZO formation cannot be evaluated using symmetrical cells with GDC electrolytes, as no YSZ is present. Therefore, the final decision of the sintering temperature should be made on the lowest possible one emerging from the sinter study. This process was supported by dilatometry measurements that detect shrinkage rate during increase of temperature.
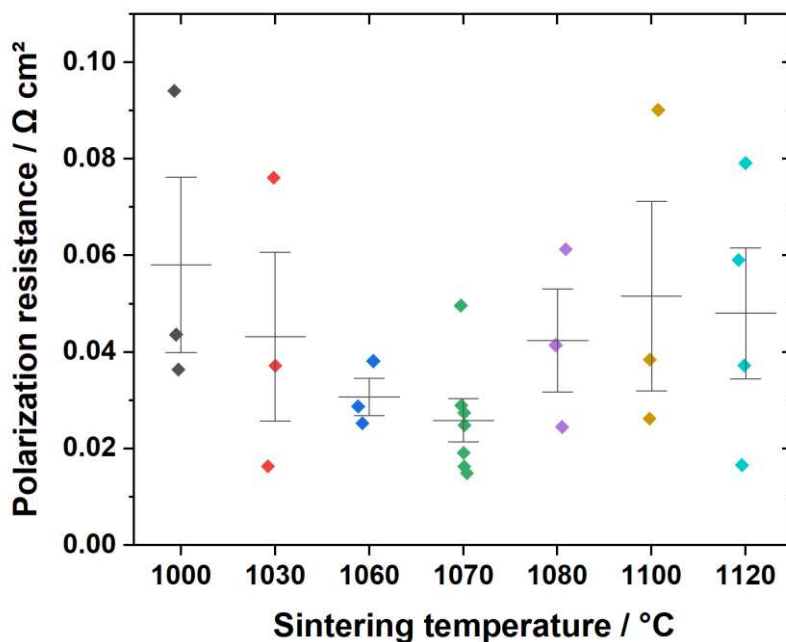


Figure 19: Polarization resistances of symmetrical cells with LPNSSC electrodes prepared at different sintering temperatures.

Button cells were tested using a standardized reduction program to reduce the NiO in the as-prepared fuel electrodes to metallic Ni. All HEP button cells were electrically contacted using gold meshes without contact pastes. Electrochemical characterization at button cell level was done in both SOFC and SOEC mode. Although the focus of the thesis is mainly on the production of green hydrogen by SOEC, some conclusions like temperature dependence on performance or morphological conclusions can more efficiently be drawn in SOFC mode. Simulations suggest that optimizations regarding grain size, porosity, and layer thickness exhibit similar trends in both SOFC and SOEC modes. This implies that the improvements achieved in SOFC operation can be assumed advantageous for electrolysis operation as well [125,126], although it is not possible to fully predict performance in SOEC mode drawing conclusions only based on SOFC data [127]. In the SOFC mode, the transport or diffusion of oxygen at the air electrode can be influenced by the inflow of air. By observing the achievable current densities and the behavior during EIS with variations in the supply of oxygen gas for the cell reaction, conclusions can be drawn about how well the morphology of the cell allows oxygen utilization. A case study is shown in Figure 20, where the airflow is varied from 50 to 500 ml min$^{-1}$ for a La$_{0.2}$Pr$_{0.2}$Nd$_{0.2}$Sm$_{0.2}$Sr$_{0.2}$Co$_{0.5}$Fe$_{0.5}$O$_{3-\delta}$ (LPNSSCF) full cell while fuel flow (H$_2$)

is kept at 40 ml min^{-1}. The cell performance is significantly influenced by the change in airflow. The growth of the semicircle at low frequencies, which can be seen in Figure 20 (b), corresponds to concentration polarization [128,129]. The longer high current densities can be maintained, meaning the lower the concentration polarization while decreasing the airflow, the more effective the microstructure of the air electrode. Similar experiments were conducted in literature, where the oxygen partial pressure was minimized in the gas flow of the air electrode [107].

At least once for each novel HEP air electrode material, current density curves are recorded within a temperature range of 800 to 650°C (with steps of 50°C). When EIS is conducted at different temperatures, conclusions can be drawn regarding the activation energies of individual cell processes. This enables the assignment of individual semicircles to their respective origins.

(a)                                                    (b)
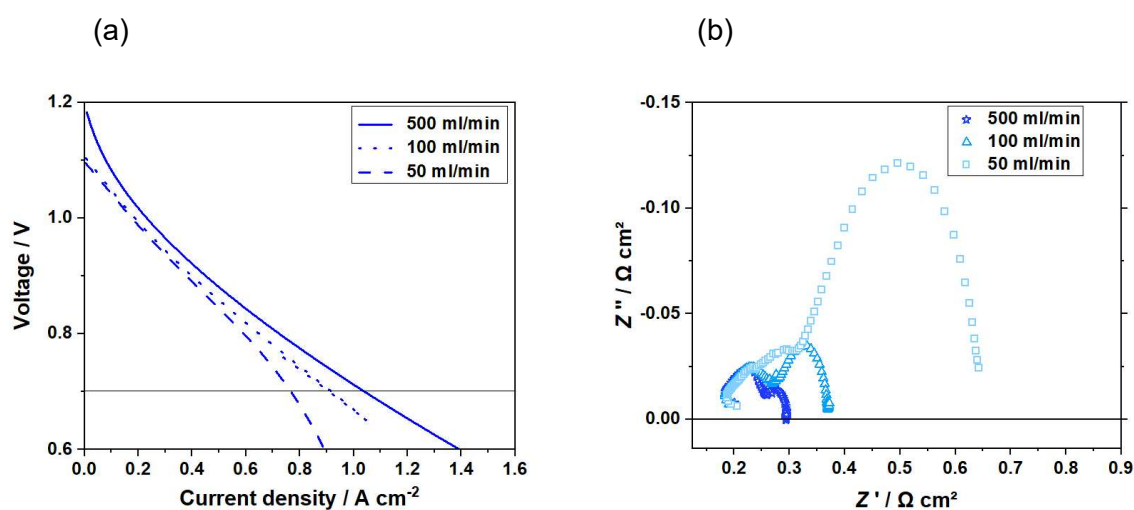


Figure 20: Current density-voltage curve (a) and EIS at 0.7 V (b) of a full cell with LPNSSCF air electrode with LNF current collector layer. Airflow is given in the legends, while $H_2$ flow was kept at 40 ml min^{-1} for all measurements at the fuel electrode.

Long-term tests were conducted with 5x5 cm² cells in SOEC mode. Taking the considerations explained in Chapter 3.1.3 into account, every electrolysis test was done at 80% humidification (rest $H_2$), aiming at 1 kh of continuous operation. At regular intervals, impedance spectra and i-V characteristics were recorded to assess the progression of degradation regarding the affected cell components [116]. Regardless of current density, operational voltage was set to 1.1 V at the start of each test. The test setup of FuelCon works with ambient air instead of synthetic air. Consequently, air impurities like sulphur dioxide, which may harm the air electrode in real operating conditions, can also affected these long-term tests.

According to the research process introduced in Chapter 4.1, SEM and EDX images of the examined cells and cell components were acquired. Characterization by SEM/EDX started with analysis of the synthesised powder via imaging, included analysis of pre-sintered symmetrical cells, as well as post-test analysis of long-term tested cells. These images were primarily taken in cross section, but surface analyses of air electrodes were also conducted to

evaluate porosity and impurities. An example of a SEM/EDX surface analysis is shown in Figure 21, where a 5x5 cm² cell with $La_{0.6}Sr_{0.4}CoO_{3-\delta}$ (LSC64) air electrode is investigated after long-term electrolysis. The analysis indicates that Pt is deposited at the electrode surface. The Pt originates from a Pt-mesh that was used for electrical contacting of 5x5 cm² cells in the FuelCon test setup. The effect is well known in literature, but no degradation issues are linked to Pt enrichment at the air electrode surface [130]. For this reason, and due to cost considerations, it was decided not to replace platinum grids with gold grids in the testing of 5x5 cm² cells. Only full button cells and symmetrical cells were exclusively tested with gold contacts.

(a)                                             (b)
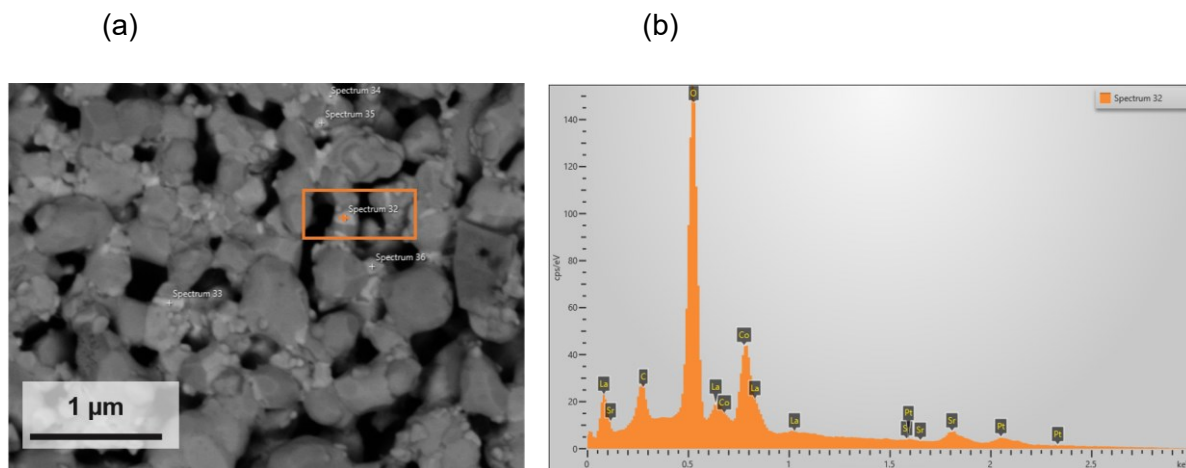


Figure 21: SEM surface image of an LSC64 air electrode on a 5x5 cm² cell (a) and EDX spectrum of the highlighted area (b) indicating the deposition of Pt.

Another key topic targeted by SEM analysis is morphology. Exemplarily, this can be demonstrated through experiments involving pore formers. Carbon, which is added to the screen printing paste, burns out during the sintering process, leaving behind a porous electrode structure. Figure 22 shows SEM images before and after the sintering of such an electrode layer. Adjustments to the porosity can be made through the shape and size of the carbon particles.
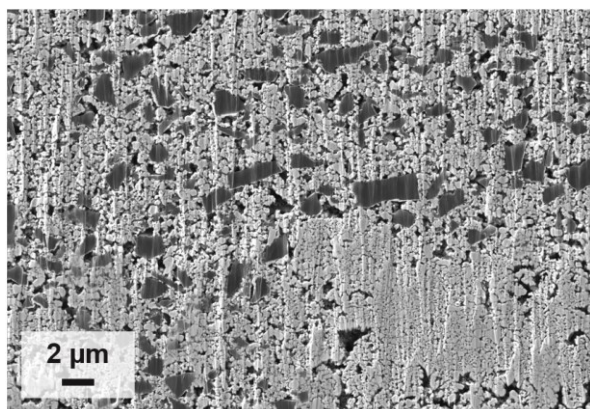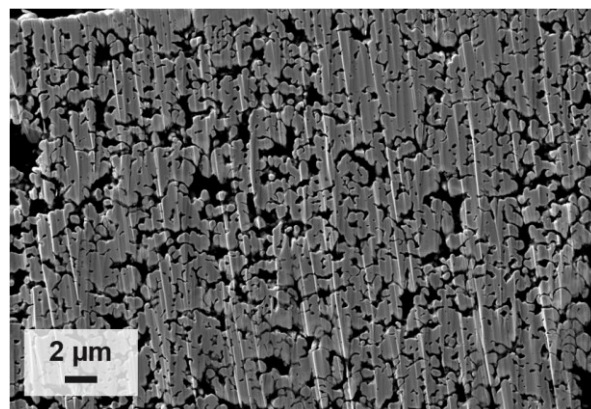
Figure 22: SEM cross section images of a symmetrical cell with LPNSSC air electrode and carbon pore former before (a) and after sintering (b).

Conductivity relaxation measurements for determining $k_{chem}$ and $D_{chem}$, as well as electronic conductivity, are also addressed as part of the material analysis. Inferences from these experiments are used to interpret results of the electrochemical cell characterization. It may be considered to compensate for low ionic conductivity of the active electrode material by incorporating composites with the electrolyte/barrier material GDC, but this was not an issue investigated in the thesis. The issue of low electronic conductivity was, however, extensively dealt with in the present work, wherein composites with more conductive materials and a current collector layer were developed.

# 5 Summary, conclusions and outlook

In the present thesis, HEP air electrode materials for SOC were investigated. The focus of the work was on the SOEC mode, although some investigations were also conducted in the SOFC mode. A series of high entropy perovskites was tailored in terms of elemental composition, morphology, and electrode design with the aim of achieving high power densities while maintaining good long-term stability. In particular, this should be achieved when reducing the Co content at the B-site of the perovskite series $La_{0.2}Pr_{0.2}Nd_{0.2}Sm_{0.2}Sr_{0.2}Co_xFe_{1-x}O_{3-\delta}$ ($0 \leq x \leq 1$). Compounds from the analogous low entropy perovskite series $La_ySr_{1-y}Co_xFe_{1-x}O_{3-\delta}$ were used for comparison. The latter generally exhibit promising electrochemical performance but have well-known weaknesses in long-term stability, especially in electrolysis mode [70,131]. The development of new materials was advanced according to a research process elaborated during the thesis.

After the successful synthesis of the targeted HEP, structural analysis with X-ray powder diffraction and Rietveld refinement provided insights into the phase purity and crystal structure. The oxygen exchange kinetics and electrical conductivity were evaluated using conductivity (relaxation) experiments in linear four-point or van der Pauw geometry. Morphological and chemical adjustments were evaluated on symmetrical cells with EIS and subsequent SEM analysis. Electrochemical investigations were conducted with button cells with 2 cm diameter and 5x5 cm² cells obtained by screen printing of the novel electrodes on commercial ASC substrates. Button cells were used for fundamental characterization of the electrodes under different operating conditions, while long-term tests in the electrolysis mode under application-relevant conditions were conducted with the 5x5 cm² cells. Following the outlined research process, the questions raised at the beginning of this thesis were addressed.

*Research question 1: Do air electrodes based on high entropy perovskites prove long-term stable in SOEC operation mode?*

➢ HEP air electrodes are long-term stable in electrolysis mode. During the course of this work, the compositions $La_{0.2}Pr_{0.2}Nd_{0.2}Sm_{0.2}Sr_{0.2}Co_xFe_{1-x}O_{3-\delta}$ ($x = 0$ and $x = 1$) were studied in long-term tests, refer to original publications 1 [132] and 2 [133]. In both cases, with solely Co and with solely Fe on the B-site, no degradation attributable to the air electrode was observed. A 5x5 cm² cell with LPNSSF air electrode was held under continuous polarization of -0.69 A cm$^{-2}$ where it showed a low degradation rate of 0.8% per 1,000 h. While conducting electrolysis, EIS measurements were performed multiple times. The peak frequencies of the resulting semicircles correspond to initial degradation effects of the fuel electrode, as well as to an increasing porosity of the diffusion barrier layer. The decrease in the density of the GDC layer might be less critical compared to other air electrode materials, as no formation of SZO was observed. During the long-term test of a 5x5 cm² cell with LPNSSC air electrode, no significant increase in cell voltage was observed over extended time periods during electrolysis. The cell was operated at -0.94 A cm$^{-2}$ and post-test examination via SEM cross section revealed no morphological differences compared to the air electrode in

an equivalent fresh cell. Quite different observations were made during the test of a commercial cell with LSC64 air electrode in the same setup under the same test conditions: The operating voltage increased almost linearly over the entire test period and was > 2% per 1,000 h. SEM images revealed delamination of the air electrode, a well-known failure mechanism in SOECs. Regarding strontium segregation, EDX analyses demonstrated that approx. 50% fewer strontium-containing secondary phases are formed on the electrode surface. However, it could not be determined whether this effect is favored by high entropy stabilization or solely due to the lower Sr content of the HEP.

*Research question 2: Can air electrodes based on high entropy perovskites outperform their state of the art (low entropy) analogs?*

➢ The question must be answered under consideration of the fact that different operating conditions of cells can lead to contrasting results. When comparing cell performance, it is essential that the same operating parameters prevail. Within the scope of this thesis, cells with LPNSSC air electrodes exhibited the best electrochemical performance in SOFC and SOEC mode. At a flow rate of 100 ml min$^{-1}$ synthetic air and 40 ml min$^{-1}$ H$_2$, the best ASC button cells with LPNSSC air electrode reached 1.75 A cm$^{-2}$ at 0.7 V in SOFC mode, and -1.56 A cm$^{-2}$ at 1.2 V in SOEC mode with a flow rate of 40 ml min$^{-1}$ H$_2$ with 70% humidification. Cells with LPNSSC air electrode seem even superior to LSC64. At comparable test conditions, a commercial 5x5 cm² cell with LSC64 air electrode reached -1.32 A cm$^{-2}$ in SOEC at 1.2 V and a flow rate of 1 l min$^{-1}$ H$_2$ and 80 % humidification, while current density for a 5x5 cm² cell with LPNSSC air electrode was -1.44 A cm$^{-2}$ at the same operational voltages and flow rates. These results are presented and discussed in original publication 1 [132].

➢ In case of cells with LPNSSF or LPNSSCF air electrodes, it is more difficult to compare the electrochemical performance with their low entropy analgos. These perovskites exhibit lower electronic conductivity, resulting in a significant increase in the ohmic part of their impedance. The electrodes could be contacted with metallic pastes to reduce the in-plane resistance. However, the catalytic nature of this layer would likely have a significant impact on the cell performance [134]. Another option is to operate the cell with a ceramic CCL as done within this thesis. However, the cell performance also depends on the conductivity and microstructure of the CCL. It was demonstrated in the present thesis that application of an optimized CCL can boost cell performance, but that a suboptimal CCL may block oxygen diffusion. These results are presented and discussed in original publication 2 [133].

*Research question 3: Which trends in oxygen exchange kinetics and electronic conductivity do the high entropy perovskites in concern show when substituting Co with Fe?*

➢ The chemical diffusion coefficient of oxygen ($D_{chem}$) does not change with variation of the B-site elements from Co to Fe, or with variation of $pO_2$. This is as expected and is further discussed in original publication 3 [135]. Between 650 and 850°C, $D_{chem}$ values range from $7\times10^{-7}$ to $1\times10^{-5}$ $cm^2$ $s^{-1}$. The chemical surface exchange coefficient of oxygen ($k_{chem}$) shows a pronounced dependence on the Co content, highlighting the catalytic effect of cobalt on the surface exchange kinetics. In the case of LPNSSC, a maximum value of $7.7\times10^{-4}$ cm $s^{-1}$ is found at 800°C and a $pO_2$ of $10^{-3}$ bar, representing an increase of over 20-fold compared to LPNSSF ($3.4\times10^{-5}$ cm $s^{-1}$ under the same conditions). The electronic conductivity (EC) decreases significantly with the substitution of Co with Fe. For LPNSSC a value of 1390 S $cm^{-1}$ is found at 800 °C and $10^{-2}$ bar $O_2$, while 75 S $cm^{-1}$ is obtained for LPNSSF. The trends and magnitudes of $k_{chem}$ and EC of all investigated HEP are in accordance with those of the low entropy analogs from the $La_ySr_{1-y}Co_xFe_{1-x}O_{3-\delta}$ ($0 \le x$, $y \le 1$) series [136,137], while LPNSSC surpasses the EC of LSC82 (1250 S $cm^{-1}$ at 800°C in air [138]).

In conclusion, the HEP material class proves an excellent choice for SOC air electrodes. Under the same test conditions, full cells with LPNSSC air electrodes even achieve higher current densities than cells with LSC64 electrodes. Although LPNSSF might not be used as standalone layer on the air electrode side due to its rather low electronic conductivity, tailoring the electrode design with suitable CCL and adjusting its morphology makes the performance of this sustainable Co-free material competitive. Summarily, HEP materials demonstrate excellent performance and good long-term stability as air electrodes for solid oxide cells. Therefore, further fundamental and application-relevant search should be conducted on HEP, and corresponding electrodes with various designs should be tested for developing even better SOC – as a step forward towards high volume green hydrogen production.

# 6 References

[1]     K.-F. Aguey-Zinsou, M. Costalin, Q. Lai, C. Pratthana, N. Rambhujun, M.S. Salman, P. Sapkota, T. Wang, *MRS Energy & Sustainability* **2020**, *7*, E33.

[2]     IEA, Global Hydrogen Review 2023, IEA, Paris, **2023**.

[3]     S. Luidold, H. Antrekowitsch, *JOM* **2007**, *59*, 20.

[4]     A. Bhaskar, M. Assadi, H. Nikpey Somehsaraei, *Energies* **2020**, *13*, 758.

[5]     L. Holappa, *Metals* **2020**, *10*, 1117.

[6]     H. Pauna, D. Ernst, M. Zarl, M. Aula, J. Schenk, M. Huttula, T. Fabritius, *Journal of Cleaner Production* **2022**, *372*, 133755.

[7]     K.C. Sabat, A.B. Murphy, *Metallurgical and Materials Transactions B* **2017**, *48*, 1561.

[8]     T. Schmidt, *Wasserstofftechnik: Grundlagen, Systeme, Anwendung, Wirtschaft*, Carl Hanser Verlag GmbH & Company KG, **2020**.

[9]     P. Millet, *Hydrogen Production* **2015**, *1*, 33.

[10]    C. Graves, S.D. Ebbesen, M. Mogensen, K.S. Lackner, *Renewable and Sustainable Energy Reviews* **2011**, *15*, 1.

[11]    S. Ebbesen, S. Jensen, A. Hauch, M. Mogensen, *Chemical Reviews* **2014**, *114*, 38.

[12]    J. Kim, H. Lee, B. Lee, J. Kim, H. Oh, I.-B. Lee, Y.-S. Yoon, H. Lim, *Energy Conversion and Management* **2021**, *250*, 114922.

[13]    M.C. Tucker, *International Journal of Hydrogen Energy* **2020**, *45*, 24203.

[14]    M.E. Chelmehsara, J. Mahmoudimehr, *International Journal of Hydrogen Energy* **2018**, *43*, 15521.

[15]    G. Kaur, *Solid Oxide Fuel Cell Components: Interfacial Compatibility of SOFC Glass Seals* **2016**, 43.

[16]    L. Ba, X. Xiong, Z. Lei, Z. Yang, B. Ge, L. Hu, Y. Jin, S. Peng, *International Journal of Hydrogen Energy* **2022**, *47*, 12469.

[17]    A. Hauch, R. Küngas, P. Blennow, A.B. Hansen, J.B. Hansen, B.V. Mathiesen, M.B. Mogensen, *Science* **2020**, *370*, 6118.

[18]    C. Lenser, D. Udomsilp, N.H. Menzler, P. Holtappels, T. Fujisaki, L. Kwati, H. Matsumoto, A.G. Sabato, F. Smeacetto, A. Chrysanthou, S. Molin in: O. Guillon (Ed.), Advanced Ceramics for Energy Conversion and Storage, Elsevier, **2020**, p. 387.

[19]    B. Königshofer, M. Höber, G. Nusev, P. Boškoski, C. Hochenauer, V. Subotić, *Journal of Power Sources* **2022**, *523*, 230982.

[20]    M.A. Laguna-Bercero, V.M. Orera, *International Journal of Hydrogen Energy* **2011**, *36*, 13051.

[21]   Y. Yang, X. Tong, A. Hauch, X. Sun, Z. Yang, S. Peng, M. Chen, *Chemical Engineering Journal* **2021**, *417*, 129260.

[22]   Y. Wang, W. Li, L. Ma, W. Li, X. Liu, *Journal of Materials Science & Technology* **2020**, *55*, 35.

[23]   S.E. Wolf, F.E. Winterhalder, V. Vibhu, L.B. de Haart, O. Guillon, R.-A. Eichel, N.H. Menzler, *Journal of Materials Chemistry A* **2023**, *11*, 17977.

[24]   H. Kozuka, K. Ohbayashi, K. Koumoto, *Science and Technology of Advanced Materials* **2015**, *16*, 026001.

[25]   A. Niemczyk, K. Świerczek, *E3S Web of Conferences* **2019**, *108*, 01019.

[26]   S.C. Singhal, K. Kendall, *High-Temperature Solid Oxide Fuel Cells: Fundamentals, Design and Applications*, Elsevier, **2003**.

[27]   V.A.C. Haanappel, J. Mertens, D. Rutenbeck, C. Tropartz, W. Herzhof, D. Sebold, F. Tietz, *Journal of Power Sources* **2005**, *141*, 216.

[28]   M. Kusnezoff, N. Trofimenko, M. Müller, A. Michaelis, *Materials* **2016**, *9*, 906.

[29]   K.V. Galloway, N.M. Sammes in: J. Garche (Ed.), Encyclopedia of Electrochemical Power Sources, Elsevier, **2009**, p. 17.

[30]   S.P. Jiang, *Journal of Materials Science* **2008**, *43*, 6799.

[31]   J. Mizusaki, Y. Yonemura, H. Kamata, K. Ohyama, N. Mori, H. Takai, H. Tagawa, M. Dokiya, K. Naraya, T. Sasamoto, H. Inaba, T. Hashimoto, *Solid State Ionics* **2000**, *132*, 167.

[32]   S. Carter, A. Selcuk, R.J. Chater, J. Kajda, J.A. Kilner, B.C.H. Steele, *Solid State Ionics* **1992**, *53-56*, 597.

[33]   T. Suzuki, M. Awano, P. Jasinski, V. Petrovsky, H. Anderson, *Solid State Ionics* **2006**, *177*, 2071.

[34]   Z. Shao, M.O. Tadé, *Intermediate-Temperature Solid Oxide Fuel Cells: Materials and Applications*, Springer Berlin Heidelberg, **2016**.

[35]   F. Zhao, L. Zhang, Z. Jiang, C. Xia, F. Chen, *Journal of Alloys and Compounds* **2009**, *487*, 781.

[36]   F. Zhao, R. Peng, C. Xia, *Materials Research Bulletin* **2008**, *43*, 370.

[37]   H. Ullmann, N. Trofimenko, F. Tietz, D. Stöver, A. Ahmad-Khanlou, *Solid State Ionics* **2000**, *138*, 79.

[38]   F. Prado, T. Armstrong, A. Caneiro, A. Manthiram, *Journal of the Electrochemical Society* **2001**, *148*, J7.

[39]   J. Matsuda, S. Kanae, T. Kawabata, J.T. Chou, Y. Inoue, S. Taniguchi, K. Sasaki, *ECS Transactions* **2017**, *78*, 993.

[40]   E. Boehm, J.-M. Bassat, P. Dordor, F. Mauvy, J.-C. Grenier, P. Stevens, *Solid State Ionics* **2005**, *176*, 2717.

[41]    A. Chroneos, D. Parfitt, J.A. Kilner, R.W. Grimes, *Journal of Materials Chemistry* **2010**, *20*, 266.

[42]    W. Sitte, R. Merkle, (eds.), *High-Temperature Electrolysis: From fundamentals to applications*, IOP Publishing, **2023**.

[43]    V. Vibhu, I.C. Vinke, R.A. Eichel, L.G.J. de Haart, *Journal of Power Sources* **2021**, *482*, 228909.

[44]    M. Rieu, R. Sayers, M. Laguna-Bercero, S. Skinner, P. Lenormand, F. Ansart, *Journal of the Electrochemical Society* **2010**, *157*, .

[45]    C. Ferchaud, J.-C. Grenier, Y. Zhang-Steenwinkel, M.M.A. van Tuel, F.P.F. van Berkel, J.-M. Bassat, *Journal of Power Sources* **2011**, *196*, 1872.

[46]    K. Chen, S.P. Jiang, *Electrochemical Energy Reviews* **2020**, *3*, 730.

[47]    I. Sreedhar, B. Agarwal, P. Goyal, A. Agarwal, *Journal of Solid State Electrochemistry* **2020**, *24*, 1239.

[48]    N.K. Patel, R.G. Utter, D. Das, M. Pecht, *Journal of Power Sources* **2019**, *438*, 227040.

[49]    W.A. Harrison, *Physical Review B* **2011**, *83*, 155437.

[50]    E. Ostrovskiy, Y.-L. Huang, E.D. Wachsman, *Journal of Materials Chemistry A* **2021**, *9*, 1593.

[51]    M. Niania, R. Podor, T.B. Britton, C. Li, S.J. Cooper, N. Svetkov, S. Skinner, J. Kilner, *Journal of Materials Chemistry A* **2018**, *6*, 14120.

[52]    Y. Yang, H. Bao, H. Ni, X. Ou, S. Wang, B. Lin, P. Feng, Y. Ling, *Journal of Power Sources* **2021**, *482*, 228959.

[53]    M.A.R. Niania, A.K. Rossall, J.A. Van den Berg, J.A. Kilner, *Journal of Materials Chemistry A* **2020**, *8*, 19414.

[54]    W. Lee, J.W. Han, Y. Chen, Z. Cai, B. Yildiz, *Journal of the American Chemical Society* **2013**, *135*, 7909.

[55]    X.-B. Xie, Q. Xu, D.-P. Huang, J. Xiao, M. Chen, K. Zhao, D.-C. Chen, F. Zhang, *Applied Surface Science* **2021**, *566*, 150659.

[56]    E. Bucher, M. Yang, W. Sitte, *Journal of the Electrochemical Society* **2012**, *159*, B592.

[57]    N. Schrödl, E. Bucher, A. Egger, P. Kreiml, C. Teichert, T. Höschen, W. Sitte, *Solid State Ionics* **2015**, *276*, 62.

[58]    M. Yang, E. Bucher, W. Sitte, *Journal of Power Sources* **2011**, *196*, 7313.

[59]    T. Horita, *Ceramics International* **2021**, *47*, 7293.

[60]    F. Wang, H. Kishimoto, T. Ishiyama, K. Develos-Bagarinao, K. Yamaji, T. Horita, H. Yokokawa, *Journal of Power Sources* **2020**, *478*, 228763.

[61]    E. Bucher, C. Gspan, F. Hofer, W. Sitte, *Solid State Ionics* **2013**, *238*, 15.

[62] H. Yokokawa, N. Sakai, T. Horita, K. Yamaji in: W. Vielstich (Ed.), Handbook of Fuel Cells, John Wiley & Sons, Ltd.,Hoboken, **2009**, p. 979.

[63] E. Bucher, C. Gspan, W. Sitte, *Solid State Ionics* **2015**, *272*, 112.

[64] M. François, M.P. Carpanese, O. Heintz, V. Lescure, D. Clematis, L. Combemale, F. Demoisson, G. Caboche, *Energies* **2021**, *14*, 3674.

[65] M. Hubert, J. Laurencin, P. Cloetens, J. Mougin, D. Ferreira Sanchez, S. Pylypko, M. Morales, A. Morata, B. Morel, D. Montinaro, E. Siebert, F. Lefebvre-Joud, *ECS Transactions* **2017**, *78*, 3167.

[66] J. Kim, H.-I. Ji, H. Dasari, D. Shin, H. Song, J. Lee, B.-K. Kim, H.-J. Je, H.-W. Lee, K. Yoon, *International Journal of Hydrogen Energy* **2013**, *38*, 1225.

[67] Z. Pan, Q. Liu, Z. Yan, Z. Jiao, L. Bi, S.H. Chan, Z. Zhong, *Electrochemistry Communications* **2022**, *137*, 107267.

[68] R. Knibbe, M.L. Traulsen, A. Hauch, S.D. Ebbesen, M. Mogensen, *Journal of the Electrochemical Society* **2010**, *157*, B1209.

[69] M.S. Khan, X. Xu, R. Knibbe, Z. Zhu, *Renewable and Sustainable Energy Reviews* **2021**, *143*, 110918.

[70] A.V. Virkar, *International Journal of Hydrogen Energy* **2010**, *35*, 9527.

[71] S.J. Skinner, J.A. Kilner, *Materials Today* **2003**, *6*, 30.

[72] S.P.S. Badwal, *Solid State Ionics* **1992**, *52*, 23.

[73] W. Araki, D. Hanashiro, Y. Arai, J. Malzbender, *Acta Materialia* **2013**, *61*, 3082.

[74] M. Weller, F. Khelfaoui, M. Kilo, M.A. Taylor, C. Argirusis, G. Borchardt, *Solid State Ionics* **2004**, *175*, 329.

[75] R.N. Basu in: S. Basu (Ed.), Recent Trends in Fuel Cell Science and Technology, Springer New York, **2007**, p. 286.

[76] J. Szász, F. Wankmüller, V. Wilde, H. Störmer, D. Gerthsen, N.H. Menzler, E. Ivers-Tiffée, *Journal of the Electrochemical Society* **2018**, *165*, F898.

[77] J. Zhang, C. Lenser, N.H. Menzler, O. Guillon, *Solid State Ionics* **2020**, *344*, 115138.

[78] A. Tsoga, A. Gupta, A. Naoumidis, P. Nikolopoulos, *Acta Materialia* **2000**, *48*, 4709.

[79] R. Punn, A.M. Feteira, D.C. Sinclair, C. Greaves, *Journal of the American Chemical Society* **2006**, *128*, 15386.

[80] A.A. Yaremchenko, V.V. Kharton, E.N. Naumovich, A.A. Tonoyan, *Materials Research Bulletin* **2000**, *35*, 515.

[81] S. Dwivedi, *International Journal of Hydrogen Energy* **2020**, *45*, 23988.

[82] J.B. Hansen, *Faraday Discussions* **2015**, *182*, 9.

[83] A. Baldan, *Journal of Materials Science* **2002**, *37*, 2379.

[84]    D. Simwonis, F. Tietz, D. Stöver, *Solid State Ionics* **2000**, *132*, 241.

[85]    M.B. Mogensen, M. Chen, H.L. Frandsen, C. Graves, A. Hauch, P.V. Hendriksen, T. Jacobsen, S.H. Jensen, T.L. Skafte, X. Sun, *Fuel Cells* **2021**, *21*, 415.

[86]    P. Vernoux, *Ionics* **1997**, *3*, 270.

[87]    R. Costa, F. Han, P. Szabo, V. Yurkiv, R. Semerad, S.K. Cheah, L. Dessemond, *Fuel Cells* **2018**, *18*, 251.

[88]    S.P.S. Shaikh, A. Muchtar, M.R. Somalu, *Renewable and Sustainable Energy Reviews* **2015**, *51*, 1.

[89]    C.M. Rost, E. Sachet, T. Borman, A. Moballegh, E.C. Dickey, D. Hou, J.L. Jones, S. Curtarolo, J.-P. Maria, *Nature Communications* **2015**, *6*, 8485.

[90]    A. Sarkar, Q. Wang, A. Schiele, M.R. Chellali, S.S. Bhattacharya, D. Wang, T. Brezesinski, H. Hahn, L. Velasco, B. Breitung, *Advanced Materials* **2019**, *31*, 1806236.

[91]    B.S. Murty, J.W. Yeh, S. Ranganathan, *High-Entropy Alloys*, Elsevier Science, **2014**.

[92]    R. Shannon, *Acta Crystallographica Section A* **1976**, *32*, 751.

[93]    W.-L. Hsu, C.-W. Tsai, A.-C. Yeh, J.-W. Yeh, *Nature Reviews Chemistry* **2024**, *8*, 471.

[94]    H. Nan, S. Lv, Z. Xu, Y. Feng, Y. Zhou, M. Liu, T. Wang, X. Liu, X. Hu, H. Tian, *Chemical Engineering Journal* **2023**, *452*, 139501.

[95]    S. Ranganathan, *Current Science* **2003**, *85*, 1404.

[96]    J.-W. Yeh, *JOM* **2015**, *67*, 2254.

[97]    V.M.T. Goldschmidt, L.; Ulrich, F.; Barth, T. F. W.; Lunde, G. O. J.; Holmsen, D.; Zachariasen, W. H., *Kristiania* **1923**, 116.

[98]    F.S. Galasso in: R. Smoluchowski (Ed.), Structure, Properties and Preparation of Perovskite Type Compounds, International Series of Monographs in Solid State Physics, **1969**, p. 3.

[99]    S.C. Tidrow, *Ferroelectrics* **2014**, *470*, 13.

[100]   Y. Zhang, T.T. Zuo, Z. Tang, M.C. Gao, K.A. Dahmen, P.K. Liaw, Z.P. Lu, *Progress in Materials Science* **2014**, *61*, 1.

[101]   J.-W. Yeh, S.-J. Lin, T.-S. Chin, J.-Y. Gan, S.-K. Chen, T.-T. Shun, C.-H. Tsau, S.-Y. Chou, *Metallurgical and Materials Transactions A* **2004**, *35*, 2533.

[102]   A. Sarkar, L. Velasco, D. Wang, Q. Wang, G. Talasila, L. de Biasi, C. Kübel, T. Brezesinski, S.S. Bhattacharya, H. Hahn, B. Breitung, *Nature Communications* **2018**, *9*, 3400.

[103]   T. Tsai, S.A. Barnett, *Solid State Ionics* **1997**, *93*, 207.

[104]   A.K. Opitz, C. Rameshan, M. Kubicek, G.M. Rupp, A. Nenning, T. Götsch, R. Blume, M. Hävecker, A. Knop-Gericke, G. Rupprechter, B. Klötzer, J. Fleig, *Topics in Catalysis* **2018**, *61*, 2129.

[105] Q. Yang, G. Wang, H. Wu, B.A. Beshiwork, D. Tian, S. Zhu, Y. Yang, X. Lu, Y. Ding, Y. Ling, Y. Chen, B. Lin, *Journal of Alloys and Compounds* **2021**, *872*, 159633.

[106] J. Dąbrowa, A. Olszewska, A. Falkenstein, C. Schwab, M. Szymczak, M. Zajusz, M. Moździerz, A. Mikuła, K. Zielińska, K. Berent, T. Czeppe, M. Martin, K. Świerczek, *Journal of Materials Chemistry A* **2020**, *8*, 24455.

[107] L. Shen, Z. Du, Y. Zhang, X. Dong, H. Zhao, *Applied Catalysis B: Environmental* **2021**, *295*, 120264.

[108] W. Preis, E. Bucher, W. Sitte, *Journal of Power Sources* **2002**, *106*, 116.

[109] E. Bucher, C. Gspan, T. Hoeschen, F. Hofer, W. Sitte, *Solid State Ionics* **2017**, *299*, 26.

[110] A. Robles-Fernández, *Ph.D. Thesis*, Universidad de Zaragoza, **2022**.

[111] A. Nechache, M. Cassir, A. Ringuedé, *Journal of Power Sources* **2014**, *258*, 164.

[112] S.M. Gateman, O. Gharbi, H. Gomes de Melo, K. Ngo, M. Turmine, V. Vivier, *Current Opinion in Electrochemistry* **2022**, *36*, 101133.

[113] S. Primdahl, M. Mogensen, *Journal of the Electrochemical Society* **1999**, *146*, 2827.

[114] R. Barfod, M. Mogensen, T. Klemensø, A. Hagen, Y.-L. Liu, P. Vang Hendriksen, *Journal of the Electrochemical Society* **2007**, *154*, B371.

[115] T. Jacobsen, P.V. Hendriksen, S. Koch, *Electrochimica Acta* **2008**, *53*, 7500.

[116] V. Subotić, C. Schluckner, J. Strasser, V. Lawlor, J. Mathe, J. Rechberger, H. Schroettner, C. Hochenauer, *Electrochimica Acta* **2016**, *207*, 224.

[117] Z. Liu, S. Xu, T. Li, B. Xie, K. Guo, J. Lu, *Ceramics International* **2021**, *47*, 33039.

[118] J. Park, B. Xu, J. Pan, D. Zhang, S. Lany, X. Liu, J. Luo, Y. Qi, *npj Computational Materials* **2023**, *9*, 29.

[119] R. Jacobs, T. Mayeshiba, J. Booske, D. Morgan, *Advanced Energy Materials* **2018**, *8*, 1702708.

[120] A. Chroneos, R.V. Vovk, I.L. Goulatis, L.I. Goulatis, *Journal of Alloys and Compounds* **2010**, *494*, 190.

[121] A. Badruzzaman, A. Yuda, A. Ashok, A. Kumar, *Inorganica Chimica Acta* **2020**, *511*, 119854.

[122] X. Liu, H. Gong, T. Wang, H. Guo, L. Song, W. Xia, B. Gao, Z. Jiang, L. Feng, J. He, *Chemistry – An Asian Journal* **2018**, *13*, 528.

[123] G. DiGiuseppe, L. Sun, *Fuel and Energy Abstracts* **2011**, *36*, 5076.

[124] F. Tietz, V.A.C. Haanappel, A. Mai, J. Mertens, D. Stöver, *Journal of Power Sources* **2006**, *156*, 20.

[125] W. Li, Y. Shi, Y. Luo, N. Cai, *International Journal of Hydrogen Energy* **2014**, *39*, 13738.

[126] S. Kim, D.W. Joh, D.-Y. Lee, J. Lee, H.S. Kim, M.Z. Khan, J.E. Hong, S.-B. Lee, S.J. Park, R.-H. Song, M.T. Mehran, C.K. Rhee, T.-H. Lim, *Chemical Engineering Journal* **2021**, *410*, 128318.

[127] V. Subotić, T. Thaller, B. Königshofer, N.H. Menzler, E. Bucher, A. Egger, C. Hochenauer, *International Journal of Hydrogen Energy* **2020**, *45*, 29166.

[128] J. Zhang, L. Lei, H. Li, K. Sun, Z. Sun, M. Han, *Journal of Power Sources* **2021**, *516*, 230678.

[129] Y. Fu, Y. Jiang, S. Poizeau, A. Dutta, A. Mohanram, J.D. Pietras, M.Z. Bazant, *Journal of the Electrochemical Society* **2015**, *162*, F613.

[130] A. Rolle, V. Thoréton, P. Rozier, E. Capoen, O. Mentré, B. Boukamp, S. Daviero-Minaud, *Fuel Cells* **2012**, *12*, 288.

[131] P. Moçoteguy, A. Brisse, *International Journal of Hydrogen Energy* **2013**, *38*, 15887.

[132] P. Pretschuh, A. Egger, R. Brunner, E. Bucher, *Fuel Cells* **2023**, *23*, 377.

[133] P. Pretschuh, A. Egger, P. Paulachan, J. Schöggl, R. Brunner, E. Bucher, *Fuel Cells* **2024**, https://doi.org/10.1002/fuce.202400068.

[134] W. Guan, G. Wang, X.-D. Zhou, *Journal of Power Sources* **2017**, *351*, 169.

[135] P. Pretschuh, A. Egger, E. Bucher, *Solid State Ionics* **2024**, submitted.

[136] R.E. van Doorn, I.C. Fullarton, R.A. de Souza, J.A. Kilner, H.J.M. Bouwmeester, A.J. Burggraaf, *Solid State Ionics* **1997**, *96*, 1.

[137] W. Sitte, E. Bucher, W. Preis, *Solid State Ionics* **2002**, *154-155*, 517.

[138] L.W. Tai, M.M. Nasrallah, H.U. Anderson, D.M. Sparlin, S.R. Sehlin, *Solid State Ionics* **1995**, *76*, 259.

# 7 Appendix

## 7.1 Declaration of usage of artificial intelligence

| Topic | usage in% | Tool/ Version | Notes | Prompts |
|---|---|---|---|---|
| Improvement of spellings | 5 | DeepL Write (Beta), ChatGPT (V3.5) | Translation, improving linguistic readability. Percentage refers to portion of text derived from AI tools within the thesis. | Available at internal server of the Chair of Physical Chemistry |

## 7.2 Contribution of the Authors

Paper 1

Title: Electrochemical and microstructural characterization of the high entropy perovskite $La_{0.2}Pr_{0.2}Nd_{0.2}Sm_{0.2}Sr_{0.2}CoO_{3-\delta}$ for solid oxide cell air electrodes

Authors: Patrick Pretschuh, Andreas Egger, Roland Brunner, Edith Bucher

Journal: Fuel Cells

Year of publication: 2023

DOI: 10.1002/fuce.202300036

Contribution of the Authors:

<u>Patrick Pretschuh:</u> Conceptualization, Methodology, Validation, Formal analysis, Investigation, Writing - Original Draft, Visualization

<u>Andreas Egger:</u> Conceptualization, Methodology, Validation, Writing - Review & Editing

<u>Roland Brunner:</u> Resources, Writing - Review & Editing, Funding acquisition

<u>Edith Bucher:</u> Conceptualization, Resources, Writing - Review & Editing, Supervision, Funding acquisition

Title: Cobalt-free high entropy perovskite $La_{0.2}Pr_{0.2}Nd_{0.2}Sm_{0.2}Sr_{0.2}FeO_{3-\delta}$ solid oxide cell air electrode with enhanced performance

Authors: Patrick Pretschuh, Andreas Egger, Priya Paulachan, Johanna Schöggl, Roland Brunner, Edith Bucher

Journal: Fuel Cells

Year of publication: 2024

DOI: 10.1002/fuce.202400068

Contribution of the Authors:

<u>Patrick Pretschuh:</u> Conceptualization, Methodology, Validation, Formal analysis, Investigation, Writing - Original Draft, Visualization

<u>Andreas Egger:</u> Conceptualization, Validation, Writing - Review & Editing

<u>Priya Paulachan:</u> Formal Analysis, Writing - Review & Editing

<u>Johanna Schöggl:</u> Formal Analysis, Writing - Review & Editing

<u>Roland Brunner:</u> Resources, Writing - Review & Editing, Funding acquisition

<u>Edith Bucher:</u> Conceptualization, Resources, Writing - Review & Editing, Supervision, Funding acquisition

Title: Crystal structure, electronic conductivity and oxygen exchange kinetics of high-entropy perovskites $La_{0.2}Pr_{0.2}Nd_{0.2}Sm_{0.2}Sr_{0.2}Co_{1-x}Fe_xO_{3-\delta}$ (x = 0, 0.5, 1) high entropy perovskites

Authors: Patrick Pretschuh, Andreas Egger, Edith Bucher

Journal: Solid State Ionics

Date of submission: 22.06.2024

Contribution of the Authors:

Patrick Pretschuh: Conceptualization, Validation, Formal analysis, Investigation, Writing - Original Draft, Visualization

Andreas Egger: Conceptualization, Methodology, Validation, Writing - Review & Editing

Edith Bucher: Conceptualization, Methodology, Resources, Writing - Review & Editing, Supervision, Funding acquisition

## 7.3  Full text of the publications

Fuel Cells
FROM FUNDAMENTALS TO SYSTEMS

RESEARCH ARTICLE

# Electrochemical and microstructural characterization of the high-entropy perovskite $La_{0.2}Pr_{0.2}Nd_{0.2}Sm_{0.2}Sr_{0.2}CoO_{3-\delta}$ for solid oxide cell air electrodes

Patrick Pretschuh[1] [ID] | Andreas Egger[1] [ID] | Roland Brunner[2] | Edith Bucher[1] [ID]

[1]Department General, Analytical and Physical Chemistry, Montanuniversitaet Leoben, Chair of Physical Chemistry, Leoben, Austria

[2]Department Microelectronics, Materials Center Leoben Forschung GmbH, Leoben, Austria

**Correspondence**
Edith Bucher, Montanuniversitaet Leoben, Chair of Physical Chemistry, Franz-Josef-Straße 18, AT-8700 Leoben, Austria.
Email: edith.bucher@unileoben.ac.at

Paper presented at the 15th European SOFC & SOE Forum 2022, held 5-8 July in 2022 in Lucerne, Switzerland. Organized by the European Fuel Cell Forum www.efcf.com

**Funding information**
Zukunftsfonds Steiermark, Grant/Award Number: 1704

## Abstract

Strontium segregation (coupled to phase decomposition and impurity poisoning) and electrode delamination are two of the most important degradation mechanisms currently limiting the long-term stability of solid oxide fuel cell and electrolysis cell (SOFC and SOEC) air electrodes. The present study aims to demonstrate that air electrodes made of entropy-stabilized multi-component oxides can mitigate these degradation mechanisms while providing excellent cell performance. A SOEC utilizing $La_{0.2}Pr_{0.2}Nd_{0.2}Sm_{0.2}Sr_{0.2}CoO_{3-\delta}$ (LPNSSC) as an air electrode delivers $-1.56$ A/cm$^2$ at 1.2 V at 800°C. This performance exceeds that of a commercial cell with $La_{0.6}Sr_{0.4}CoO_{3-\delta}$ (LSC) air electrode, which reaches $-1.43$ A/cm$^2$. In a long-term electrolysis test, the LPNSSC cell shows stable performance during 700 h, while the LSC cell degrades continuously. Post-mortem analyses by scanning electron microscopy-energy dispersive X-ray spectroscopy indicate complete delamination of the LSC electrode, while LPNSSC shows excellent adhesion. The amount of secondary phases formed (esp. SrSO$_4$) is also much lower in LPNSSC compared to LSC. In conclusion, the high-entropy perovskite LPNSSC is a promising option for air electrodes of solid oxide cells. While LPNSSC can compete with – or even outperform – LSC air electrodes in terms of electrochemical performance, it could be particularly advantageous in terms of long-term stability in SOEC mode.

**KEYWORDS**
electrochemical characterization, fuel cell electrode, high-entropy perovskite, microstructural characterization, solid oxide electrolysis cell, solid oxide fuel cell, strontium segregation

## 1 | INTRODUCTION

Nowadays, hydrogen is acknowledged as a fundamental component of a sustainable green industry [1–3] and potential fields of application include many energy-intensive industrial divisions [4–6]. In addition to efficient storage and transport, one of the biggest hurdles is the sustainable production of green hydrogen. In this context, high-temperature water electrolysis with solid oxide cells (SOCs) is a promising technology for large-scale applications [7, 8]. Moreover, solid oxide fuel cells (SOFCs), solid oxide electrolysis cells (SOECs), or reversible SOCs

(RSOCs) can also be applied as power balancing or independent power supply systems [9]. Such industrial-scale plants can play an important role in buffering fluctuating and seasonal wind and solar energy [10]. Especially in combination with applications that also require or supply thermal energy, SOCs can develop their full potential [11]. Although application areas are growing, there are still some challenges for SOCs to achieve broad market penetration. These issues concern in particular the costs of materials and systems, which go hand in hand with the efficiency and lifetime of SOC solutions. The air electrode is a key component of SOCs [12], which requires materials with excellent electrochemical performance and good long-term stability [13–16]. Especially in the electrolysis mode, delamination of the air electrode is a critical degradation mechanism caused by high internal oxygen pressure in the electrolyte close to the air electrode interface [17]. In addition, Sr segregation is one of the main reasons for air electrode degradation in state-of-the-art (SOTA) perovskites like $La_{0.6}Sr_{0.4}Co_{0.2}Fe_{0.8}O_{3-\delta}$ (LSCF) [18–21] and $La_{0.6}Sr_{0.4}CoO_{3-\delta}$ (LSC) [22–26]. High-entropy (multi-component) oxides are a relatively new strategy to stabilize ceramic compounds through their increased configurational entropy [27]. This approach is also suitable to improve the thermodynamic stability of perovskites (general formula $ABO_3$) by mixing n $\geq$ 5 cations on the A- and/or B-sites of the crystal lattice [27–30]. Compared to low-entropy perovskites (LEP) such as LSCF, Sr segregation is suppressed in medium- (MEP) and high-entropy perovskites (HEP) [31, 32]. Good electrochemical performances and low polarization resistances are reported for SOCs with HEP and MEP air electrodes [31–34]. However, there is a need for further experimental verification and deeper insights into the structure-property relationships in order to prove enhanced long-term stability of electrochemical SOCs with HEP electrodes. In the present study, the HEP $La_{0.2}Pr_{0.2}Nd_{0.2}Sm_{0.2}Sr_{0.2}CoO_{3-\delta}$ (LPNSSC) is characterized as a SOC air electrode in terms of electrochemical performance, long-term stability, microstructure, and cation distribution. The composition LPNSSC was selected in analogy to the well-investigated low-entropy perovskites from the series $(La,Sr)CoO_{3-\delta}$, which show high electronic and significant ionic conductivities and fast oxygen exchange kinetics [35, 36], but limited long-term stability [37, 38]. For the A-site, Pr, Nd, and Sm were chosen in addition to La and Sr since these rare earth elements have similar ionic radii as La and Sr [39]. In order to maximize the configurational entropy (Equation S1), the five cations were used in equimolar amounts of 0.2 each. In particular, this work aims at demonstrating that the power densities and long-term stabilities of cells with HEP electrodes can exceed those of cells with SOTA perovskites, especially in SOEC mode, and that Sr segregation

and delamination of the air electrode are lower for HEPs compared to SOTA electrode materials.

## 2 | EXPERIMENTAL SECTION

### 2.1 | Synthesis of LPNSSC

LPNSSC powder is synthesized by the citric acid–ethylenediaminetetraacetate (CA-EDTA) sol-gel method. Stoichiometric amounts of metal nitrates, that is, $La(NO_3)_3\cdot6H_2O$, $Pr(NO_3)_3\cdot6H_2O$, $Nd(NO_3)_3\cdot6H_2O$, $Sm(NO_3)_3\cdot6H_2O$, $Sr(NO_3)_2$ and $Co(NO_3)_2\cdot6H_2O$ (all chemicals purchased from Aldrich, purity $\geq$99.0%), are dissolved in deionized water, stirred, heated and mixed with 1 mol anhydrous citric acid per mol of cations. A pH of 8 is adjusted by the addition of an aqueous ammonia solution. The temperature of the solution is then raised on a hot plate to evaporate water and form a gel. After the water is completely evaporated, spontaneous combustion occurs, and the temperature is maintained until the gel is completely converted to raw ash. The powder is homogenized with an agate mortar and then calcined for 4 h at 1000°C in the air with heating and cooling rates of 5 K/min[1].

### 2.2 | Preparation of cells

The calcined LPNSSC powder is milled for 48 h on a rolling bench using 3 mm diameter zirconia balls in ethanol until a particle size distribution with $d_{50}$ of approximately 0.5 µm is reached. A terpineol-based ink vehicle containing 6 wt.% ethyl cellulose is used to produce a screen-printing paste containing 66 wt.% LPNSSC. The paste is screen-printed onto commercially available 2 cm diameter round anode-supported cell (ASC) substrates (fuelcellmaterials) and 5×5 cm² square ASC substrates (Elcogen AS). The active area of the cells is 1.1 cm² (button cells) and 16 cm² (square cells). The cells with the printed electrodes are sintered for 2 h at 1070°C with heating rates of 5 K/min and cooling rates of 2 K/min. A commercial 5×5 cm² ASC consisting of an LSC air electrode, GDC diffusion barrier, YSZ electrolyte, and Ni-YSZ fuel electrode (Elcogen AS) was used as a benchmark for comparison with the 5×5 cm² LPNSSC cell.

### 2.3 | Microstructural characterization

The microstructure of the cells is investigated by field emission scanning electron microscopy (FESEM) using a ZEISS 450 GeminiSEM in backscattered electron (BSE)

and secondary electron (SE) mode with 5 kV and 3 nA. For the preparation of specimen cross sections, the cells are sectioned with a diamond wire saw and then cut with a Hitachi IM400Plus ion slicer. A thin layer of gold is sputtered onto the samples to ensure good electrical conductivity. The distribution of chemical elements is mapped by energy dispersive X-ray spectroscopy (EDX) using an Ultim Extreme detector from Oxford Instruments at an energy range of 10 keV.

## 2.4 | Electrochemical characterization

Button cells with a diameter of 2 cm are investigated using a Probostat system (NorECs Norwegian Electro Ceramics AS) and a frequency response analyzer (Novocontrol Alpha-A) with potentiostat/galvanostat interface (Novocontrol POT/GAL 15 V/10 A). Electrochemical impedance spectroscopy (EIS) is performed in a four-wire configuration in the frequency range of 10 mHz – 1 MHz. The cells are placed in an alumina sample holder inside a tubular furnace. Gold sealant ensures gas tightness between the air side and the fuel side. Ni-mesh/Ni-paste and Pt-mesh/Pt-paste are used for current collection on the fuel electrode and air electrode, respectively.

Square $5{\times}5$ cm$^2$ cells are electrochemically characterized with an Evaluator C50-HT (Horiba FuelCon GmbH) system. The cells are placed between an alumina plate and a polished ceramic cell housing to ensure gas tightness. Ni- and Pt-meshes (without metallic contact pastes) are used as current collectors on the fuel and air electrode sides, respectively. A mechanical load of 1 kg is used to improve the gas tightness and reduce contact resistance.

For both button cells and square cells, the current density-voltage characteristics are recorded at current ramps of up to 3 mA/(cm$^2$ s) until the voltage reaches at least 1.2 V (SOEC) or drops to 0.7 V (SOFC). For button cells, the cell performance under continuous load is evaluated at a gas flow of 40 ml/min at the fuel electrode and 100 ml/min at the air electrode. For SOEC operation, the fuel stream is humidified with a Humistat setup (NorECs Norwegian Electro Ceramics AS). For the $5{\times}5$ cm$^2$ planar cells, the fuel and air flow rates are 1 l/min unless otherwise specified. Heating and cooling rates are 2 K/min for button cells and 1 K/min for $5{\times}5$ cm$^2$ ASCs.

## 3 | RESULTS AND DISCUSSION

### 3.1 | Electrochemical characterization

The performance of LPNSSC | GDC | YSZ | Ni-YSZ button cells is evaluated in SOFC mode in the temperature
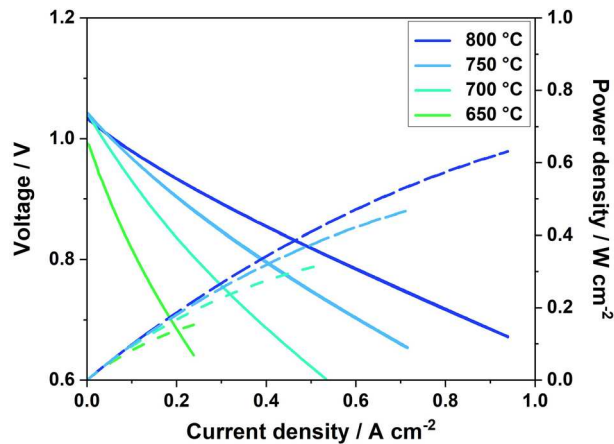


**FIGURE 1** Current-voltage curves (solid lines) and power densities (dashed lines) of a button cell with La$_{0.2}$Pr$_{0.2}$Nd$_{0.2}$Sm$_{0.2}$Sr$_{0.2}$CoO$_{3-\delta}$ (LPNSSC) air electrode in solid oxide fuel cell (SOFC) mode at different temperatures. Gas flows were 100 ml/min with 20% O$_2$ (rest Ar) at the air electrode and 40 ml/min H$_2$ with 3% H$_2$O at the fuel electrode.

range from 650°C to 800°C. Figure 1 shows the cell voltage and power density versus the current density. The power densities at 0.7 V are 0.59, 0.42, 0.26, and 0.13 W/cm$^2$ at 800, 750, 700, and 650°C, respectively. According to the Nernst equation, the theoretical equilibrium potential for a 97% H$_2$ / 3% H$_2$O fuel mixture vs. 20% O$_2$ at 800°C is 1.10 V. However, the measured open circuit voltage (OCV) at 800°C shows only 1.04 V and also remains below the theoretical value at 650°C. This indicates a minor gas leak due to imperfect sealing, but it is not expected to have a significant impact on the characterization.

Impedance spectra of the button cell are recorded at OCV as shown in Figure 2. The overall polarization resistance $R_p$ and the serial resistance $R_s$ are determined by fitting the curves to an equivalent circuit in the configuration $(L_0+R_s) + R_1||CPE_1 + R_2||CPE_2 + R_3||CPE_3$. Here $L_0$ is the inductance of the setup, $R_s$ corresponds to the ohmic part of the impedance, and the resistances $R_1$, $R_2$, and $R_3$ add up to $R_p$. Constant phase elements (CPEs) are used to model the capacitive components of the polarization processes. The CPE values are then converted to equivalent capacitances ($C_i$) using the procedure described by Fleig [40]. The inductance of the setup $L_0$ and the serial resistance $R_s$ are subtracted from the data sets shown in Figure 2 for better comparability. Values of $R_s$ and $R_p$ are listed in Table 1 as a function of temperature. A comprehensive overview of the inductive, resistive, and capacitive contributions obtained from impedance analysis is given in Table S1.

The long-term performance and degradation behavior of LPNSSC are investigated in SOEC mode using $5{\times}5$ cm$^2$ planar cells. Initial electrochemical characterization

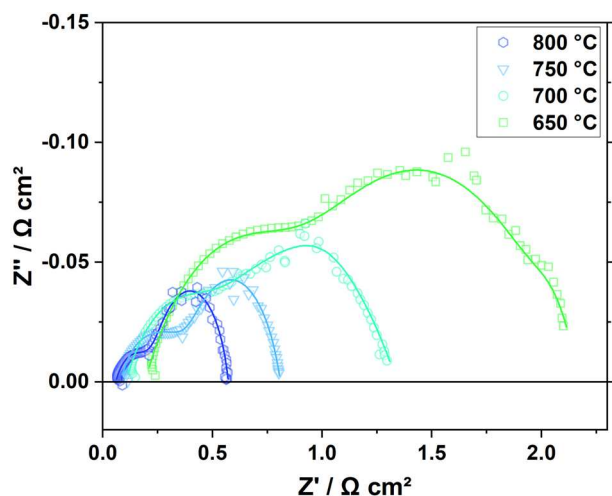**FIGURE 2**　Impedance spectra (100 mV below OCV) of the button cell with $La_{0.2}Pr_{0.2}Nd_{0.2}Sm_{0.2}Sr_{0.2}CoO_{3-\delta}$ (LPNSSC) air electrode at different temperatures. Gas flows were 100 ml/min with 20% $O_2$ (rest Ar) at the air electrode and 40 ml/min $H_2$ with 3% $H_2O$ at the fuel electrode. Lines are fits with the equivalent circuit described in the text. For better comparability the inductance of the setup and the serial resistance were subtracted from the data sets.

**TABLE 1**　Serial resistances ($R_s$) and total polarization resistances ($R_p$) of the button cell with $La_{0.2}Pr_{0.2}Nd_{0.2}Sm_{0.2}Sr_{0.2}CoO_{3-\delta}$ (LPNSSC) air electrode as obtained from impedance spectra shown in Figure 2.

| $T$ /°C | 800 | 750 | 700 | 650 |
|---|---|---|---|---|
| $R_s$ / Ω cm² | 0.051 | 0.066 | 0.090 | 0.143 |
| $R_p$ / Ω cm² | 0.438 | 0.626 | 1.04 | 1.98 |

is performed with 90%, 70%, and 50% $H_2O$ (rest $H_2$). Current densities reach −1.24, −0.92, and −0.74 A/cm², respectively, at 1.2 V and 800°C as shown in Figure 3. In addition to the 5×5 cm² LPNSSC cell, the electrochemical performance of a 2 cm button cell is investigated in order to evaluate the influence of the different cell sizes and test setups. For the button cell, the SOEC current density at 1.2 V with 70% $H_2O$ is −1.6 A/cm² (Figure S1), which is significantly higher than the −0.92 A/cm² reached by the 5×5 cm² cell (Figure 3). As the layer structure of both cells is very similar, this difference suggests differences in test setups and gas supplies as underlying causes. For example, reducing the $H_2O$/$H_2$ inlet flow from standard 1 l/min to a lower flow of 0.25 l/min has a significant impact on the electrochemical performance of the 5×5 cm² LPNSSC and LSC cells (Figure S4). Taking into account the influencing factors evident in Figure S1, Figure 3, and Figure S4, it is important to note that cell performances should be compared only with identical cell geometries and under identical test conditions, as done in Figure 4.
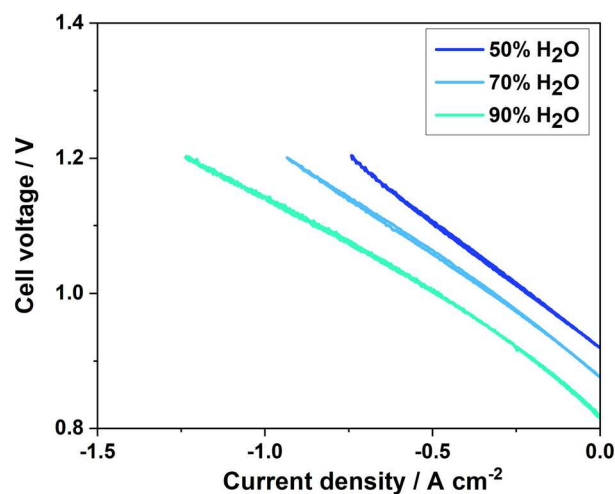


**FIGURE 3**　Current density-voltage curves of a 5×5 cm² cell with $La_{0.2}Pr_{0.2}Nd_{0.2}Sm_{0.2}Sr_{0.2}CoO_{3-\delta}$ (LPNSSC) air electrode at different levels of fuel humidification at 800°C; gas flows are 1 l/min air at the air electrode and 1 l/min $H_2$/$H_2O$ at the fuel electrode.
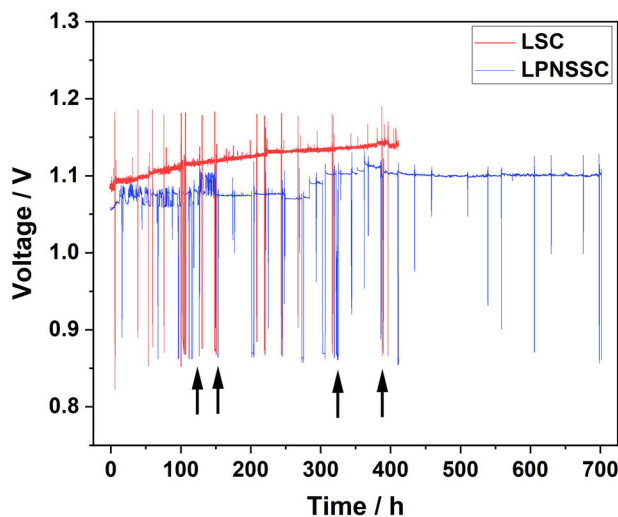


**FIGURE 4**　Voltage curves of 5×5 cm² ASCs with $La_{0.2}Pr_{0.2}Nd_{0.2}Sm_{0.2}Sr_{0.2}CoO_{3-\delta}$ (LPNSSC) (blue) and $La_{0.6}Sr_{0.4}CoO_{3-\delta}$ (LSC) (red) air electrodes during long-term polarization in solid oxide electrolysis cell (SOEC) mode with −0.938 A/cm² at 800°C. Arrows mark points in time when uncontrolled shutdowns during the LPNSSC test occurred. Test parameters are 80% $H_2O$ (rest $H_2$) at the fuel electrode and compressed air at the air electrode, both with 1 l/min gas flow.

Regarding long-term steam electrolysis tests, we compare a commercial anode-supported cell (ASC) with an LSC air electrode (Elcogen AS) with the ASC utilizing the HEP LPNSSC air electrode. Test conditions are the same for both cells and chosen in analogy to published research [41]. Constant current densities of −0.938 A/cm² are applied at 800°C during the entire test, while the change of cell voltage is observed, as shown in Figure 4.
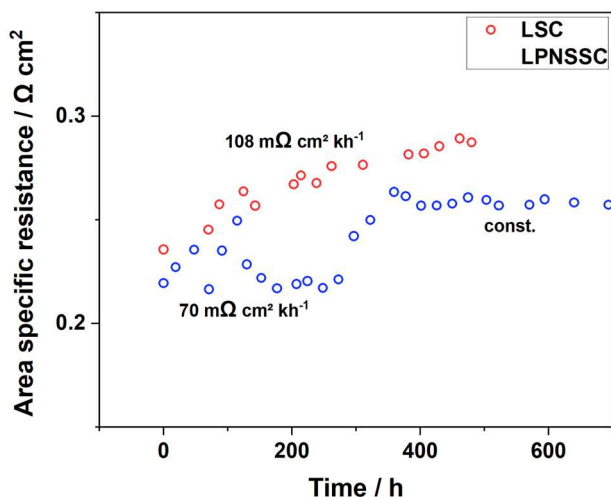
**FIGURE 5** ASR of 5×5 cm$^2$ anode-supported cells (ASCs) with La$_{0.2}$Pr$_{0.2}$Nd$_{0.2}$Sm$_{0.2}$Sr$_{0.2}$CoO$_{3-\delta}$ (LPNSSC) and La$_{0.6}$Sr$_{0.4}$CoO$_{3-\delta}$ (LSC) air electrodes during long-term solid oxide electrolysis cell (SOEC) studies. Test parameters were 80% humidity (rest H$_2$) at the fuel electrode and air at the air electrode with 1 l/min gas flow each. A continuous polarization at −0.938 A/cm$^2$ was applied.

Area-specific resistances (ASRs) are calculated from the average slopes of the current-voltage curves, which are acquired in regular intervals during the long-term measurements (see examples in Figures S2 and S3 for LPNSSC and LSC, respectively). Figure 5 shows the time dependence of the ASR values of the cells with LSC and LPNSSC electrodes. The SOTA cell with an LSC air electrode shows a continuous increase in the cell voltage during SOEC operation for 500 h. The average ASR degradation rate is 108 mΩ cm$^2$ per 1000 h (estimated by linear interpolation between the measured ASR values at 0 and 450 h), which is similar to degradation rates reported by other groups [42, 43]. In the course of the long-term SOEC test of the cell with LPNSSC air electrode, four thermal cycles were performed due to unintended shutdowns of the test setup (Figure 4). During these shutdowns, heating was turned off and the cell was cooled down to room temperature with undefined cooling rates. Afterwards, the cell was re-heated to 800°C with heating rate of 1 K/min (arrows in Figure 4, cooling/heating ramps not shown). Several step-wise changes of the cell voltage occur (in particular after thermal cycles and recordings of current-voltage curves), which are a consequence of the thermal cycles rather than due to continuous performance degradation. In the first 400 h of testing, where all four thermal cycles occurred, the average increase of the ASR is 70 mΩ cm$^2$ per 1000 h (estimated by linear interpolation between the measured ASR values at 0 and 400 h) (Figure 5). After stability issues with the test setup were resolved and continuous SOEC operation prevails, no more abrupt changes in cell volt-

age are observed and the voltage of the LPNSSC cell shows virtually no increase in the time interval of 400–700 h (Figure 4). This indicates excellent performance stability of the LPNSSC cell compared to the LSC cell at similar voltage levels.

## 3.2 | Microstructural characterization of fresh and degraded cells

A FESEM-BSE image of the cross-section of a fresh 5×5 cm$^2$ ASC with LPNSSC air electrode is shown in Figure 6. It should be noted that the fuel electrode of the freshly prepared cell is not reduced and is therefore composed of NiO-YSZ (not Ni-YSZ). The air electrode shows a homogeneous thickness of 14 μm (± 0.3 μm) and uniform microstructure across the entire analyzed region (Figures S5 and S7). Thresholding-based image analysis of the air electrode yields a porosity of 24%. Image analysis was performed using the software ImageJ [44]. Figure 6 depicts the interfaces between the air electrode, the diffusion barrier (GDC), the electrolyte (YSZ), and the functional layer of the fuel electrode (NiO-YSZ). The layers in contact adhere well to each other. The electrolyte is dense and no cracks or open porosity are observed, whereas the GDC barrier is relatively porous (porosity estimated to be 9%). Figure 6 also shows EDX elemental maps of the same region. The Sr- and Zr-maps indicate the formation of small SrZrO$_3$ grains at the interface between GDC barrier and YSZ electrolyte, which presumably occurs during the sintering process. As reported in the literature, the porosity of the GDC barrier facilitates the formation of SrZrO$_3$ via cation interdiffusion [45]. SEM-EDX analyses of a fresh 5×5 cm$^2$ ASC with LSC air electrode are shown in Figure 7 (see also further images in Figures S6 and S8). The thickness of the LSC air electrode is 16 μm (± 0.5 μm) with a porosity of 36%. Again, the electrolyte layer is dense, whereas the GDC barrier is relatively porous (porosity estimated to be 13%) and EDX images show formation of SrZrO$_3$ at the GDC/YSZ interface of the LSC cell.

It should be noted that the apparent Co-signals in the fuel electrode (Figure 6d), apparent La/Sr-signals in regions other than the air electrode and the electrode/electrolyte interface (Figures 6b,c, and 7b,c), as well as apparent Y-signals in the air electrode (Figures 6f and 7f) are artifacts due to overlapping or small-intensity peaks in the EDX spectra. These artifacts are more pronounced for the LPNSSC cell due to the larger variety and lower contents of rare earth elements as compared to the LSC cell.

Post-mortem microstructural analyses of 5×5 cm$^2$ LPNSSC and LSC cells are performed after the SOEC long-term tests using FESEM and EDX. Figure 8a shows the
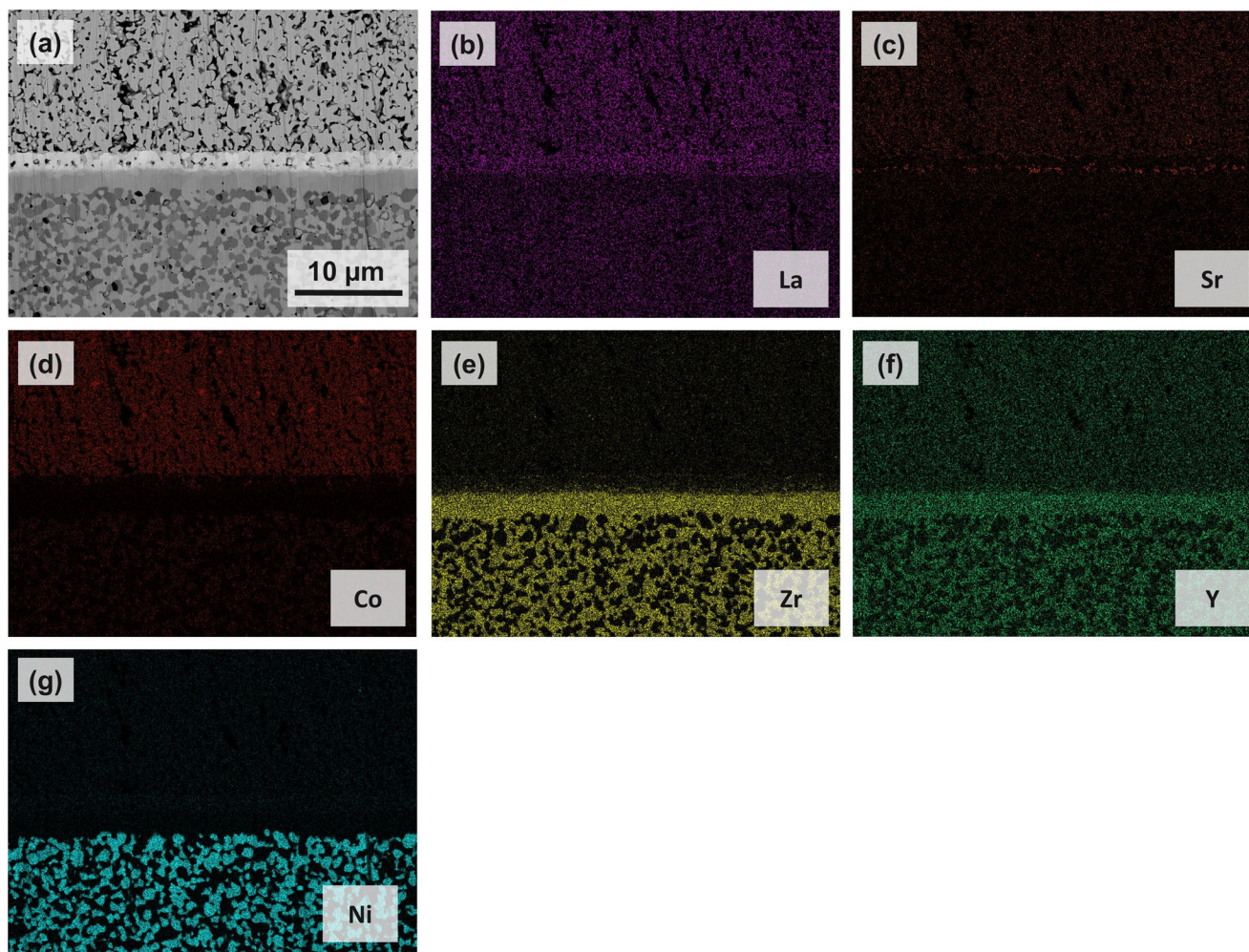
**FIGURE 6**  Cross-section image of a fresh 5×5 cm$^2$ anode-supported cell (ASC) with La$_{0.2}$Pr$_{0.2}$Nd$_{0.2}$Sm$_{0.2}$Sr$_{0.2}$CoO$_{3-\delta}$ (LPNSSC) air electrode recorded by (a) FESEM-BSE; (b–g) elemental maps for La, Sr, Co, Zr, Y, and Ni acquired by energy dispersive X-ray spectroscopy (EDX) in the same region.
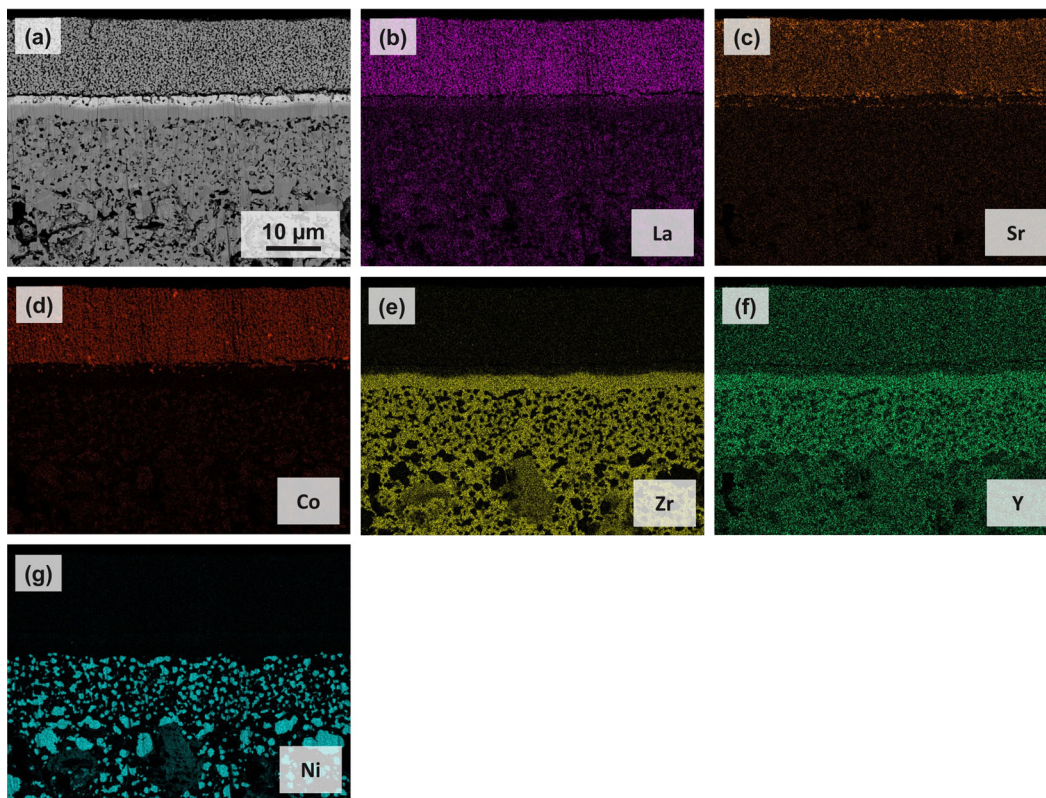
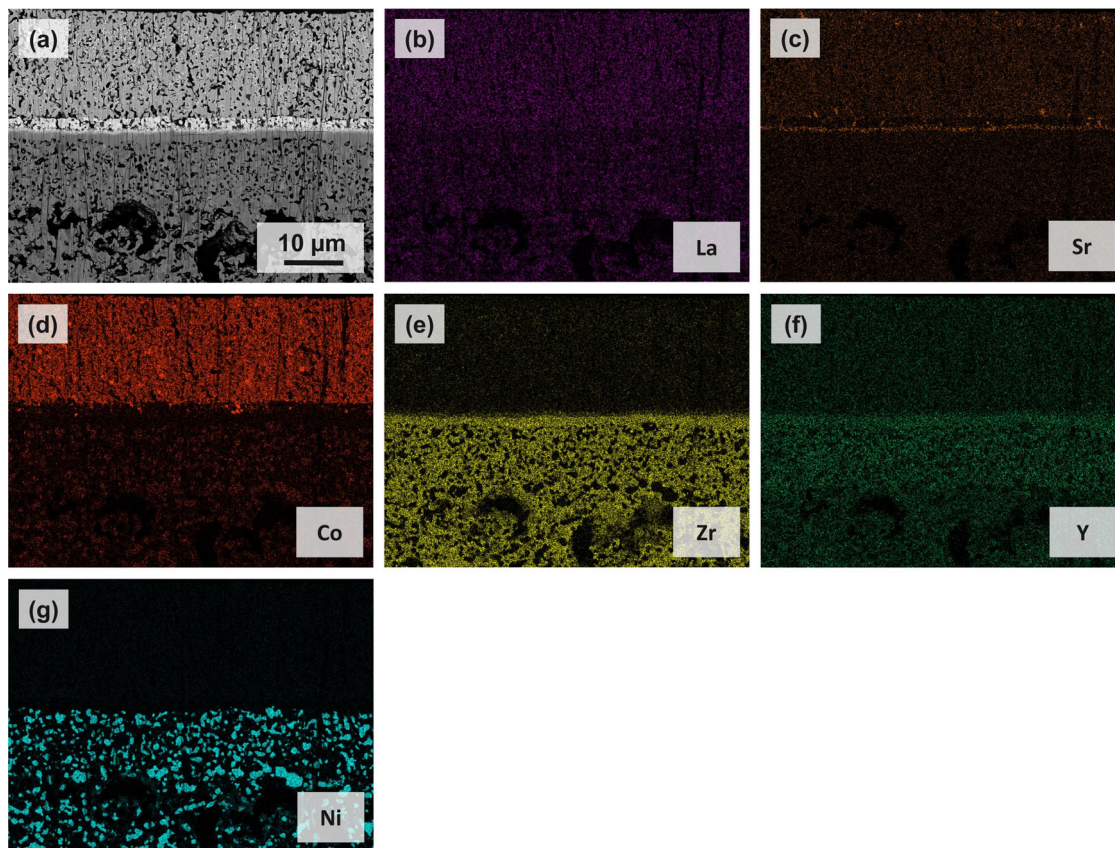post-mortem cross section image of the degraded LSC cell. The thickness of the LSC electrode is 12 μm (± 0.5 μm) and the porosity 33%. The average particle sizes of the grains within the LSC electrode are between 0.25 and 0.5 μm. At the LSC/GDC interface, severe delamination of the electrode is observed (Figure 8), which is a common failure mode in SOECs [15, 17, 46] and explains the degradation of the LSC cell during the long-term test (Figure 4). In addition, the EDX elemental map for Sr shown in Figure 8c indicates that Sr is enriched (compared to the bulk of the LSC electrode) in the near-surface region – as well as at the LSC/GDC and GDC/YSZ interfaces. The porosity of the GDC barrier estimated via thresholding is about 12%.

The post-mortem cross-section image of the degraded LPNSSC cell is shown in Figure 9a. The thickness of the LPNSSC electrode is 16 ± 0.3 μm and the porosity is estimated to be 22%. Comparing Figure 6a (fresh LPNSSC cell) and Figure 9a (post-mortem LPNSSC cell), the microstructure of the air electrode after long-term test-

ing is comparable to that of the as-prepared electrode in terms of thickness and porosity. The porosity of the GDC barrier of the LPNSSC cell is relatively high with 23% and thus SrZrO$_3$ (refer to Sr- and Zr-maps in Figure 9) is found at the YSZ/GDC interface, formed by cation interdiffusion between the air electrode and electrolyte through the barrier layer. Since SrZrO$_3$ formation usually occurs during sintering of the air electrode at elevated temperatures [45], these effects are ascribed mainly to pre-test processing and not to long-term degradation during cell testing at 800°C.

Figure 10a,b illustrates post-mortem surface FESEM images of the LSC electrode. In addition to the LSC grains, angular particles are observed, which appear in a darker contrast in the BSE image. Similar particles are also found in the post-mortem analysis of the LPNSSC surface (Figure 10c,d). According to the EDX elemental maps of the LPNSSC and LSC surfaces in Figures S9 and S10, these particles are composed of Sr, S and O, indicating the formation of SrSO$_4$, which is coupled to phase decomposition
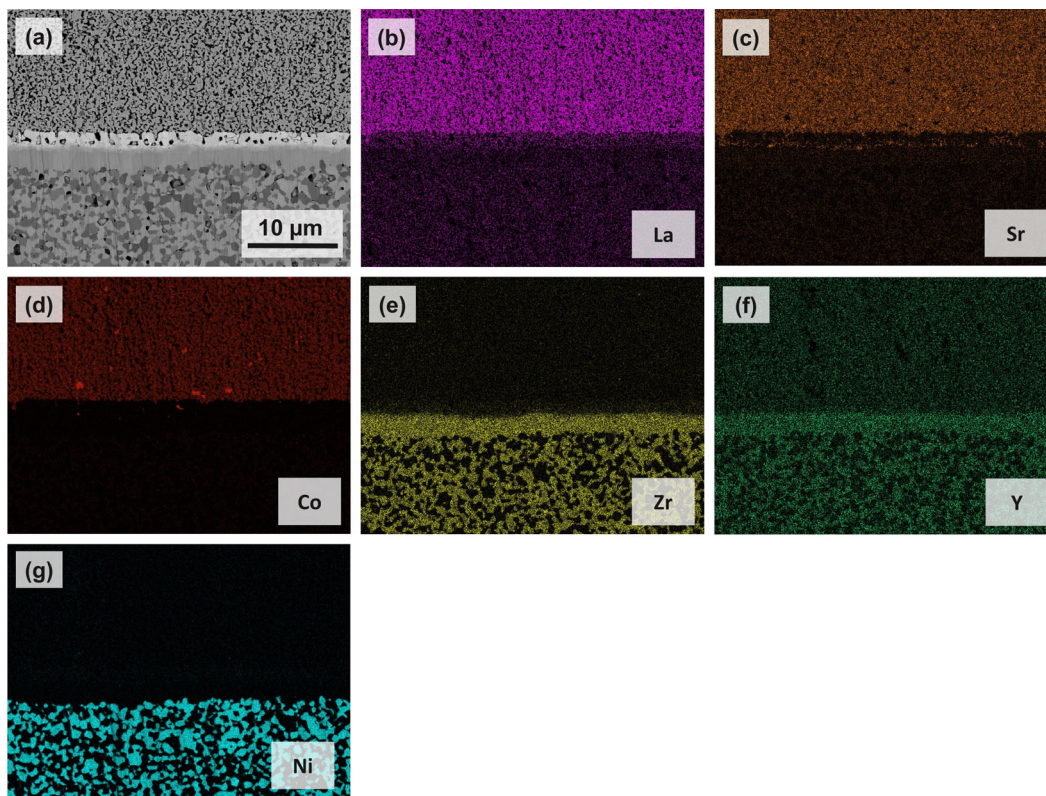
**FIGURE 7**     Cross-section image of a fresh 5×5 cm$^2$ anode-supported cell (ASC) with $La_{0.6}Sr_{0.4}CoO_{3-\delta}$ (LSC) air electrode recorded by (a) FESEM-BSE; (b–g) elemental maps for La, Sr, Co, Zr, Y, and Ni acquired by energy dispersive X-ray spectroscopy (EDX) in the same region.



**FIGURE 8**     Post-mortem cross-section image of a 5×5 cm$^2$ anode-supported cell (ASC) with $La_{0.6}Sr_{0.4}CoO_{3-\delta}$ (LSC) air electrode obtained by (a) FESEM-BSE after long-term polarization in solid oxide electrolysis cell (SOEC) mode; (b–g) elemental maps for La, Sr, Co, Zr, Y, and Ni acquired by energy dispersive X-ray spectroscopy (EDX) in the same sample region.

**FIGURE 9** Post-mortem cross-section image of a 5×5 cm$^2$ anode-supported cell (ASC) with La$_{0.2}$Pr$_{0.2}$Nd$_{0.2}$Sm$_{0.2}$Sr$_{0.2}$CoO$_{3-\delta}$ (LPNSSC) air electrode obtained by (a) FESEM-BSE after long-term polarization in solid oxide electrolysis cell (SOEC) mode; (b–g) elemental maps for La, Sr, Co, Zr, Y, and Ni acquired by energy dispersive X-ray spectroscopy (EDX) in the same sample region.
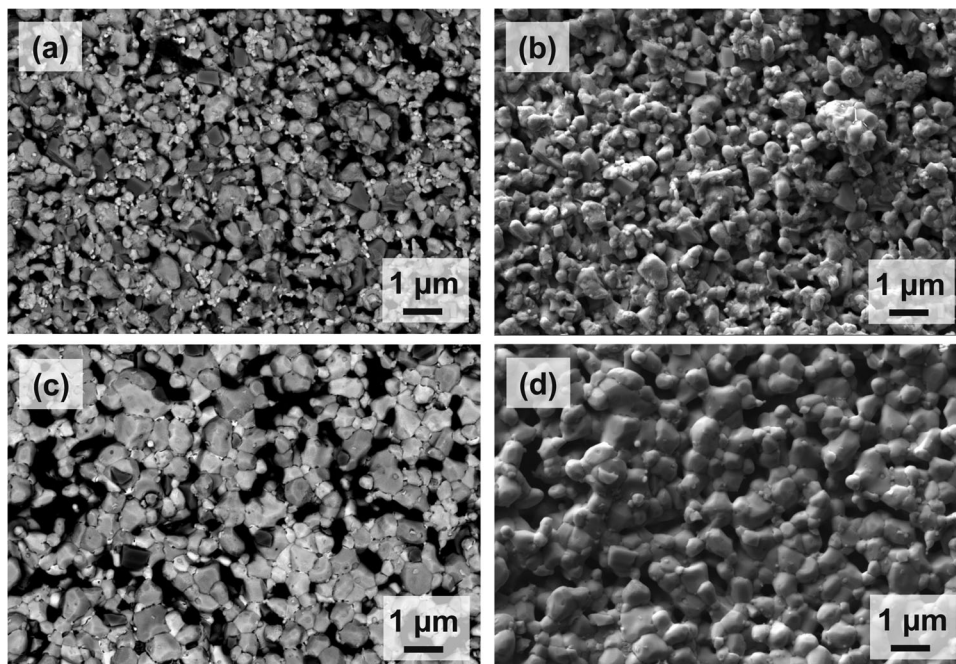


**FIGURE 10** Post-mortem microstructure images of the surface of (a, b) the La$_{0.6}$Sr$_{0.4}$CoO$_{3-\delta}$ (LSC) air electrode and (c, d) the La$_{0.2}$Pr$_{0.2}$Nd$_{0.2}$Sm$_{0.2}$Sr$_{0.2}$CoO$_{3-\delta}$ (LPNSSC) air electrode after long-term polarization of 5×5 cm$^2$ anode-supported cells (ASCs) in solid oxide electrolysis cell (SOEC) mode; images (a) and (c) were acquired by FESEM-BSE, images (b) and (d) by FESEM-SE.

of the perovskite phase, as previously reported in the literature [47–50]. A comparison of Figure 10a,c shows that the amount of this secondary phase is significantly less on the surface of the degraded LPNSSC electrode (~3% $SrSO_4$ after 700 h) than on the LSC electrode (~8% $SrSO_4$ after 400 h). The relative amount of $SrSO_4$ particles was determined using thresholding-based image analysis, whereby particles in question are distinguished from the bulk using differences in gray values as one criterion. Care was taken to complement the software-based selection by manually including $SrSO_4$ particles based on their distinctive angular shape.

In addition, the BSE images of both LSC and LPNSSC electrodes (Figure 10a,c) feature small particles, which appear as bright spots. EDX analysis shows that these are Pt particles originating from the Pt paste used for current collection at the air electrode. Post-mortem analyses of the Ni-YSZ fuel electrodes (Figures 8 and 9) show no significant differences between the LSC and LPNSSC cells, confirming that the observed degradation (Figure 4) is mainly due to changes at the air electrodes.

## 4 | CONCLUSIONS

Solid oxide cells with high-entropy perovskite LPNSSC air electrodes are characterized with regard to electrochemical performance and microstructure. For a planar 5×5 cm$^2$ cell, a current density of −1.24 A/cm$^2$ is reached in SOEC mode at 1.2 V and 800°C with 90% humidity (rest H$_2$). This performance surpasses that of a commercial cell with state-of-the-art LSC air electrodes for identical test conditions. Long-term electrolysis during 700 h at 800°C reveals remarkable long-term stability of the LPNSSC cell. Under the same conditions, the voltage of the LSC cell increases continuously for 400 h. According to post-test analyses, the differences in stability during long-term testing can be attributed to the LSC and LPNSSC air electrodes. While delamination of the LSC electrode occurred at the LSC/GDC interface, good adhesion of LPNSSC was observed even after 700 h of electrolysis. The air electrode surfaces of both cells show the formation of secondary phases, especially $SrSO_4$. However, significantly less $SrSO_4$ is formed on LPNSSC compared to LSC.

In conclusion, the high-entropy perovskite LPNSSC is a promising option for SOC air electrodes. While LPNSSC cells can compete with − or even surpass – SOTA cells based on LSC with respect to electrochemical performance, they could be especially advantageous regarding long-term stability in SOEC mode. Two of the most critical problems of SOC air electrodes, namely delamination and secondary phase formation due to Sr segregation and $SO_2$ poisoning, are alleviated compared to SOTA LSC electrodes. Further development of LPNSSC air electrodes is aimed at optimizing the microstructure (e.g., grain sizes, porosity, tortuosity, etc.) to further enhance the electrode performance [51–53]. In addition, the issue of $SrZrO_3$ formation at the electrolyte-barrier layer interface should be addressed, mainly by decreasing the porosity of the GDC diffusion barrier.

## ORCID
*Patrick Pretschuh* https://orcid.org/0000-0002-8807-122X
*Andreas Egger* https://orcid.org/0000-0002-1577-4725
*Edith Bucher* https://orcid.org/0000-0002-9017-9555

## REFERENCES
1. P. P. Edwards, V. L. Kuznetsov, W. I. F. David, N. P. Brandon, *Energy Policy* **2008**, *36*, 4356.
2. N. Z. Muradov, T. N. Veziroğlu, *Int. J. Hydrogen Energy* **2008**, *33*, 6804.
3. Y. Zhou, R. Li, Z. Lv, J. Liu, H. Zhou, C. Xu, *Chin. J. Chem. Eng.* **2022**, *43*, 2.
4. I. P. Jain, *Int. J. Hydrogen Energy* **2009**, *34*, 7368.
5. R. Shinnar, *Technol. Soc.* **2003**, *25*, 455.
6. K. C. Sabat, A. B. Murphy, *Metall. Mater. Trans. B* **2017**, *48*, 1561.
7. O. Posdziech, T. Geißler, K. Schwarze, R. Blumentritt, *ECS Trans.* **2019**, *91*, 2537.
8. C. Lenser, D. Udomsilp, N. Menzler, P. Holtappels, T. Fujisaki, K. Leonard, H. Matsumoto, A. Sabato, F. Smeacetto, A. Chrysanthou, S. Molin, *Advanced Ceramics for Energy Conversion and Storage* In (Eds: O. Guillon), Elsevier, **2019**, p. 387. https://doi.org/10.1016/B978-0-08-102726-4.00009-0
9. S. Y. Gómez, D. Hotza, *Renew. Sustain. Energy Rev.* **2016**, *61*, 155.
10. K. Motylinski, J. Kupecki, B. Numan, Y. S. Hajimolana, V. Venkataraman, *Energy Conver. Manag.* **2021**, *228*, 113674.
11. F. Wang, L. Wang, Y. Ou, X. Lei, J. Yuan, X. Liu, Y. Zhu, *Case Stud. Thermal Eng.* **2021**, *27*, 101240.
12. O. Schmidt, A. Gambhir, I. Staffell, A. Hawkes, J. Nelson, S. Few, *Int. J. Hydrogen Energy* **2017**, *42*, 30470.
13. M. S. Khan, X. Xu, R. Knibbe, Z. Zhu, *Renew. Sustain. Energy Rev.* **2021**, *143*, 110918.
14. Y. Wang, W. Li, L. Ma, W. Li, X. Liu, *Journal of Mater. Sci. Technol.* **2020**, *55*, 35.
15. I. Sreedhar, B. Agarwal, P. Goyal, A. Agarwal, *J. Solid State Electrochem.* **2020**, *24*, 1239.
16. P. Moçoteguy, A. Brisse, *Int. J. Hydrogen Energy* **2013**, *38*, 15887.
17. A. V. Virkar, *Int. J. Hydrogen Energy* **2010**, *35*, 9527.
18. L. C. Baqué, A. L. Soldati, E. Teixeira-Neto, H. E. Troiani, A. Schreiber, A. C. Serquis, *J. Power Sources* **2017**, *337*, 166.

19. K. Develos-Bagarinao, J. De Vero, H. Kishimoto, T. Ishiyama, K. Yamaji, T. Horita, H. Yokokawa, *Phys. Chem. Chem. Phys.* **2019**, *21*, 7183.

20. E. Ostrovskiy, Y.-L. Huang, E. D. Wachsman, *J. Mater. Chem. A* **2021**, *9*, 1593.

21. S. P. Simner, M. D. Anderson, M. H. Engelhard, J. W. Stevenson, *Electrochem. Solid State Lett.* **2006**, *9*, A478.

22. K. Chen, S. P. Jiang, *Electrochem. Energy Rev.* **2020**, *3*, 730.

23. G. M. Rupp, H. Téllez, J. Druce, A. Limbeck, T. Ishihara, J. Kilner, J. Fleig, *J. Mater. Chem. A* **2015**, *3*, 22759.

24. A. K. Opitz, C. Rameshan, M. Kubicek, G. M. Rupp, A. Nenning, T. Götsch, R. Blume, M. Hävecker, A. Knop-Gericke, G. Rupprechter, B. Klötzer, J. Fleig, *Topics Catal.* **2018**, *61*, 2129.

25. N. K. Patel, R. G. Utter, D. Das, M. Pecht, *J. Power Sources* **2019**, *438*, 227040.

26. M. A. R. Niania, A. K. Rossall, J. A. Van den Berg, J. A. Kilner, *J. Mater. Chem. A* **2020**, *8*, 19414.

27. C. M. Rost, E. Sachet, T. Borman, A. Moballegh, E. C. Dickey, D. Hou, J. L. Jones, S. Curtarolo, J.-P. Maria, *Nat. Commun.* **2015**, *6*, 8485.

28. P. A. Krawczyk, M. Jurczyszyn, J. Pawlak, W. Salamon, P. Baran, A. Kmita, Ł. Gondek, M. Sikora, C. Kapusta, T. Strączek, J. Wyrwa, A. Żywczak, *ACS Appl. Electr. Mater.* **2020**, *2*, 3211.

29. S. Jiang, T. Hu, J. Gild, N. Zhou, J. Nie, M. Qin, T. Harrington, K. Vecchio, J. Luo, *Scripta Materialia* **2018**, *142*, 116.

30. A. Sarkar, Q. Wang, A. Schiele, M. R. Chellali, S. S. Bhattacharya, D. Wang, T. Brezesinski, H. Hahn, L. Velasco, B. Breitung, *Adv. Mater.* **2019**, *31*, 1806236.

31. L. Shen, Z. Du, Y. Zhang, X. Dong, H. Zhao, *Appl. Catal. B Environ.* **2021**, *295*, 120264.

32. Y. Yang, H. Bao, H. Ni, X. Ou, S. Wang, B. Lin, P. Feng, Y. Ling, *J. Power Sources* **2021**, *482*, 228959.

33. Q. Yang, G. Wang, H. Wu, B. A. Beshiwork, D. Tian, S. Zhu, Y. Yang, X. Lu, Y. Ding, Y. Ling, Y. Chen, B. Lin, *J. Alloys Compounds* **2021**, *872*, 159633.

34. J. Dąbrowa, A. Olszewska, A. Falkenstein, C. Schwab, M. Szymczak, M. Zajusz, M. Moździerz, A. Mikuła, K. Zielińska, K. Berent, T. Czeppe, M. Martin, K. Świerczek, *J. Mater. Chem. A* **2020**, *8*, 24455.

35. A. N. Petrov, O. F. Kononchuk, A. V. Andreev, V. A. Cherepanov, P. K. Kofstad, *Solid State Ionics* **1995**, *80*, 189.

36. A. Egger, E. Bucher, M. Yang, W. Sitte, *Solid State Ionics* **2012**, *225*, 55.

37. A. Egger, M. Perz, E. Bucher, C. Gspan, W. Sitte, *Fuel Cells* **2019**, *19*, 458.

38. P. Hjalmarsson, M. Søgaard, M. Mogensen, *Solid State Ionics* **2008**, *179*, 1422.

39. R. Shannon, *Acta Crystallographica Sect. A* **1976**, *32*, 751.

40. J. Fleig, *Solid State Ionics* **2002**, *150*, 181.

41. B. Königshofer, M. Höber, G. Nusev, P. Boškoski, C. Hochenauer, V. Subotić, *J. Power Sources* **2022**, *523*, 230982.

42. X. Sun, P. V. Hendriksen, M. B. Mogensen, M. Chen, *Fuel Cells* **2019**, *19*, 740.

43. T. L. Skafte, O. B. Rizvandi, A. L. Smitshuysen, H. L. Frandsen, J. V. Thorvald Høgh, A. Hauch, S. K. Kær, S. S. Araya, C. Graves, M. B. Mogensen, S. H. Jensen, *J. Power Sources* **2022**, *523*, 231040.

44. C. A. Schneider, W. S. Rasband, K. W. Eliceiri, *Nat. Methods* **2012**, *9*, 671.

45. J. Szász, F. Wankmüller, V. Wilde, H. Störmer, D. Gerthsen, N. H. Menzler, E. Ivers-Tiffée, *J. Electrochem. Soc.* **2018**, *165*, F898.

46. Z. Pan, Q. Liu, Z. Yan, Z. Jiao, L. Bi, S. H. Chan, Z. Zhong, *Electrochem. Commun.* **2022**, *137*, 107267.

47. E. Bucher, C. Gspan, F. Hofer, W. Sitte, *Solid State Ionics* **2013**, *238*, 15.

48. E. Bucher, C. Gspan, W. Sitte, *Solid State Ionics* **2015**, *272*, 112.

49. H. Yokokawa, N. Sakai, T. Horita, K. Yamaji, (Eds.), *Handbook of Fuel Cells*, John Wiley & Sons, Ltd., Hoboken **2009**. p. 979.

50. F. Wang, H. Kishimoto, T. Ishiyama, K. Develos-Bagarinao, K. Yamaji, T. Horita, H. Yokokawa, *J. Power Sources* **2020**, *478*, 228763.

51. M. Laguna-Bercero, R. Campana, Á. Larrea, J. A. Kilner, V. M. Orera, *J. Power Sources* **2011**, *196*, 8942.

52. S. Kim, D. W. Joh, D.-Y. Lee, J. Lee, H. S. Kim, M. Z. Khan, J. E. Hong, S.-B. Lee, S. J. Park, R.-H. Song, M. T. Mehran, C. K. Rhee, T.-H. Lim, *Chem. Eng. J.* **2021**, *410*, 128318.

53. W. Li, Y. Shi, Y. Luo, N. Cai, *Int. J. Hydrogen Energy* **2014**, *39*, 13738.

## SUPPORTING INFORMATION

Additional supporting information can be found online in the Supporting Information section at the end of this article.

# Supplementary Material

## Electrochemical and Microstructural Characterization of the High-entropy Perovskite $La_{0.2}Pr_{0.2}Nd_{0.2}Sm_{0.2}Sr_{0.2}CoO_{3-\delta}$ for Solid Oxide Cell Air Electrodes

Patrick Pretschuh[1], Andreas Egger[1], Roland Brunner[2], Edith Bucher[1]

[1]Montanuniversitaet Leoben, Chair of Physical Chemistry, Franz-Josef-Straße 18, AT-8700 Leoben, Austria

[2]Materials Center Leoben Forschung GmbH, Roseggerstraße 12, AT-8700 Leoben, Austria

## S-1. Introduction

High-entropy perovskites (HEP) are formed by mixing $n \geq 5$ cations on the A- and/or B-sites of the crystal lattice $ABO_3$. The configurational entropy $S_{config}$ of a HEP can be calculated from the following equation, where $x_i$ is the molar fraction of the element $i$ and $R$ is the universal gas constant. By definition, HEPs have $S_{config} \geq 1.5\,R$ [1].

$$S_{config} = -R \left[ \left( \sum_{a=1}^{n_1} x_a ln x_a \right)_{A-site} + \left( \sum_{b=1}^{n_2} x_b ln x_b \right)_{B-site} + 3 \left( \sum_{c=1}^{n_3} x_c ln x_c \right)_{O-site} \right] \quad \text{Eq. S-1}$$

- $S_{config} \geq 1.5\,R$: High-entropy perovskites (HEP)
- $1.5\,R > S_{config} \geq 1\,R$: Medium-entropy perovskites (MEP)
- $1\,R > S_{config}$: Low-entropy perovskites (LEP)

## S-2. Electrochemical Characterization

Table S-1: Parameter sets as obtained from complex non-linear least squares fits to the impedance spectra of the button cell with LPNSSC air electrode in Figure 2 of the main text.

| $T$ / °C | 800 | 750 | 700 | 650 |
|---|---|---|---|---|
| $L$ / H | 2.671E-7 | 2.670E-7 | 2.674E-7 | 2.677E-7 |
| $R_0$ / Ω cm² | 0.051 | 0.066 | 0.090 | 0.143 |
| $R_1$ / Ω cm² | 0.110 | 0.222 | 0.299 | 0.463 |
| $C_1$ / F cm⁻² | 2.189E-5 | 2.342E-6 | 1.314E-6 | 1.449E-6 |
| $R_2$ / Ω cm² | 0.056 | 0.057 | 0.570 | 1.038 |
| $C_2$ / F cm⁻² | 0.034 | 0.011 | 0.002 | 0.007 |
| $R_3$ / Ω cm² | 0.272 | 0.347 | 0.170 | 0.479 |
| $C_3$ / F cm⁻² | 0.249 | 0.178 | 0.488 | 0.020 |
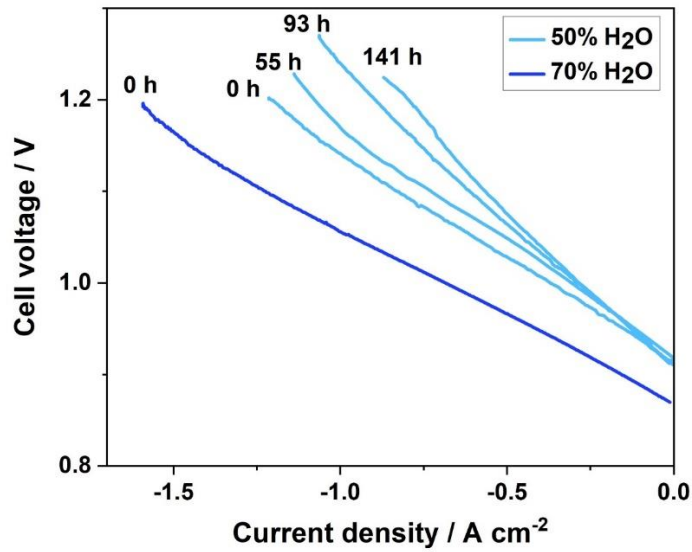
Figure S-1: Current-voltage curves of a button cell with LPNSSC air electrode in SOEC mode at different humidification levels and at different times. Gas flows were 60 mL min$^{-1}$ 20% $O_2$ (rest Ar) at the air electrode, and 40 mL min$^{-1}$ $H_2$ with 3% $H_2O$ at the fuel electrode.
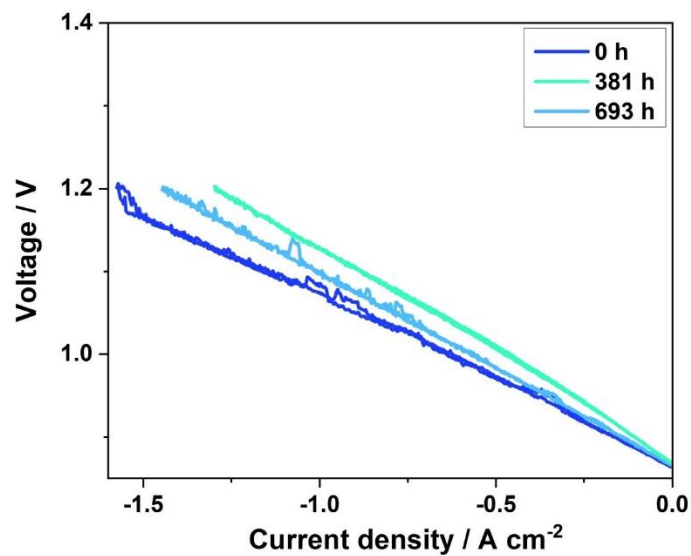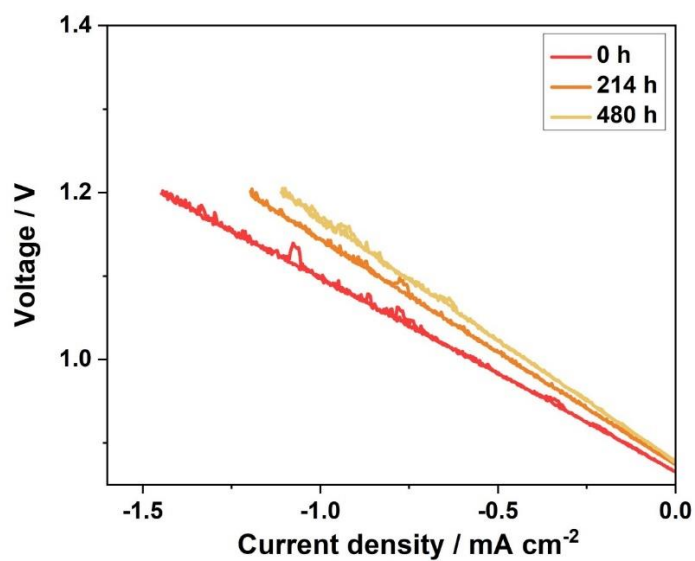


Figure S-2: Current-voltage curves of a 5x5 cm² ASC with LPNSSC air electrode recorded at 800 °C during long-term electrolysis (-0.983 A/cm²) at 80% $H_2O$ (rest $H_2$) and 1 L min$^{-1}$ fuel gas flow.
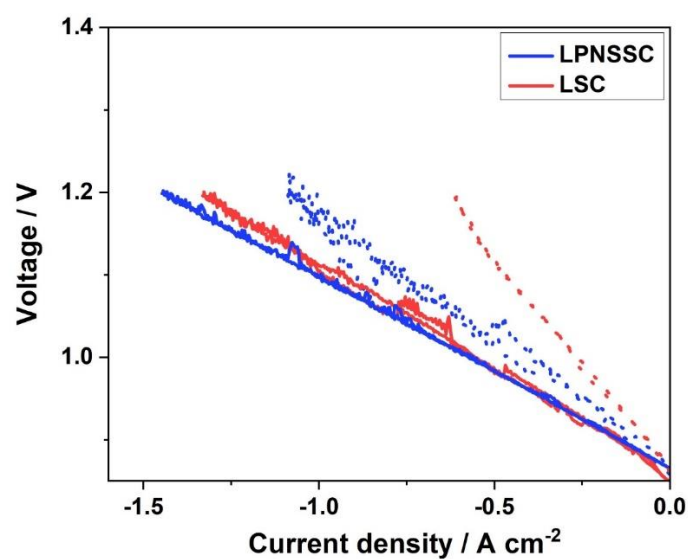
Figure S-3: Current-voltage curves of a 5x5 cm² ASC with LSC air electrode recorded at 800 °C during long-term electrolysis (-0.983 A/cm²) at 80% $H_2O$ (rest $H_2$) and 1 L min⁻¹ fuel gas flow.



Figure S-4: Current-voltage curves of 5x5 cm² ASCs with LPNSSC and LSC air electrodes tested at 80% $H_2O$ (rest $H_2$) and 1 L min⁻¹ fuel gas flow; broken lines show curves of the same cells with 0.25 L min⁻¹ fuel gas flow. The curves were recorded at 800 °C before the start of the long-term tests.

## S-3. Microstructure
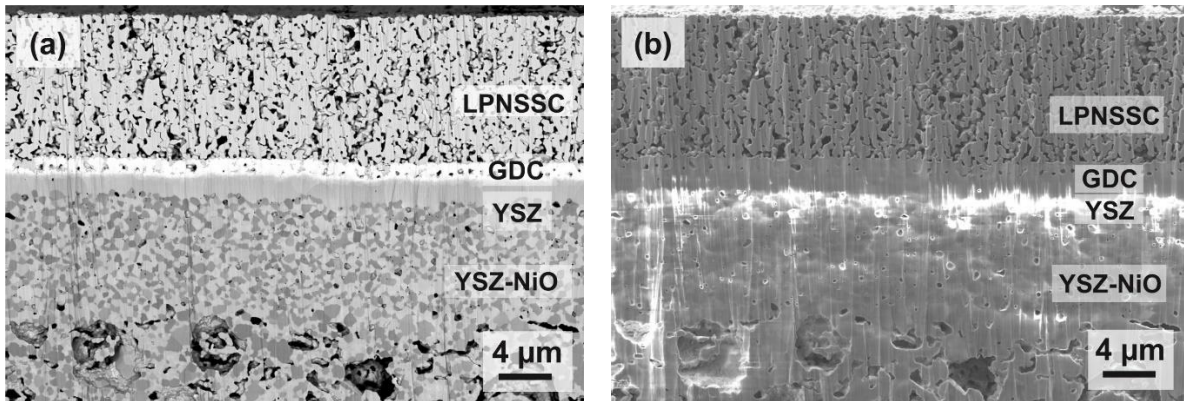


Figure S-5: Cross section images of a fresh 5x5 cm² ASC with LPNSSC air electrode in (a) FESEM-BSE and (b) FESEM-SE mode, showing the air electrode/diffusion barrier/electrolyte/fuel electrode interfaces (fuel electrode is still in oxidized state, NiO-YSZ).
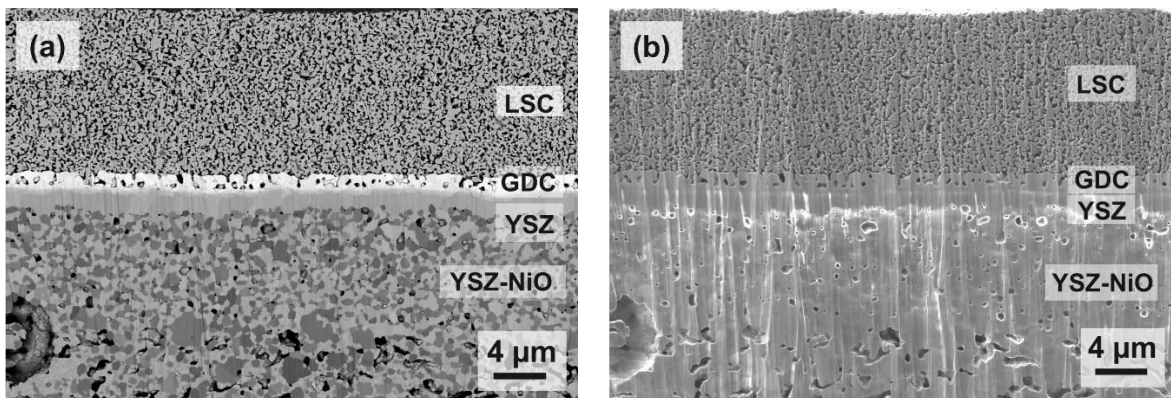


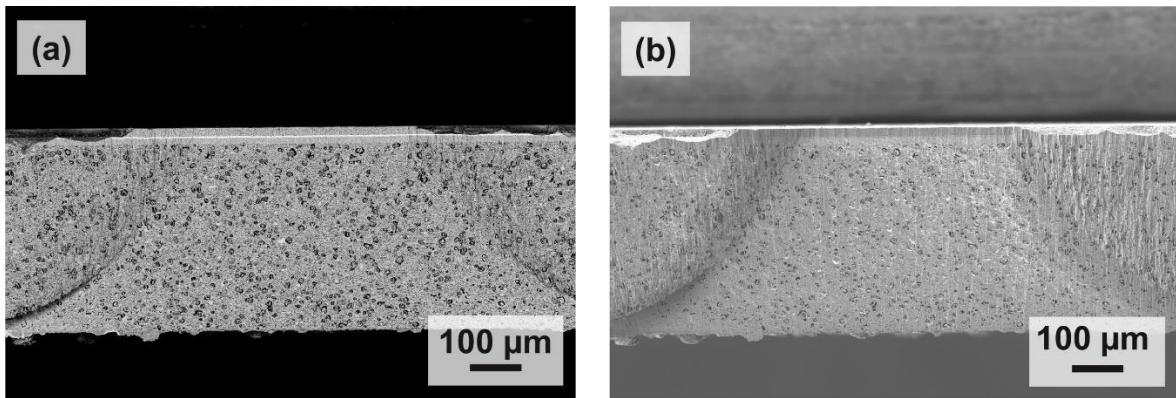Figure S-6: Cross section images of a fresh commercial 5x5 cm² ASC with LSC air electrode in (a) FESEM-BSE and (b) FESEM-SE mode, showing the air electrode/diffusion barrier/electrolyte/fuel electrode interfaces (fuel electrode is still in oxidized state, NiO-YSZ).
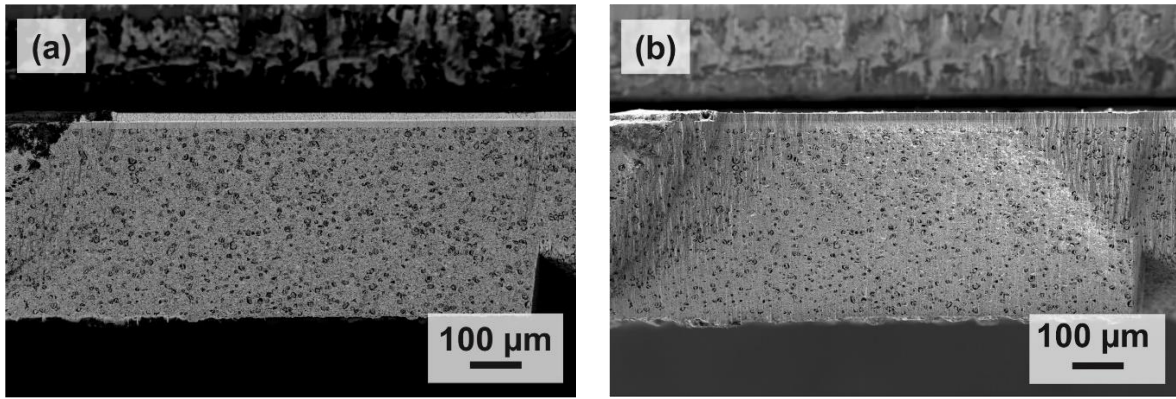
Figure S-7: Cross section images of a fresh 5x5 cm² ASC with LPNSSC air electrode in (a) FESEM-BSE and (b) FESEM-SE mode.



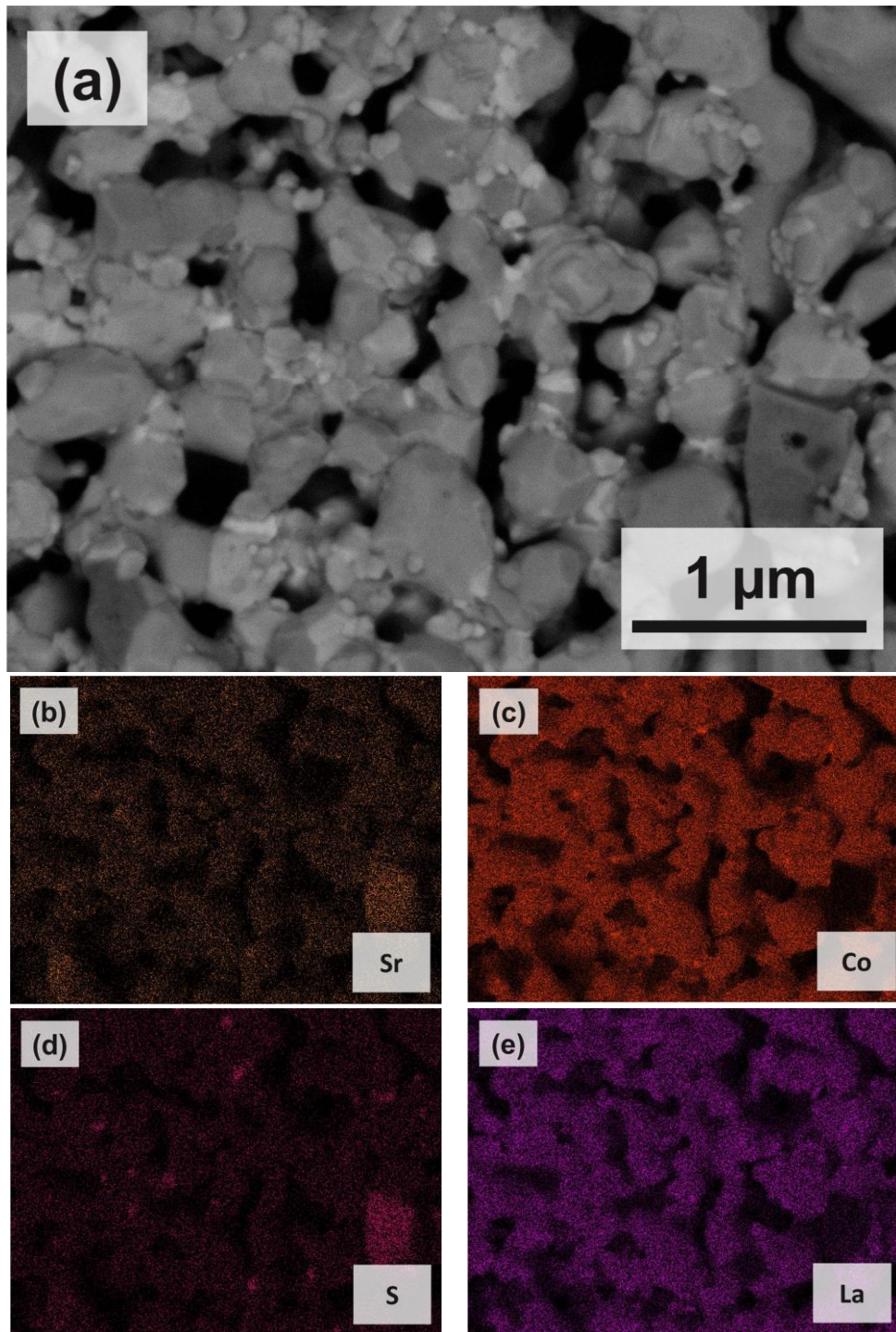Figure S-8: Cross section images of a fresh commercial 5x5 cm² ASC with LSC air electrode in (a) FESEM-BSE and (b) FESEM-SE mode.
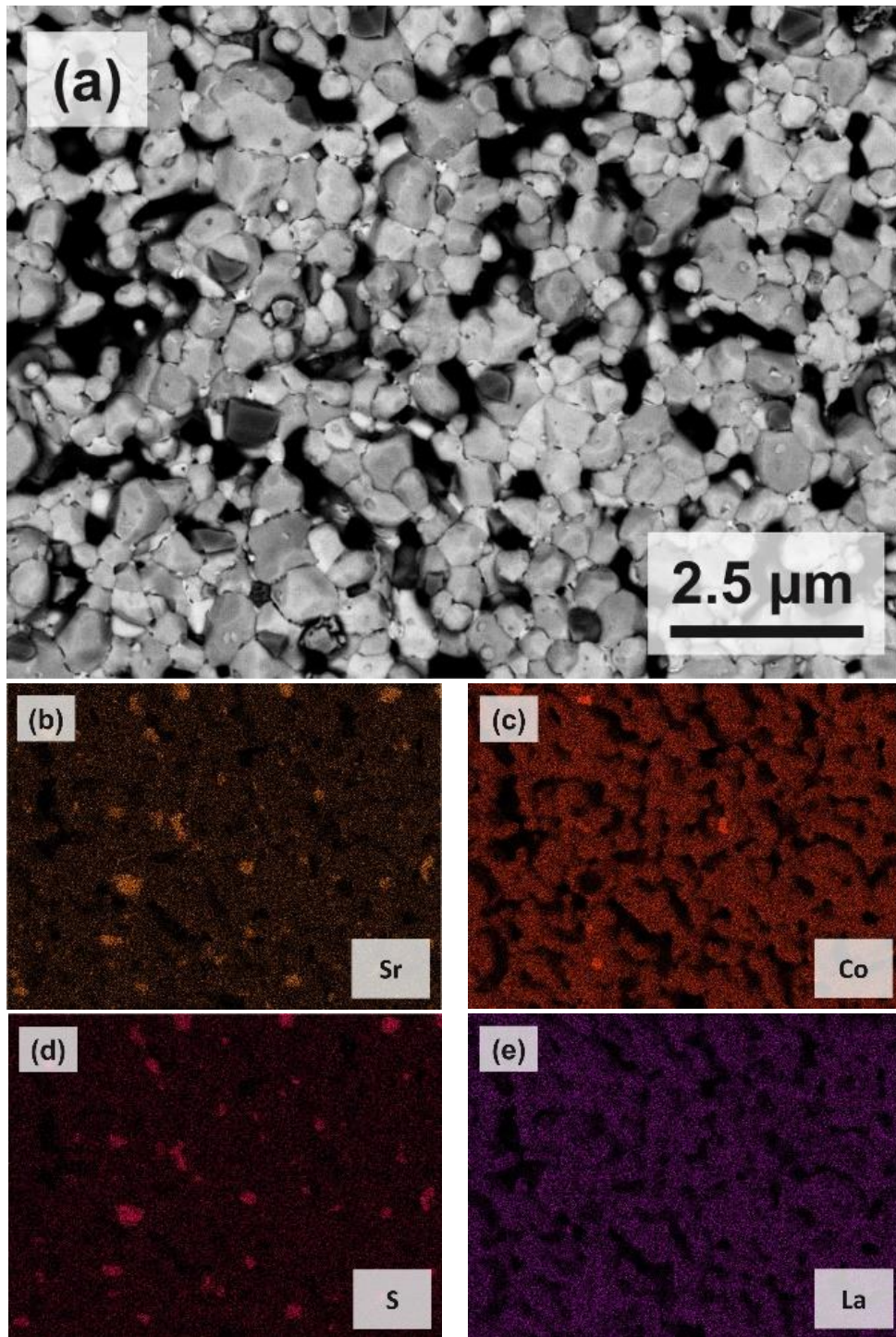
Figure S-9: Post-mortem microstructure image of the surface of (a) the LPNSSC air electrode acquired by FESEM-BSE after long-term polarization of a 5x5 cm² ASC in SOEC mode; (b) – (e) elemental maps for Sr, Co, S and La acquired by EDX in the same surface region.

Figure S-10: Post-mortem microstructure image of the surface of (a) the LSC air electrode acquired by FESEM-BSE after long-term polarization of a 5x5 cm² ASC in SOEC mode; (b) – (e) elemental maps for Sr, Co, S and La acquired by EDX in the same surface region.

**S-4.  References**

[1]   A. Sarkar, Q. Wang, A. Schiele, M.R. Chellali, S.S. Bhattacharya, D. Wang, T. Brezesinski, H. Hahn, L. Velasco, B. Breitung, *Advanced Materials* **2019**, *31*, 1806236.

**RESEARCH ARTICLE** OPEN ACCESS

# Cobalt-Free High-Entropy Perovskite La$_{0.2}$Pr$_{0.2}$Nd$_{0.2}$Sm$_{0.2}$Sr$_{0.2}$FeO$_{3-\delta}$ Solid Oxide Cell Air Electrode With Enhanced Performance

Patrick Pretschuh[1] | Andreas Egger[1] | Priya Paulachan[2] | Johanna Schöggl[2] | Roland Brunner[2] | Edith Bucher[1]

[1]Montanuniversitaet Leoben, Chair of Physical Chemistry, Leoben, Austria | [2]Materials Center Leoben Forschung GmbH, Leoben, Austria

**Correspondence:** Edith Bucher (edith.bucher@unileoben.ac.at)

## ABSTRACT

This study investigates the novel cobalt-free high-entropy perovskite, La$_{0.2}$Pr$_{0.2}$Nd$_{0.2}$Sm$_{0.2}$Sr$_{0.2}$FeO$_{3-\delta}$ (LPNSSF), as an air electrode material for solid oxide cells (SOCs). When testing a button cell with a single-phase LPNSSF electrode, a current density of 0.55 A cm$^{-2}$ is obtained at 0.7 V in fuel cell mode at 800°C. In order to mitigate the moderate electronic conductivity of LPNSSF, two approaches are explored. Incorporating a Co-free highly conductive perovskite, LaNi$_{0.6}$Fe$_{0.4}$O$_{3-\delta}$ (LNF), either as an LPNSSF–LNF composite electrode or as a current collector layer (CCL), enhances the performance to 0.61 and 0.66 A cm$^{-2}$, respectively, under the same conditions. Microstructural features are studied by electron microscopy and show a rather dense structure of the CCL. Optimization of the current collector increases the current density further to 0.96 A cm$^{-2}$ at 0.7 V in a 5 × 5 cm$^2$ anode-supported cell at 800°C. This cell exhibits good long-term stability in electrolysis mode in H$_2$-H$_2$O with 80% humidification. Continuous polarization of −0.69 A cm$^{-2}$ is sustained for 1000 h, with an average degradation rate of 10 mV kh$^{-1}$ after an initial run-in phase. These findings demonstrate the promising performance and durability of LPNSSF as cobalt-free SOC air electrode.

## 1 | Introduction

With the rapidly growing commitment to sustainable energy solutions, solid oxide electrolysis cells (SOECs) and solid oxide fuel cells (SOFCs) have emerged as promising technologies that can transform the landscape of electrochemical energy storage and conversion. Solid oxide cells (SOCs) exhibit exceptionally high efficiencies at the cell and system level, which clearly exceed those of other technologies [1–3]. In the future, they may offer an economically viable bridge between renewable energy sources and reliable, on-demand power supply and storage systems [4]. Central to the success of SOEC and SOFC technologies is the

development of robust air electrodes, a critical component that facilitates the electrochemical reactions in these cells [5, 6].

To date, cobalt-containing air electrodes have played a pivotal role in enhancing the performance of SOCs. However, growing concerns relate to the resource scarcity of cobalt, coupled with its environmental and ethical implications. The material not only faces supply chain challenges but also raises ethical questions regarding its extraction and processing [7]. In addition, the substitution of Co with non-critical elements might tackle cost issues and thus increase the competitiveness of SOC technologies [8]. For these reasons, research activities for developing

alternative Co-free air electrode materials have been gaining in importance in recent years [9–12]. A major challenge in this effort lies in the fact that Co-free materials are usually less catalytically active and often exhibit significantly lower electronic conductivity than state-of-the-art electrodes containing cobalt. For example, the electronic conductivity of commonly used air electrode materials $La_{0.6}Sr_{0.4}Co_{0.2}Fe_{0.8}O_{3-\delta}$ and $La_{0.6}Sr_{0.4}CoO_{3-\delta}$ is 270 [13] and 1600 S cm$^{-1}$ [13], respectively.

High-entropy perovskites (HEPs), containing five or more elements on the A- and/or B-site of the perovskite structure $ABO_3$, are an interesting material class that has emerged in recent years [14]. Their application as highly performing and long-term stable air electrodes in SOCs has been successfully demonstrated for cobalt-containing compositions [15–17]. The present study aims at showing that excellent performance and good long-term stability can also be achieved with cobalt-free HEP electrodes, provided that the cell design is optimized in terms of phase composition, microstructure, and current collection. Because iron is widely available, using a ferrite as an air electrode material aids in obtaining independence from critical resources and lowers the raw material costs. In addition, Fe-based perovskites exhibit lower thermal expansion coefficients than Co-based materials and are thus thermomechanically more compatible with common electrolyte and diffusion barrier materials [18–21]. Thus, the composition $La_{0.2}Pr_{0.2}Nd_{0.2}Sm_{0.2}Sr_{0.2}FeO_{3-\delta}$ (LPNSSF) was selected as an air electrode material, and its electrochemical properties as well as long-term stability were studied both in fuel cell and electrolysis mode. The impact of variations in electrode configuration is evaluated by comparing single-phase LPNSSF with LPNSSF-based air electrodes, the overall electrical conductivity of which has been enhanced either by composite formation or by using an additional current collector layer (CCL). In this work, the cobalt-free perovskite $LaNi_{0.6}Fe_{0.4}O_{3-\delta}$ (LNF) is applied both as a composite component as well as a current collector, as it provides a high electronic conductivity of 580 S cm$^{-1}$ [22, 23] compared to 90 S cm$^{-1}$ for LPNSSF at 800°C.

## 2 | Experimental Procedures

### 2.1 | Material and Cell Preparation

LPNSSF powder is synthesized using a citric acid (CA)–ethylenediaminetetraacetic acid (EDTA) sol–gel method. Stoichiometric amounts of the metal nitrates, that is, $La(NO_3)_3 \cdot 6H_2O$, $Pr(NO_3)_3 \cdot 6H_2O$, $Nd(NO_3)_3 \cdot 6H_2O$, $Sm(NO_3)_3 \cdot 6H_2O$, $Sr(NO_3)_2$, and $Fe(NO_3)_2 \cdot 6H_2O$ (all purchased from Aldrich with a purity of ≥99.0%), are dissolved in deionized water. The stirred mixture is heated until the salts are dissolved, and then 1 mol of anhydrous CA per mole of cations is added. The pH of the solution is adjusted to 8 using an aqueous ammonia solution. Subsequently, the solution is heated on a hot plate to remove water and create a gel. After the water has completely evaporated, spontaneous combustion occurs. The temperature of the hot plate is maintained until the gel is transformed into raw ash. The resulting powder is homogenized using an agate mortar and is then calcined at 1100°C for 4 h in ambient air, with heating and cooling rates of 5 K min$^{-1}$.

The particle size distribution of the ceramic powders is determined by laser diffraction using a particle size analyzer PAS 1090 (Anton Paar). The calcined LPNSSF powder is milled for 4 h on a rolling bench using 3 mm diameter zirconia balls in ethanol until a particle size distribution with a $d_{50}$ of approximately 1.0 μm is reached. Commercially available LNF powder with a $d_{50}$ of approximately 1.0 μm (purchased from EMPA, Switzerland) was used for all experiments with symmetrical cells and button cells. For the 5 × 5 cm$^2$ cell, a coarser LNF powder (particle size 10 μm) was synthesized by the glycine-nitrate method [24]. In this process, aqueous 1 M solutions of $La(NO_3)_3 \cdot 6H_2O$ (Fluka, puriss. p.a.), $Fe(NO_3)_3 \cdot 9H_2O$ (Riedel-de Haën, puriss. p.a.), and $Ni(NO_3)_2 \cdot 6H_2O$ (Merck, p.a.) are mixed in the appropriate amounts required for the targeted cation stoichiometry. Glycine (Sigma-Aldrich, ≥99%) is added as a chelating and combustion agent with the ratio of glycine to cations being 2:1. The resulting solution is stirred and heated on a hot plate. Water is evaporated to obtain a gel, which ignites upon further heating. The obtained raw ash is calcined in ambient air for 4 h at 1000°C with heating and cooling rates of 5 K min$^{-1}$.

A terpineol-based ink vehicle containing 14 wt.% polyvinyl butyral is used to produce screen-printing pastes containing 66 wt.% active air electrode material. The fabricated current collector paste contains 33 wt.% LNF. The pastes are screen-printed onto the substrates using T32 polyester screens. Substrates for the symmetrical cells are fabricated from $Ce_{0.9}Gd_{0.1}O_{1.95}$ (GDC) powder purchased from CerPoTech, which is uniaxially pressed in a 2.5 diameter die with 2 t and subsequently isostatically pressed at 240 MPa. The disks are sintered at 1450°C for 10 h with 2 K min$^{-1}$ heating rate and 1 K min$^{-1}$ cooling rate. The air electrodes (active area 0.79 cm$^2$) are screen-printed on both sides of the GDC substrates. Commercially available 2 cm diameter round anode-supported cell (ASC) substrates and 5 × 5 cm$^2$ ASC substrates (both purchased from Elcogen AS) are used for the fabrication of full cells. In both cases, the cell substrates consist of a Ni-YSZ fuel electrode (active layer and support), a YSZ electrolyte, and a GDC diffusion barrier. The active area of the air electrodes is 1.3 cm$^2$ (button cells) and 16 cm$^2$ (square cells). All screen-printed air electrodes—either single-phase, composite, or with a current collector—are sintered (or co-sintered) for 2 h at 1050°C with heating rates of 5 K min$^{-1}$ and cooling rates of 2 K min$^{-1}$.

### 2.2 | Electrochemical Characterization

Symmetrical and full button cells with a diameter of 2 cm are characterized using a ProboStat system produced by Norwegian Electro Ceramics AS (NorECs) and a Novocontrol Alpha-A frequency response analyzer with potentiostat/galvanostat interface (Novocontrol POT/GAL 15 V/10 A). Electrochemical impedance spectroscopy (EIS) is carried out in a four-wire setup, with frequencies ranging logarithmically in 71 steps from 1 MHz to 100 mHz and 50 mV (rms) amplitude. The inductance of the test setup ($L_0$) was subtracted from all impedance spectra presented in this work.

In the case of the symmetrical cells, no dedicated sealing is used, and the gas flow on both sides is equal. For the full button cells, sealing between the air and fuel electrode compartments is established by means of gold gaskets. Electrical contacts on the air electrode side are accomplished by using Au-mesh without any additional metallic pastes. Ni-mesh and Ni-paste are employed

for contacting the fuel electrode side. Heating and cooling rates at the start and end of the cell tests are set to 2 K min⁻¹. For SOEC testing, the fuel gas is humidified using a Humistat provided by NorECs. Some tests were performed using gas flow variations, as described in Section 3.1. The maximum flow rates are 100 mL min⁻¹ at the fuel electrode side and 500 mL min⁻¹ at the air electrode side.

Characterization of the $5 \times 5$ cm² cells is carried out using an Evaluator C50-HT test stand from Horiba FuelCon GmbH. The cells are fixed onto a polished alumina frame with a ceramic housing placed on top of their edges. A mechanical load of 0.5 kg is applied in order to achieve gas tightness and reduce contact resistance. Ni- and Pt-meshes are used as electrical contacts on the fuel and air electrode side, respectively. No additional metallic contact pastes are used. Heating and cooling rates are set to 1 K min⁻¹, with gas flows adjusted according to the specific test protocol (see Section 3). All current–voltage curves are recorded at a rate of 3 mA cm⁻² s⁻¹. Impedance spectra are acquired from 100 kHz to 100 mHz, the amplitude being automatically adjusted by the measurement software (TestWork). All Nyquist plots shown in Section 3 are redrawn in the Supporting Information with equal scaling for the $x$- and $y$-axes (Figures S-1–S-4).

## 2.3 | Microstructural and Chemical Characterization

Cell microstructures are examined using a ZEISS 450 GeminiSEM field emission scanning electron microscope (FESEM), both in backscattered electron (BSE) and secondary electron (SE) modes, operating at 5 kV and 3 nA. To create specimen cross sections, the cells undergo sectioning with a diamond wire saw and subsequent treatment with a Hitachi IM400Plus ion slicer. A thin layer of gold is sputtered onto the samples to avoid charging. The distribution of chemical elements is analyzed using energy dispersive X-ray spectroscopy (EDX) with an Ultim Extreme detector from Oxford Instruments, covering an energy range of 0–10 keV. The voltage range is selected to provide sufficient element detection.

## 3 | Results and Discussion

## 3.1 | Electrochemical Characterization of Button Cells

### 3.1.1 | Symmetrical Button Cells

Symmetrical cells with two equal air electrodes on both sides of the GDC substrates are used to characterize ohmic and polarization resistances of various electrode configurations by EIS at 800°C. All spectra are fitted with the equivalent circuit $(L_0 + R_s) + R_1||CPE_1 + R_2||CPE_2$, where $L_0$ represents the inductance of the test setup, $R_i$ is ohmic resistances, and $CPE_i$ refers to constant phase elements used to model non-ideal capacitances [25]. No bias current is applied during the measurements. In order to reduce concentration polarization effects due to gas limitation, a flow of 20% $O_2$/Ar is established at 100 mL min⁻¹.

Figure 1a shows impedance spectra of symmetrical cells with different electrode configurations. In this diagram, $L_0$ as well as

the ohmic resistance of the GDC substrates (calculated from the cell geometry and a conductivity value of 0.07 S cm⁻¹ at 800°C for GDC, as determined by a separate measurement) are subtracted from the data. Moreover, the values are divided by two in order to display the average contribution of a single air electrode.

It is suggested that the high-frequency semicircle ($R_1||CPE_1$) is caused by the charge transfer of oxygen ions and the double layer capacitance at the electrode–electrolyte interface. The main contribution to the midfrequency arc ($R_2||CPE_2$) corresponds to the actual electrode reaction, consisting of a series of elementary steps such as adsorption of molecular oxygen on the electrode surface, oxygen dissociation, reduction, and incorporation into the crystal lattice as well as bulk diffusion of oxygen toward the electrolyte. It is further assumed that $R_s$ is caused by the ionic resistivity of GDC and an additional ohmic contribution from the air electrodes.

Figure 1b shows values of $R_{ohmic}$, which are calculated from $R_s$ by subtracting the ohmic contribution of the GDC electrolyte. $R_p$ represents the average polarization resistance of a single electrode, that is, $(R_1 + R_2)/2$, according to the equivalent circuit stated above.

Regarding the symmetrical cells without CCL, Figure 1b shows that increasing the LNF–LPNSSF ratio in the composite layer significantly reduces the ohmic resistance, leading to a decrease in $R_{ohmic}$ from 1.08 Ω cm² (0% LNF) to 0.02 Ω cm² (50% LNF). This effect is most likely due to the high electronic conductivity of LNF compared to that of LPNSSF. The polarization resistance increases with increasing the LNF content in the composite, from 0.15 Ω cm² (25% LNF) to 0.23 Ω cm² (50% LNF). This is as expected, as LNF is known to possess rather small oxygen deficiencies and thus a low ionic conductivity of oxygen [26]. These results show that among the investigated compositions, the composite air electrode with 50 wt.% LPNSSF yields the lowest overall (i.e., $R_{ohmic} + R_p$) electrode resistance.

The best electrode performance, however, both in terms of $R_{ohmic}$ and $R_p$ (0.01 and 0.12 Ω cm², respectively), is obtained when a single-phase LPNSSF air electrode is combined with an additional LNF CCL.

### 3.1.2 | Full Button Cells

Based on the results obtained for symmetrical cells, several air electrode compositions are investigated on full cells at the button cell level. Serving as a reference cell, the electrochemical performance of a button cell with single-phase LPNSSF air electrode (i.e., LPNSSF|GDC|YSZ|Ni-YSZ) is evaluated in SOFC mode at different temperatures (Figure 2). High gas flow rates of 0.5 L min⁻¹ 20% $O_2$ (rest Ar) at the air electrode side and 100 mL min⁻¹ $H_2$ at the fuel electrode side are used in order to reduce concentration polarization effects. The current densities at 0.7 V are 0.55, 0.50, 0.40, and 0.29 A cm⁻² at 800°C, 750°C, 700°C, and 650°C, respectively.

Figure 3 shows impedance spectra acquired on a full button cell with single-phase LPNSSF air electrode. The curves are recorded 100 mV below OCV in order to avoid electrolysis operation during
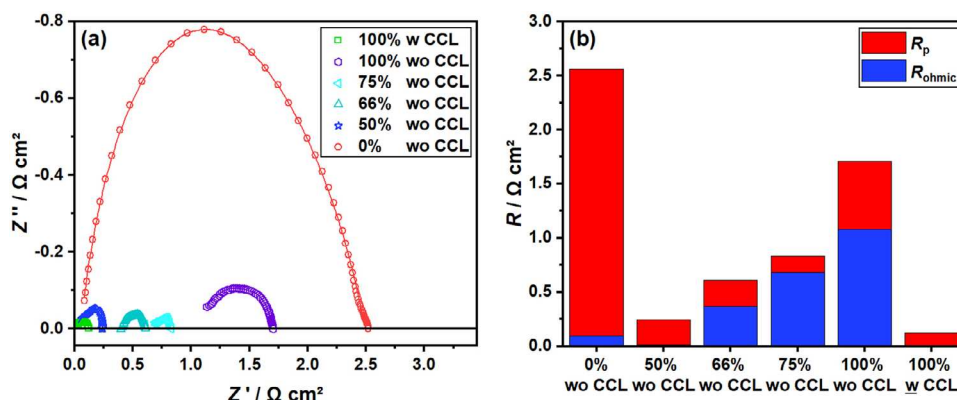
**FIGURE 1** | Impedance spectra of the symmetrical cells with GDC electrolyte and LPNSSF–LNF composite air electrodes with (w) and without (wo) LNF current collector (CCL) at 800°C (a) and $R_{ohmic}$ as well as $R_p$ shown as bar chart (b). Percentages given in the diagrams refer to the LPNSSF content (wt.%) of the composite electrodes. Gas flow is 100 mL min$^{-1}$ 20% $O_2$ (rest Ar) in all cases. Lines in (a) are least-squares fits using the equivalent circuit described in the text. The inductance of the setup as well as the resistance of the GDC electrolyte are subtracted, and the data are divided by two. GDC, $Ce_{0.9}Gd_{0.1}O_{1.95}$; LPNSSF, $La_{0.2}Pr_{0.2}Nd_{0.2}Sm_{0.2}Sr_{0.2}FeO_{3-\delta}$; LNF, $LaNi_{0.6}Fe_{0.4}O_{3-\delta}$.
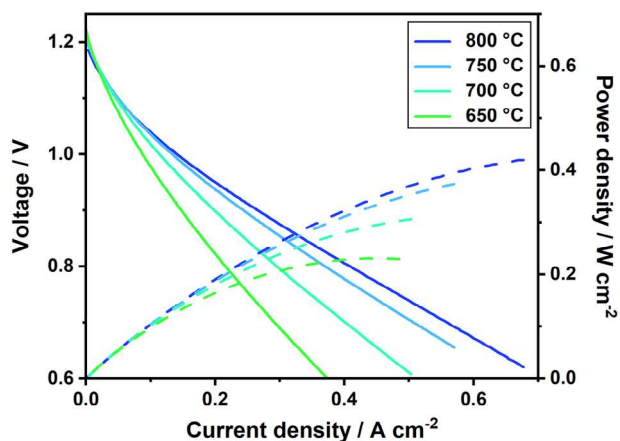


**FIGURE 2** | Voltage (solid lines) and power density (dashed lines) vs. current density of a full button cell with single-phase LPNSSF air electrode in SOFC mode at different temperatures. Flow rates are 500 mL min$^{-1}$ 20% $O_2$ (rest Ar) at the air electrode and 100 mL min$^{-1}$ $H_2$ at the fuel electrode. LPNSSF, $La_{0.2}Pr_{0.2}Nd_{0.2}Sm_{0.2}Sr_{0.2}FeO_{3-\delta}$; SOFC, solid oxide fuel cells.



**FIGURE 3** | Impedance spectra of a full button cell with single-phase LPNSSF air electrode recorded 100 mV below OCV at different temperatures. Flow rates are 500 mL min$^{-1}$ 20% $O_2$ (rest Ar) at the air electrode side and 100 mL min$^{-1}$ $H_2$ at the fuel electrode side. Lines are fits with the equivalent circuit model described in the text. LPNSSF, $La_{0.2}Pr_{0.2}Nd_{0.2}Sm_{0.2}Sr_{0.2}FeO_{3-\delta}$.

the impedance measurements. The spectra are fitted with the equivalent circuit $(L_0 + R_s) + R_1 \| CPE_1 + R_2 \| CPE_2$. Table 1 lists all parameters derived from least-squares fitting.

The resistance of the low-frequency arc ($R_2$) is around 0.15 $\Omega$ cm$^2$ and shows no thermal activation. This semicircle could be related to gas transport processes at the electrodes, which are characterized by a weak temperature dependence [27–29]. $R_s$ accounts for approximately 50% of the total cell resistance and thus plays a significant role in the limited electrochemical performance of cells with single-phase LPNSSF air electrode. Because the low electronic conductivity of LPNSSF is expected to be a major contributing factor to $R_s$, two different approaches are pursued in this work to improve the electrochemical performance of the air electrode. As suggested by the results of the symmetrical cell tests, the application of an additional LNF CCL, or the use of a
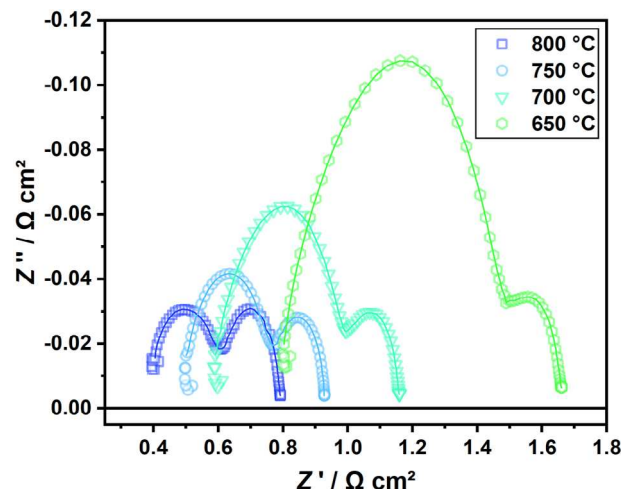
50 wt.% LPNSSF—50 wt.% LNF composite electrode, should be promising ways to enhance the electrode performance.

Current–voltage curves of full button cells with different air electrode configurations are shown in Figure 4 for both SOEC and SOFC operations. As in all previous tests, no metallic contact pastes are used on the air electrode side. In SOFC mode, the cell with a 50% LPNSSF–50% LNF composite air electrode without CCL achieves a current density of 0.61 A cm$^{-2}$ at 0.7 V and 800°C, which corresponds to a performance increase of approximately 10% compared to the single-phase LPNSSF electrode without CCL (0.55 A cm$^{-2}$). The improvement in cell performance is less significant in electrolysis mode, where the cell with composite air electrode reaches −0.39 A cm$^{-2}$ at 1.2 V, whereas single-phase LPNSSF achieves −0.37 A cm$^{-2}$ at the same voltage. The cell with a single-phase LPNSSF air electrode and an additional

**TABLE 1** | Parameters obtained from fits to the impedance spectra in Figure 3 of a full button cell with single-phase $La_{0.2}Pr_{0.2}Nd_{0.2}Sm_{0.2}Sr_{0.2}FeO_{3-\delta}$ (LPNSSF) air electrode.

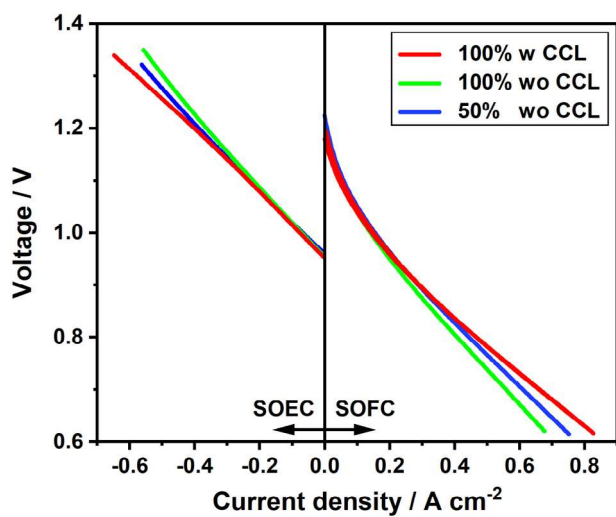| Temperature | 800°C | 750°C | 700°C | 650°C |
|---|---|---|---|---|
| $R_s/\Omega\ cm^2$ | 0.366 | 0.475 | 0.571 | 0.783 |
| $R_p/\Omega\ cm^2$ $(=R_1 + R_2)$ | 0.429 | 0.458 | 0.591 | 0.880 |
| $R_1/\Omega\ cm^2$ | 0.255 | 0.304 | 0.438 | 0.734 |
| $C_1/F\ cm^{-2}$ | 5.85E−05 | 7.19E−05 | 8.71E−05 | 9.78E−05 |
| $R_2/\Omega\ cm^2$ | 0.174 | 0.154 | 0.153 | 0.146 |
| $C_2/F\ cm^{-2}$ | 0.064 | 0.084 | 0.114 | 0.187 |



**FIGURE 4** | Current–voltage curves of full button cells in SOFC and SOEC modes with (w) and without (wo) a CCL at 800°C. Percentages given in the legend refer to the LPNSSF weight fractions of the air electrode (the remainder is LNF). In SOFC mode, gas flows are 500 mL min$^{-1}$ 20% $O_2$ (rest Ar) at the air electrode and 100 mL min$^{-1}$ $H_2$ at the fuel electrode. In SOEC mode, gas flows are 40 mL min$^{-1}$ 20% $O_2$ (rest Ar) at the air electrode and 40 mL min$^{-1}$ $H_2$ with 50 vol.% $H_2O$ at the fuel electrode. CCL, current collector layer; LPNSSF, $La_{0.2}Pr_{0.2}Nd_{0.2}Sm_{0.2}Sr_{0.2}FeO_{3-\delta}$; LNF, $LaNi_{0.6}Fe_{0.4}O_{3-\delta}$; SOEC, solid oxide electrolysis cells; SOFC, solid oxide fuel cells.

LNF CCL reaches 0.66 A cm$^{-2}$ at 0.7 V, which is approximately 20% higher compared to the LPNSSF electrode without CCL. In SOEC mode, the current density is −0.40 A cm$^{-2}$ at 1.2 V for the cell with the LPNSSF electrode with CCL, which corresponds to approximately 8% increase compared to the performance without a CCL.

Impedance spectra of the full button cells acquired at 0.7 V in SOFC mode and 1.2 V in SOEC mode are shown in Figure 5. For these and all subsequent EIS spectra, an equivalent circuit with 2 or 3 R‖CPE elements is used to model the electrode polarization. All parameters derived from least-squares fitting are collected in Table 2.

Regarding the ohmic resistances $R_s$, it is evident from Figure 5a (SOFC mode) that cells with an LPNSSF–LNF composite electrode (0.33 Ω cm$^2$) and a single-phase LPNSSF electrode with LNF

CCL (0.22 Ω cm$^2$) exhibit lower values of $R_s$ than the single-phase LPNSSF air electrode without CCL (0.40 Ω cm$^2$). The polarization resistance $R_p$ is almost the same for cells with single-phase LPNSSF and LPNSSF–LNF composite electrodes (0.27 Ω cm$^2$), but slightly higher for the cell with the single-phase LPNSSF electrode with CCL (0.29 Ω cm$^2$). In SOEC mode (see Figure 5b), similar trends regarding $R_s$ and $R_p$ are found.

In Figure 5a,b, a semicircle consistently occurs in the low-frequency region of the impedance spectra. The corresponding capacitances are similar to values obtained for the button cell with single-phase LPNSSF air electrode (see Figure 3) and are thus ascribed to gas diffusion and gas transport processes at the air and/or fuel electrodes [28, 29], as discussed above. In order to corroborate this interpretation and to localize these processes, the gas flow at the air electrode is varied for cells with and without CCL, and the impact on the impedance spectra is studied. Impedance spectra recorded in SOFC mode at 0.7 V and 800°C are shown in Figure 6a for 20% $O_2$/Ar flows of 100, 50, and 33 mL min$^{-1}$, whereas the fuel flow is kept constant at 40 mL min$^{-1}$ $H_2$. Consistent with the results obtained in SOFC mode under high air flow (see Figure 5a), the performance of the cell with single-phase LPNSSF electrode and an additional LNF CCL is superior to that of the LPNSSF–LNF composite without CCL, which is mostly due to the lower $R_s$ (case (1) in Figure 6a). However, when reducing the air flow, the resistance $R_3$ of the low-frequency arc increases strongly (cases (2) and (3) in Figure 6a), indicating that it is dominated by processes at the air electrode. All parameters derived from fitting are collected in Table 3. A comparison of the $R_3$ values determined from the impedance spectra (Figure 6b) shows that the increase in $R_3$ is more pronounced for the cell with a current collector, suggesting insufficient permeability of the porous CCL for air. Therefore, in an attempt to further optimize the microstructure of the air electrode, a coarser LNF powder is used for the preparation of the current collector, which is expected to improve gas transport through the CCL to the active electrode (see Section 3.2).

Post-test FESEM−BSE cross-section images of button cells with the three tested air electrode configurations are shown in Figure 7. All air electrodes feature a homogeneous active layer with a thickness of ∼25 μm. In the case of the cell with the single-phase LPNSSF electrode with current collector, the CCL adds an additional 6 μm to the electrode thickness. The LPNSSF layers have a very fine microstructure, with primary particles having a diameter below 100 nm. The porosity of the single-phase LPNSSF
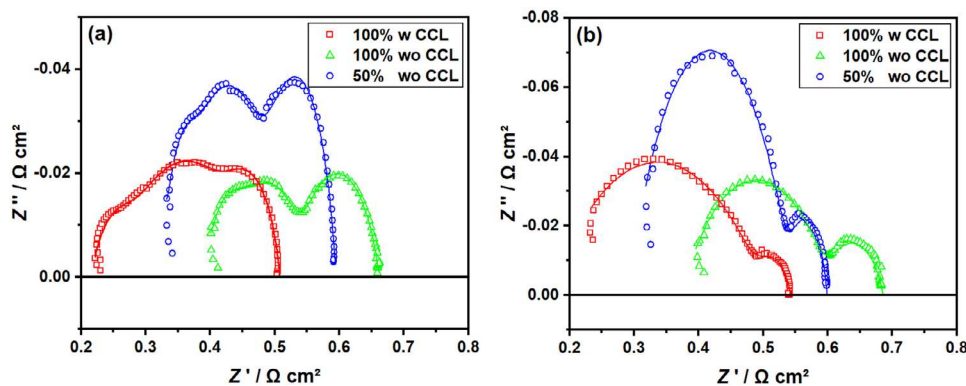
**FIGURE 5** | Impedance spectra of full button cells with (w) and without (wo) a CCL at 0.7 V in SOFC (a) and 1.2 V in SOEC mode (b) at 800°C. Percentages given in the legend refer to the LPNSSF weight fraction of the air electrode (the remainder is LNF). In SOFC mode (a), gas flows are 500 mL min$^{-1}$ 20% $O_2$ (rest Ar) at the air electrode and 100 mL min$^{-1}$ $H_2$ at the fuel electrode. In SOEC mode (b), gas flows are 40 mL min$^{-1}$ 20% $O_2$ (rest Ar) at the air electrode and 40 mL min$^{-1}$ $H_2$ with 50 vol.% $H_2O$ at the fuel electrode. Lines are fits with the equivalent circuit model described in the text. CCL, current collector layer; LPNSSF, La$_{0.2}$Pr$_{0.2}$Nd$_{0.2}$Sm$_{0.2}$Sr$_{0.2}$FeO$_{3-\delta}$; LNF, LaNi$_{0.6}$Fe$_{0.4}$O$_{3-\delta}$; SOEC, solid oxide electrolysis cells; SOFC, solid oxide fuel cells.

**TABLE 2** | Parameters obtained from least-squares fits to the impedance spectra in Figure 5 of full button cells with different air electrodes.

| Air electrode | 100% w CCL | 100% wo CCL | 50% wo CCL | 100% w CCL | 100% wo CCL | 50% wo CCL |
|---|---|---|---|---|---|---|
| Operation | | SOFC @ 0.7 V | | | SOEC @ 1.2 V | |
| $R_s$/$\Omega$ cm$^2$ | 0.216 | 0.396 | 0.328 | 0.173 | 0.376 | 0.293 |
| $R_p$/$\Omega$ cm$^2$ | 0.294 | 0.267 | 0.268 | 0.388 | 0.310 | 0.306 |
| ($=R_1 + R_2 + R_3$) | | | | | | |
| $R_1$/$\Omega$ cm$^2$ | 0.060 | 0.043 | 0.038 | 0.329 | 0.223 | 0.247 |
| $C_1$/F cm$^{-2}$ | 1.55E$-$4 | 8.16E$-$05 | 1.15E$-$04 | 2.05E$-$05 | 3.68E$-$05 | 2.99E$-$05 |
| $R_2$/$\Omega$ cm$^2$ | 0.170 | 0.101 | 0.124 | — | — | — |
| $C_2$/F cm$^{-2}$ | 6.46E$-$03 | 5.13E$-$04 | 9.28E$-$04 | — | — | — |
| $R_3$/$\Omega$ cm$^2$ | 0.064 | 0.123 | 0.106 | 0.059 | 0.087 | 0.059 |
| $C_3$/F cm$^{-2}$ | 0.709 | 0.108 | 0.157 | 0.116 | 0.064 | 0.114 |

*Note*: Percentages refer to the LPNSSF weight fraction of the air electrode (the remainder is LNF) with (w) or without (wo) LNF CCL.

Abbreviations: CCL, current collector layer; LNF, LaNi$_{0.6}$Fe$_{0.4}$O$_{3-\delta}$; LPNSSF, La$_{0.2}$Pr$_{0.2}$Nd$_{0.2}$Sm$_{0.2}$Sr$_{0.2}$FeO$_{3-\delta}$; SOECs, solid oxide electrolysis cells; SOFC, solid oxide fuel cell.
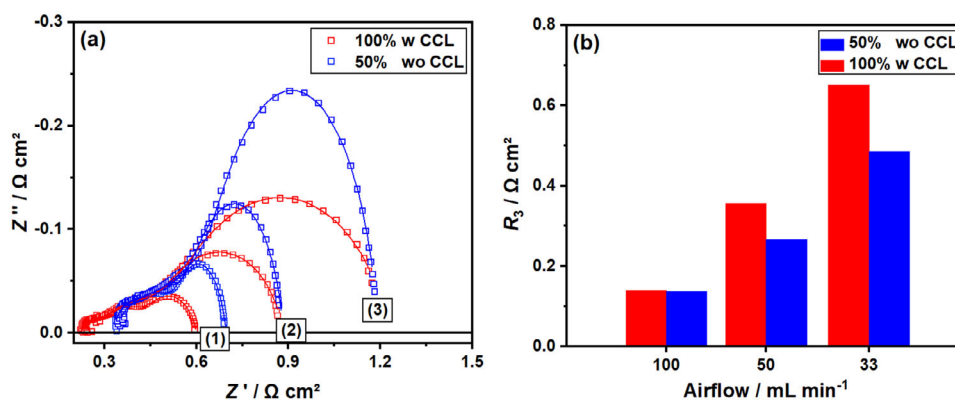


**FIGURE 6** | Impedance spectra of full button cells with single-phase (100%) LPNSSF air electrode with CCL and 50% LPNSSF–50% LNF composite electrode without CCL (a) and bar graph of $R_3$ as a function of the airflow (b). The spectra were acquired in SOFC mode at 0.7 V and 800°C for different air flows of 100 (1), 50 (2), and 33 (3) mL min$^{-1}$ (20% $O_2$, rest Ar). Fuel gas flow is 40 mL min$^{-1}$ $H_2$ in all cases. Lines are fits with the equivalent circuit model described in the text. CCL, current collector layer; LPNSSF, La$_{0.2}$Pr$_{0.2}$Nd$_{0.2}$Sm$_{0.2}$Sr$_{0.2}$FeO$_{3-\delta}$; LNF, LaNi$_{0.6}$Fe$_{0.4}$O$_{3-\delta}$; SOFC, solid oxide fuel cells.

**TABLE 3** | Parameters obtained from fits to the impedance spectra in Figure 6 of full button cells with different air electrodes.

| Air electrode | 100% w CCL | 50% wo CCL | 100% w CCL | 50% wo CCL | 100% w CCL | 50% wo CCL |
|---|---|---|---|---|---|---|
| Air flow/mL min$^{-1}$ | 100 | | 50 | | 33 | |
| $R_s/\Omega$ cm$^2$ | 0.218 | 0.326 | 0.218 | 0.319 | 0.229 | 0.330 |
| $R_p/\Omega$ cm$^2$ ($=R_1 + R_2 + R_3$) | 0.383 | 0.374 | 0.670 | 0.568 | 1.005 | 0.871 |
| $R_1/\Omega$ cm$^2$ | 0.060 | 0.029 | 0.050 | 0.123 | 0.053 | 0.137 |
| $C_1$/F cm$^{-2}$ | 1.58E−04 | 1.74E−04 | 1.68E−04 | 1.10E−04 | 1.61E−04 | 1.16E−04 |
| $R_2/\Omega$ cm$^2$ | 0.183 | 0.208 | 0.264 | 0.179 | 0.301 | 0.248 |
| $C_2$/F cm$^{-2}$ | 8.67E−03 | 2.01E−03 | 1.37E−02 | 1.94E−02 | 1.47E−02 | 3.62E−02 |
| $R_3/\Omega$ cm$^2$ | 0.140 | 0.137 | 0.356 | 0.266 | 0.651 | 0.486 |
| $C_3$/F cm$^{-2}$ | 0.619 | 0.494 | 0.827 | 0.642 | 0.796 | 0.701 |

*Note*: Percentages refer to the LPNSSF weight fraction of the air electrode (the remainder is LNF) with (w) or without (wo) LNF CCL.

Abbreviations: CCL, current collector layer; LNF, LaNi$_{0.6}$Fe$_{0.4}$O$_{3-\delta}$; LPNSSF, La$_{0.2}$Pr$_{0.2}$Nd$_{0.2}$Sm$_{0.2}$Sr$_{0.2}$FeO$_{3-\delta}$.
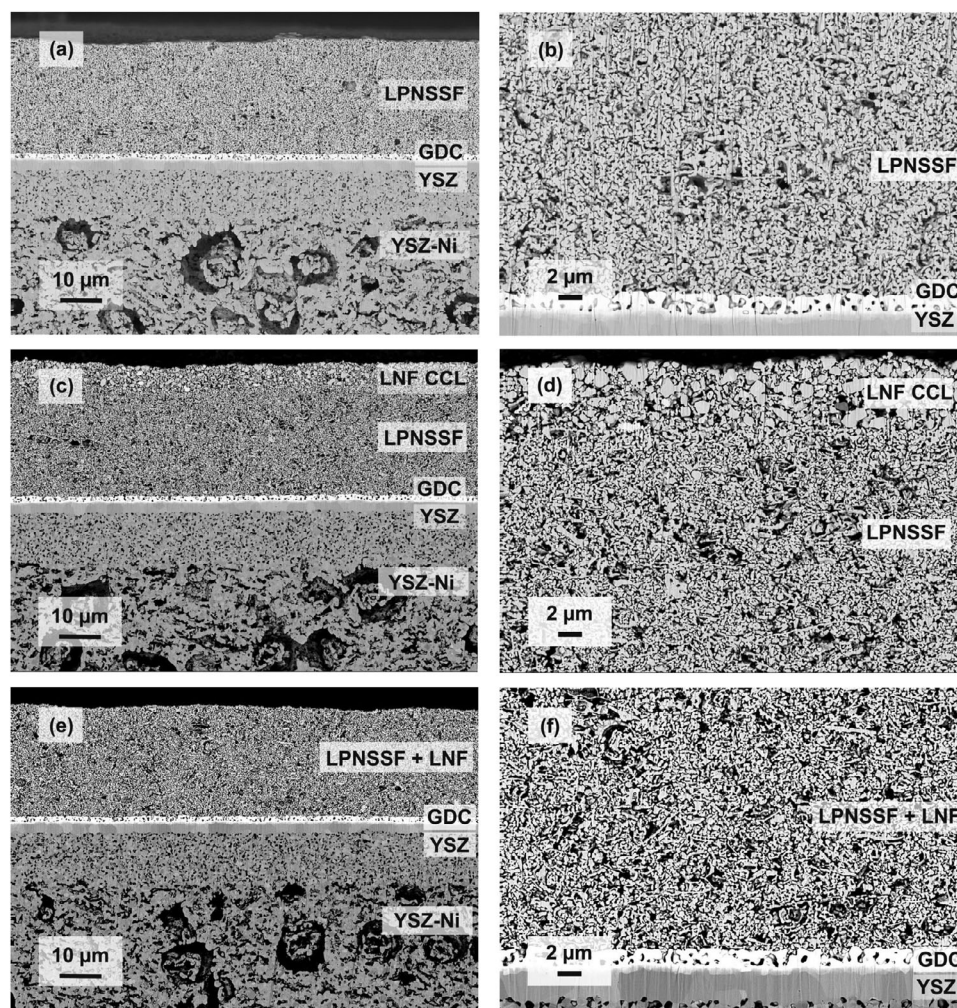


**FIGURE 7** | FESEM–BSE cross-section images of ASC button cells acquired at different magnifications. Cell with single-phase LPNSSF air electrode without CCL (a and b), LPNSSF electrode with CCL (c and d), and 50% LPNSSF–50% LNF composite electrode without CCL (e and f). ASC, anode-supported cell; BSE, backscattered electron; CCL, current collector layer; FESEM, field emission scanning electron microscope; GDC, Ce$_{0.9}$Gd$_{0.1}$O$_{1.95}$; LPNSSF, La$_{0.2}$Pr$_{0.2}$Nd$_{0.2}$Sm$_{0.2}$Sr$_{0.2}$FeO$_{3-\delta}$; LNF, LaNi$_{0.6}$Fe$_{0.4}$O$_{3-\delta}$.

air electrode, estimated by image analysis [30] of SEM cross sections, is ~36%. The LPNSSF–LNF composite electrode shows a porosity of ~33%, which is slightly lower than that of the single-phase electrode. The porosity of the LNF current collector has a rather low value of ~28%, which may limit the accessibility of the active electrode layer by the oxidant, which is consistent with the findings discussed above (cf. Figure 6). This is also in agreement with the literature, where it has been reported that a too dense CCL can limit oxygen gas transport toward the air electrode/electrolyte interface [31, 32].

The images confirm good adhesion among all adjacent layers. The GDC barriers seem rather porous (estimated approximately 20%), which would be expected to facilitate the formation of $SrZrO_3$ (SZO) [33] during electrode sintering. However, there are no indications of SZO formation in the FESEM–BSE images. Elemental maps obtained by EDX analysis of the LPNSSF air electrode/barrier layer interface are shown in Figure S-5 and confirm the absence of SZO. This is consistent with the literature, which reports that $La_{0.8}Sr_{0.2}FeO_{3-\delta}$ in direct contact with YSZ does not form SZO but rather incorporates $Zr^{4+}$ ions in the perovskite structure [34].

## 3.2 | Electrochemical Characterization of a $5 \times 5$ cm$^2$ Cell

Following the button cell tests, the best performing air electrode configuration (i.e., single-phase LPNSSF + LNF CCL) is transferred to a $5 \times 5$ cm$^2$ cell format with 16 cm$^2$ air electrode area. Based on the insights described in Section 3.1, LNF powder with a larger particle size of ~10 μm is used in a further optimization step in order to avoid gas transport limitations caused by a too dense CCL. The results of the electrochemical characterization are shown in Figure 8. In SOFC mode, the current density of the $5 \times 5$ cm$^2$ cell reaches a maximum of 0.96 A cm$^{-2}$ at 0.7 V and 800°C. In SOEC mode, a current density of −1.06 A cm$^{-2}$ is obtained at 1.2 V and 90 vol.% humidity (rest H$_2$). The essentially linear characteristics of the curves in SOEC mode indicate that mass transfer (diffusion) limitations play a subordinate role even at lower humidification levels.

A long-term test is performed for 1000 h under continuous polarization at −0.69 A cm$^{-2}$ in electrolysis mode with 80 vol.% humidification and a gas flow rate of 1 L min$^{-1}$ at the fuel electrode. During such long-term operation, SOCs typically face significant challenges in terms of the microstructural and chemical stability of the air electrode and the electrolyte [35–37]. In addition, the fuel electrode is prone to degradation due to the agglomeration and migration of nickel [38, 39].

According to Figure 9, the long-term behavior can be divided into two stages. The first stage is characterized by a nonlinear increase in cell voltage from 1.10 to 1.15 V during the initial 300 h, a typical behavior that has been described in the literature [40, 41]. In the second stage, especially from 500 h onward and at a cell voltage of ~1.16 V, the voltage increase becomes much weaker and more linear. This results in an average degradation rate of 10 mV kh$^{-1}$ or 0.8% kh$^{-1}$, taking the cell voltage at 500 h as a reference. Current–voltage curves for SOEC operation are displayed in Figure S-6 and show a constant OCV as well as a decrease in current density
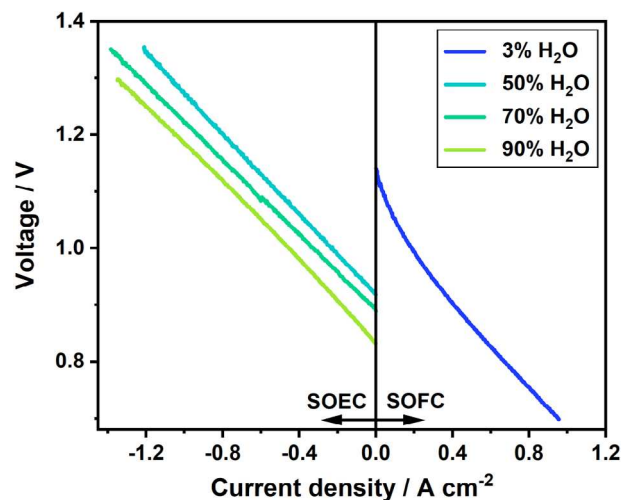


**FIGURE 8** | Current–voltage curves of a $5 \times 5$ cm$^2$ ASC with LPNSSF air electrode and LNF CCL in SOFC and SOEC modes at different humidification levels (rest H$_2$) at 800°C. The gas flow at the fuel electrode is 1 L min$^{-1}$. At the air electrode, the gas flow is 3 L min$^{-1}$ air in SOFC mode and 0.5 L min$^{-1}$ air in SOEC mode. ASC, anode-supported cell; CCL, current collector layer; LPNSSF, $La_{0.2}Pr_{0.2}Nd_{0.2}Sm_{0.2}Sr_{0.2}FeO_{3-\delta}$; LNF, $LaNi_{0.6}Fe_{0.4}O_{3-\delta}$; SOEC, solid oxide electrolysis cells; SOFC, solid oxide fuel cells.
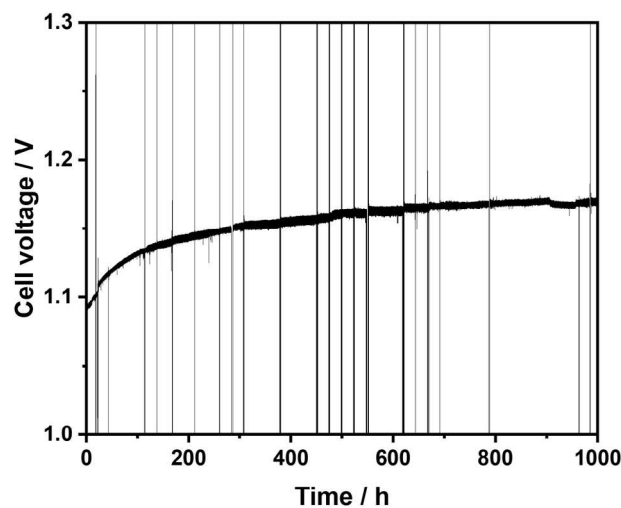


**FIGURE 9** | Cell voltage of a $5 \times 5$ cm$^2$ ASC with LPNSSF air electrode and LNF CCL during a long-term test in SOEC mode at 800°C with continuous polarization of −0.688 A cm$^{-2}$. Gas flows are 1 L min$^{-1}$ 80 vol.% H$_2$O (rest H$_2$) at the fuel electrode and 0.5 L min$^{-1}$ air at the air electrode. Vertical lines correspond to short interruptions in which current–voltage curves and impedance spectra are recorded. ASC, anode-supported cell; CCL, current collector layer; LPNSSF, $La_{0.2}Pr_{0.2}Nd_{0.2}Sm_{0.2}Sr_{0.2}FeO_{3-\delta}$; LNF, $LaNi_{0.6}Fe_{0.4}O_{3-\delta}$; SOEC, solid oxide electrolysis cells.

from −0.99 A cm$^{-2}$ (0 h) to −0.75 A cm$^{-2}$ (987 h) at 1.2 V over the testing period. Impedance spectra recorded at OCV from 100 kHz to 10 Hz are shown in Figure S-7. The increase in cell voltage in the first stage of the long-term test is mainly due to a process with an initial peak frequency around 1 kHz. During the first 450 h, the peak frequency shifts to approximately 100 Hz, where
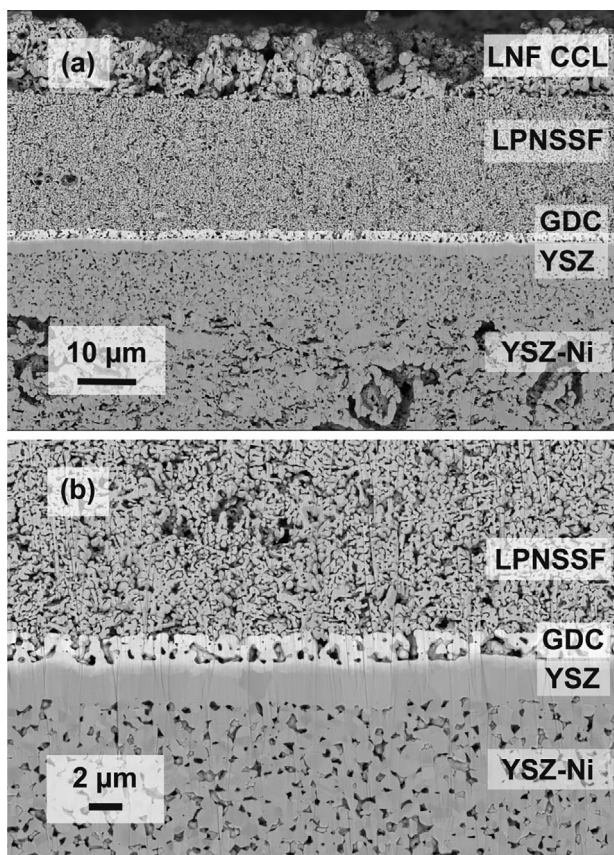
**FIGURE 10** | Post-test FESEM–BSE cross-section images of a $5 \times 5$ cm$^2$ ASC with LPNSSF air electrode and LNF CCL after 1000 h long-term polarization in SOEC mode acquired at different magnifications. ASC, anode-supported cell; BSE, backscattered electron; CCL, current collector layer; FESEM, field emission scanning electron microscope; LPNSSF, La$_{0.2}$Pr$_{0.2}$Nd$_{0.2}$Sm$_{0.2}$Sr$_{0.2}$FeO$_{3-\delta}$; LNF, LaNi$_{0.6}$Fe$_{0.4}$O$_{3-\delta}$; SOEC, solid oxide electrolysis cells.

it remains until the end of the test. The phenomenon of a marked increase in cell voltage at the start of long-term electrolysis is usually attributed to a reduction in triple phase boundaries of the fuel electrode. These occur due to a loss of contact between YSZ and Ni particles as well as Ni migration at high steam content [39, 42, 43]. The spectra also indicate that there appears to be a small but steady increase in the ohmic resistance, which, together with progressive fuel electrode degradation, could be the main reason for the cell degradation in the second stage ($t \geq 500$ h) [40].

A comparison between FESEM images of the pristine cell (Figures S-8 and S-9a) and the tested cell (Figure 10 and Figure S-9b) shows that the porosity of the GDC diffusion barrier increases from ~20% (fresh state) to ~36% (after 1000 h test). This increase in porosity may contribute to the slight increase in $R_s$ observed during testing (see Figure S-7) [44]. A similar increase in the porosity of the GDC barrier after a long-term electrolysis test has also been observed in a previous study [17]. The increase in porosity of the barrier layer may be related to a mechanism suggested by Knibbe et al. [45], who observed the formation of pores within the electrolyte close to the air electrode at high current densities in SOEC mode. With respect to the air electrode, no microstructural degradation can be discerned after

the 1000 h test. In addition, there is good adhesion between all layers, indicating that the GDC/air electrode interface remains intact during the long-term operation.

The CCL has a rather nonuniform thickness of ~10 μm and displays a very open and porous structure compared to the denser CCL of the button cells (cf. Figure 7d). This is expected to afford an easier exchange of oxygen between the air electrode and the ambient gas atmosphere while maintaining efficient current collection, which may explain the strong improvement in cell performance.

Figure S-10 shows elemental maps of the tested cell. There is no evidence of SZO formation at the GDC/YSZ or LPNSSF/GDC interfaces. As ambient air was used for the cell test, another potential issue might be sulfur poisoning of the air electrode. This would manifest itself by the formation of SrSO$_4$ within the air electrode due to a reaction of SO$_2$ with strontium from the electrode layer [17, 46, 47]. Because the LNF current collector covers the air electrode, sulfur poisoning is impossible to detect in top view but could be determined from sections across the cell. However, no evidence of sulfur is found by EDX mapping of the electrode cross section (results not shown). This indicates that either the LNF layer protects the air electrode surface or the LPNSSF structure is more resistant to sulfur poisoning than other perovskite materials [17, 46, 48].

## 4 | Conclusions

The cobalt-free HEP LPNSSF is successfully synthesized and characterized as air electrode in SOCs. On the button cell level, a current density of 0.55 A cm$^{-2}$ is achieved for a cell with single-phase LPNSSF air electrode at 0.7 V and 800°C in fuel cell mode. Symmetrical cell tests demonstrate that the cell performance can be enhanced by the good electronic conductor LNF, either by using an LPNSSF–LNF composite electrode or by applying an additional LNF CCL. The best performance is achieved when a single-phase LPNSSF electrode with LNF CCL is used. This results in an increase in current density of approximately 20% in SOFC operation mode, whereas the improvement is less pronounced in electrolysis mode. In both cases, the effect is almost entirely due to a significant decrease in the ohmic resistance of the cells, indicating that the moderate electronic conductivity of LPNSSF could limit the current density of cells when used as a single-phase air electrode. Moreover, impedance spectroscopy and SEM analyses show that a non-optimized microstructure of the current collector can block gas transport to the active electrode layer and thus limit cell performance.

Drawing on the results from the button cell tests, an optimized $5 \times 5$ cm$^2$ cell with single-phase LPNSSF air electrode and LNF CCL is prepared, which shows a significant improvement in cell performance, reaching 0.96 A cm$^{-2}$ at 0.7 V and 800°C in fuel cell mode. A long-term test with continuous polarization of $-0.69$ A cm$^{-2}$ in electrolysis mode is performed for 1000 h at 80% humidification. After an initial run-in period, the cell voltage increases at a relatively low rate of 0.8% per 1000 h. SEM images indicate that an increase in porosity of the GDC barrier layer may be one factor contributing to the observed degradation behavior.

In summary, LPNSSF shows promising electrochemical performance and good long-term stability as a sustainable cobalt-free SOC air electrode when special attention is paid to mitigate effects caused by the limited electronic conductivity of the ferrite by ensuring adequate current collection in a more optimized electrode design.

## Data Availability Statement

The data that support the findings of this study are available from the corresponding author upon reasonable request.

## References

1. M. El-Shafie, "Hydrogen Production by Water Electrolysis Technologies: A Review," *Results in Engineering* 20 (2023): 101426.

2. D. Ferrero, A. Lanzini, M. Santarelli, and P. Leone, "A Comparative Assessment on Hydrogen Production From Low- and High-Temperature Electrolysis," *International Journal of Hydrogen Energy* 38 (2013): 3523–3536.

3. M. Mohebali Nejadian, P. Ahmadi, and E. Houshfar, "Comparative Optimization Study of Three Novel Integrated Hydrogen Production Systems With SOEC, PEM, and Alkaline Electrolyzer," *Fuel* 336 (2023): 126835.

4. V. Venkataraman, M. Pérez-Fortes, L. Wang, et al., "Reversible Solid Oxide Systems for Energy and Chemical Applications—Review & Perspectives," *Journal of Energy Storage* 24 (2019): 100782.

5. Y. Zheng, Q. Li, T. Chen, C. Xu, and W. G. Wang, "Quantitative Contribution of Resistance Sources of Components to Stack Performance for Solid Oxide Electrolysis Cells," *Journal of Power Sources* 274 (2015): 736–740.

6. S. E. Wolf, F. E. Winterhalder, V. Vibhu, et al., "Solid Oxide Electrolysis Cells—Current Material Development and Industrial Application," *Journal of Materials Chemistry A* 11 (2023): 17977–18028.

7. A. H. Tkaczyk, A. Bartl, A. Amato, V. Lapkovskis, and M. Petranikova, "Sustainability Evaluation of Essential Critical Raw Materials: Cobalt, Niobium, Tungsten and Rare Earth Elements," *Journal of Physics D: Applied Physics* 51 (2018): 203001.

8. S. Akkurt, C. Sindiraç, T. Özmen Egesoy, and E. Erğen, "A Review on New Cobalt-Free Cathode Materials for Reversible Solid Oxide Fuel Cells," *Journal of Metals, Materials and Minerals* 33 (2023): 1654.

9. N. A. Baharuddin, A. Muchtar, and M. R. Somalu, "Short Review on Cobalt-Free Cathodes for Solid Oxide Fuel Cells," *International Journal of Hydrogen Energy* 42 (2017): 9149–9155.

10. Z. Han, J. Bai, X. Chen, X. Zhu, and D. Zhou, "Novel Cobalt-Free $Pr_2Ni_{1-x}Nb_xO_4$ ($x$ = 0, 0.05, 0.10, and 0.15) Perovskite as the Cathode Material for IT-SOFC," *International Journal of Hydrogen Energy* 46 (2021): 11894–11907.

11. S. S. Hashim, F. Liang, W. Zhou, and J. Sunarso, "Cobalt-Free Perovskite Cathodes for Solid Oxide Fuel Cells," *ChemElectroChem* 6 (2019): 3549–3569.

12. L. Zhao, B. He, X. Zhang, R. Peng, G. Meng, and X. Liu, "Electrochemical Performance of Novel Cobalt-Free Oxide $Ba_{0.5}Sr_{0.5}Fe_{0.8}Cu_{0.2}O_{3-\delta}$ for Solid Oxide Fuel Cell Cathode," *Journal of Power Sources* 195 (2010): 1859–1861.

13. H. Ullmann, N. Trofimenko, F. Tietz, D. Stöver, and A. Ahmad-Khanlou, "Correlation Between Thermal Expansion and Oxide Ion Transport in Mixed Conducting Perovskite-Type Oxides for SOFC Cathodes," *Solid State Ionics* 138 (2000): 79–90.

14. A. Sarkar, Q. Wang, A. Schiele, et al., "High-Entropy Oxides: Fundamental Aspects and Electrochemical Properties," *Advanced Materials* 31 (2019): 1806236.

15. X. Li, C. Shi, G. Zhang, et al., "A Medium-Entropy Perovskite Oxide $La_{0.7}Sr_{0.3}Co_{0.25}Fe_{0.25}Ni_{0.25}Mn_{0.25}O_{3-\delta}$ as Intermediate Temperature Solid Oxide Fuel Cells Cathode Material," *Ceramics International* 49 (2023): 30187–30195.

16. H. Xu, L. Dang, J. Yan, F. Wan, and W. Gong, "A New $(La_{0.2}Nd_{0.2}Gd_{0.2}Sr_{0.2}Ba_{0.2})Co_{0.2}Fe_{0.8}O_{3-\delta}$ High-Entropy Oxide Cathode for Intermediate Temperature Solid Oxide Fuel Cell," *Solid State Ionics* 397 (2023): 116233.

17. P. Pretschuh, A. Egger, R. Brunner, and E. Bucher, "Electrochemical and Microstructural Characterization of the High-Entropy Perovskite $La_{0.2}Pr_{0.2}Nd_{0.2}Sm_{0.2}Sr_{0.2}CoO_{3-\delta}$ for Solid Oxide Cell Air Electrodes," *Fuel Cells* 23 (2023): 377–386.

18. E. V. Tsipis and V. V. Kharton, "Electrode Materials and Reaction Mechanisms in Solid Oxide Fuel Cells: A Brief Review," *Journal of Solid State Electrochemistry* 12 (2008): 1367–1391.

19. S. P. Jiang, "Development of Lanthanum Strontium Cobalt Ferrite Perovskite Electrodes of Solid Oxide Fuel Cells—A Review," *International Journal of Hydrogen Energy* 44 (2019): 7448–7493.

20. A. Ndubuisi, S. Abouali, K. Singh, and V. Thangadurai, "Recent Advances, Practical Challenges, and Perspectives of Intermediate Temperature Solid Oxide Fuel Cell Cathodes," *Journal of Materials Chemistry A* 10 (2022): 2196–2227.

21. A. Julian, E. Juste, P. M. Geffroy, et al., "Thermal Behaviour of $La_{0.8}Sr_{0.2}Fe_{1-x}Ga_xO_{3-\delta}$ (x=0 or x=0.3)," *Journal of the European Ceramic Society* 29 (2009): 2603–2610.

22. C. Sun, R. Hui, and J. Roller, "Cathode Materials for Solid Oxide Fuel Cells: A Review," *Journal of Solid State Electrochemistry* 14 (2010): 1125–1144.

23. R. Chiba, F. Yoshimura, and Y. Sakurai, "An Investigation of $LaNi_{1-x}Fe_xO_3$ as a Cathode Material for Solid Oxide Fuel Cells," *Solid State Ionics* 124 (1999): 281–288.

24. L. A. Chick, L. R. Pederson, G. D. Maupin, J. L. Bates, L. E. Thomas, and G. J. Exarhos, "Glycine-Nitrate Combustion Synthesis of Oxide Ceramic Powders," *Materials Letters* 10 (1990): 6–12.

25. M. R. Shoar Abouzari, F. Berkemeier, G. Schmitz, and D. Wilmer, "On the Physical Interpretation of Constant Phase Elements," *Solid State Ionics* 180 (2009): 922–927.

26. M. Nishi, T. Horita, K. Yamaji, et al., "Oxide Ion Conductivity of $LaNi_{0.6}Fe_{0.4}O_3$," *ECS Transactions* 45 (2012): 171.

27. S. Kim, D. W. Joh, D.-Y. Lee, et al., "Microstructure Tailoring of Solid Oxide Electrolysis Cell Air Electrode to Boost Performance and Long-Term Durability," *Chemical Engineering Journal* 410 (2021): 128318.

28. J. Zhang, L. Lei, H. Li, K. Sun, Z. Sun, and M. Han, "Experimental Investigations of Cell Resistances to Characterize the Concentration Polarization Behavior of $10 \times 10$ cm$^2$ Solid Oxide Fuel Cells," *Journal of Power Sources* 516 (2021): 230678.

29. Y. Fu, Y. Jiang, S. Poizeau, et al., "Multicomponent Gas Diffusion in Porous Electrodes," *Journal of the Electrochemical Society* 162 (2015): F613.

30. C. A. Schneider, W. S. Rasband, and K. W. Eliceiri, "NIH Image to ImageJ: 25 Years of Image Analysis," *Nature Methods* 9 (2012): 671–675.

31. V. A. C. Haanappel, J. Mertens, D. Rutenbeck, et al., "Optimisation of Processing and Microstructural Parameters of LSM Cathodes to Improve the Electrochemical Performance of Anode-Supported SOFCs," *Journal of Power Sources* 141 (2005): 216–226.

32. M. Kusnezoff, N. Trofimenko, M. Müller, and A. Michaelis, "Influence of Electrode Design and Contacting Layers on Performance of Electrolyte Supported SOFC/SOEC Single Cells," *Materials* 9 (2016): 906.

33. M. Z. Khan, R.-H. Song, M. T. Mehran, S.-B. Lee, and T.-H. Lim, "Controlling Cation Migration and Inter-Diffusion Across Cathode/Interlayer/Electrolyte Interfaces of Solid Oxide Fuel Cells: A Review," *Ceramics International* 47 (2021): 5839–5869.

34. S. P. Simner, J. P. Shelton, M. D. Anderson, and J. W. Stevenson, "Interaction Between La(Sr)FeO$_3$ SOFC Cathode and YSZ Electrolyte," *Solid State Ionics* 161 (2003): 11–18.

35. K. Chen and S. P. Jiang, "Surface Segregation in Solid Oxide Cell Oxygen Electrodes: Phenomena, Mitigation Strategies and Electrochemical Properties," *Electrochemical Energy Reviews* 3 (2020): 730–765.

36. M. Keane, M. K. Mahapatra, A. Verma, and P. Singh, "LSM–YSZ Interactions and Anode Delamination in Solid Oxide Electrolysis Cells," *International Journal of Hydrogen Energy* 37 (2012): 16776–16785.

37. M. Nerat and Đ. Juričić, "Modelling of Anode Delamination in Solid Oxide Electrolysis Cell and Analysis of Its Effects on Electrochemical Performance," *International Journal of Hydrogen Energy* 43 (2018): 8179–8189.

38. Q. Fu, C. Tian, L. Hun, et al., "Ni Agglomeration and Performance Degradation of Solid Oxide Fuel Cell: A Model-Based Quantitative Study and Microstructure Optimization," *Energy* 289 (2024): 129997.

39. Y. Wang, C. Wu, B. Zu, et al., "Ni Migration of Ni-YSZ Electrode in Solid Oxide Electrolysis Cell: An Integrated Model Study," *Journal of Power Sources* 516 (2021): 230660.

40. X. Sun, P. V. Hendriksen, M. B. Mogensen, and M. Chen, "Degradation in Solid Oxide Electrolysis Cells During Long Term Testing," *Fuel Cells* 19 (2019): 740–747.

41. Y. Wang, W. Li, L. Ma, W. Li, and X. Liu, "Degradation of Solid Oxide Electrolysis Cells: Phenomena, Mechanisms, and Emerging Mitigation Strategies—A Review," *Journal of Materials Science & Technology* 55 (2020): 35–55.

42. M. B. Mogensen, A. Hauch, X. Sun, et al., "Relation Between Ni Particle Shape Change and Ni Migration in Ni–YSZ Electrodes—A Hypothesis," *Fuel Cells* 17 (2017): 434–441.

43. M. B. Mogensen, M. Chen, H. L. Frandsen, et al., "Ni Migration in Solid Oxide Cell Electrodes: Review and Revised Hypothesis," *Fuel Cells* 21 (2021): 415–429.

44. M. S. Khan, X. Xu, R. Knibbe, and Z. Zhu, "Air Electrodes and Related Degradation Mechanisms in Solid Oxide Electrolysis and Reversible Solid Oxide Cells," *Renewable and Sustainable Energy Reviews* 143 (2021): 110918.

45. R. Knibbe, M. L. Traulsen, A. Hauch, S. D. Ebbesen, and M. Mogensen, "Solid Oxide Electrolysis Cells: Degradation at High Current Densities," *Journal of the Electrochemical Society* 157 (2010): B1209.

46. E. Bucher, C. Gspan, F. Hofer, and W. Sitte, "Sulphur Poisoning of the SOFC Cathode Material La$_{0.6}$Sr$_{0.4}$CoO$_{3-\delta}$," *Solid State Ionics* 238 (2013): 15–23.

47. E. Bucher, C. Gspan, and W. Sitte, "Degradation and Regeneration of the SOFC Cathode Material La$_{0.6}$Sr$_{0.4}$CoO$_{3-\delta}$ in SO$_2$-Containing Atmospheres," *Solid State Ionics* 272 (2015): 112–120.

48. F. Wang, H. Kishimoto, T. Ishiyama, et al., "A Review of Sulfur Poisoning of Solid Oxide Fuel Cell Cathode Materials for Solid Oxide Fuel Cells," *Journal of Power Sources* 478 (2020): 228763.

**Supporting Information**

Additional supporting information can be found online in the Supporting Information section.

Supplementary Information


# Cobalt-free High-Entropy Perovskite La$_{0.2}$Pr$_{0.2}$Nd$_{0.2}$Sm$_{0.2}$Sr$_{0.2}$FeO$_{3-\delta}$ Solid Oxide Cell Air Electrode with Enhanced Performance

Patrick Pretschuh[1], Andreas Egger[1], Priya Paulachan[2], Johanna Schöggl[2], Roland Brunner[2], Edith Bucher[1]

[1] Montanuniversitaet Leoben, Chair of Physical Chemistry, Franz-Josef-Straße 18, AT-8700 Leoben, Austria

[2] Materials Center Leoben Forschung GmbH, Roseggerstraße 12, AT-8700 Leoben, Austria

**S-1. Introduction**

High-entropy perovskites (HEP) are created by mixing $n \geq 5$ cations on the A- and/or B-sites of the lattice $ABO_3$. The configurational entropy $S_{config}$ of a HEP is calculated from the following equation, where $x_i$ represents the site fraction of the element $i$ and $R$ is the universal gas constant. By definition, HEPs have $S_{config} \geq 1.5\ R$ [1].

$$S_{config} = -R \left[ \left( \sum_{a=1}^{n_1} x_a ln x_a \right)_{A-site} + \left( \sum_{b=1}^{n_2} x_b ln x_b \right)_{B-site} + 3 \left( \sum_{c=1}^{n_3} x_c ln x_c \right)_{O-site} \right] \quad \text{Eq. (S-1)}$$

- $S_{config} \geq 1.5\ R$: High-entropy perovskites (HEP)
- $1.5\ R > S_{config} \geq 1\ R$: Medium-entropy perovskites (MEP)
- $1\ R > S_{config}$: Low-entropy perovskites (LEP)

**S-2. Characterization of button cells**

Table S-1: $R_{ohmic}$ and $R_p$ of symmetrical cells for different weight fractions of LPNSSF in the air electrode material (rest LNF) as obtained from fits to the impedance spectra shown in Figure 1. See main text for further details.

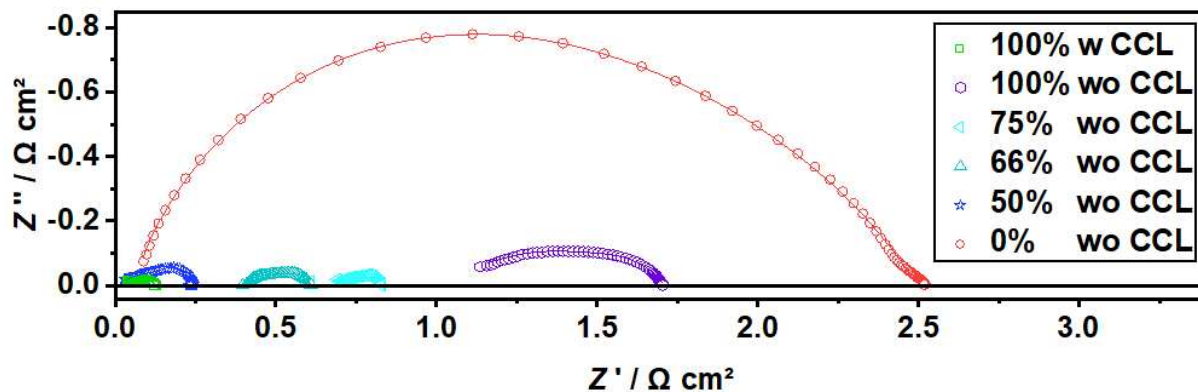| LPNSSF weight fraction | $R_{ohmic}$ / Ω cm² | $R_p$ / Ω cm² |
|:---:|:---:|:---:|
| 0% wo CCL | 0.025 | 2.469 |
| 50% wo CCL | 0.015 | 0.230 |
| 66% wo CCL | 0.371 | 0.239 |
| 75% wo CCL | 0.679 | 0.152 |
| 100% wo CCL | 1.078 | 0.631 |
| 100% <u>w</u> CCL | 0.010 | 0.121 |

Figure S-1: Impedance spectra of the symmetrical cells with GDC electrolyte and LPNSSF-LNF composite air electrodes with (w) and without (wo) LNF current collector (CCL) at 800 °C. Percentages given in the diagram refer to the LPNSSF content (wt.%) of the composite electrodes. Gas flow is 100 mL min$^{-1}$ 20% $O_2$ (rest Ar) in all cases. Lines are least-squares fits using the equivalent circuit described in the text. The inductance of the setup as well as the resistance of the GDC electrolyte are subtracted and the data divided by two.
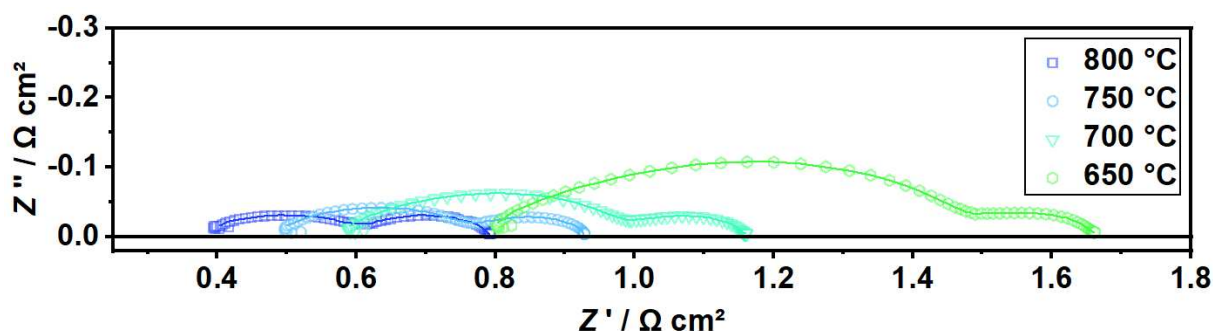


Figure S-2: Impedance spectra of a full button cell with single-phase LPNSSF air electrode recorded 100 mV below OCV at different temperatures. Flow rates are 500 mL min$^{-1}$ 20% $O_2$ (rest Ar) at the air electrode side and 100 mL min$^{-1}$ $H_2$ at the fuel electrode side. Lines are fits with the equivalent circuit model described in the text.
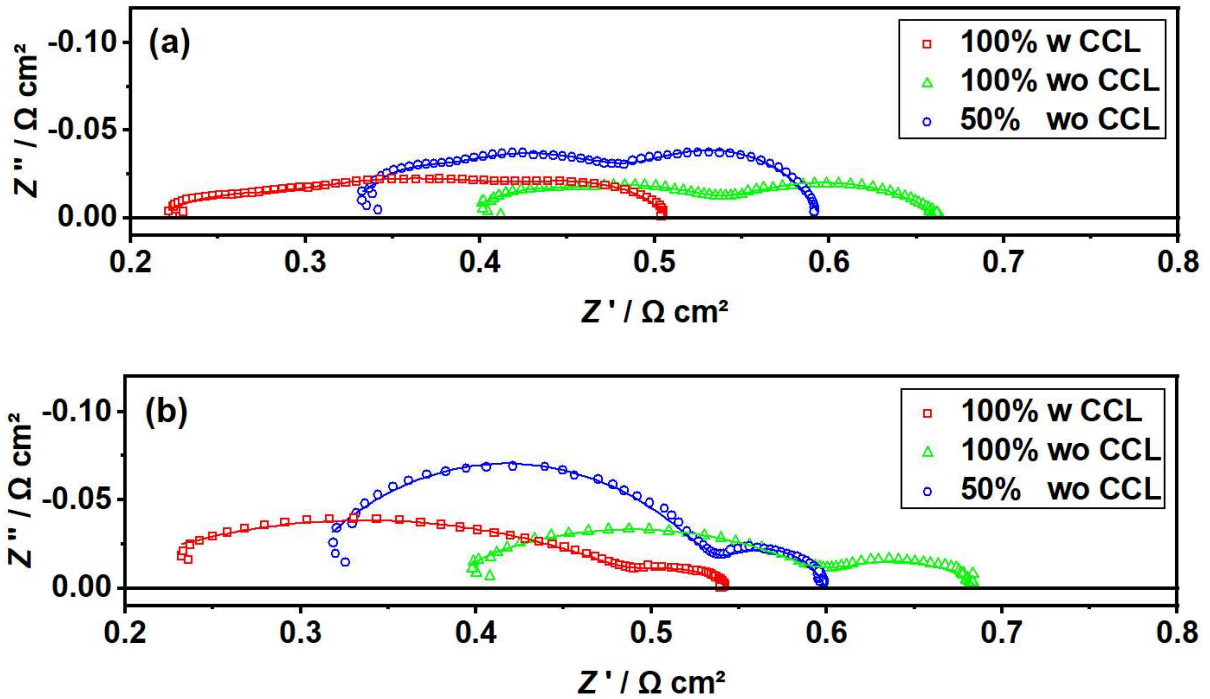
Figure S-3: Impedance spectra of full button cells with (w) and without (wo) a CCL at 0.7 V in SOFC (a) and 1.2 V in SOEC mode (b) at 800 °C. Percentages given in the legend refer to the LPNSSF weight fraction of the air electrode (the remainder is LNF). In SOFC mode (a), gas flows are 500 mL min$^{-1}$ 20% $O_2$ (rest Ar) at the air electrode and 100 mL min$^{-1}$ $H_2$ at the fuel electrode. In SOEC mode (b), gas flows are 40 mL min$^{-1}$ 20% $O_2$ (rest Ar) at the air electrode and 40 mL min$^{-1}$ $H_2$ with 50 vol.% $H_2O$ at the fuel electrode. Lines are fits with the equivalent circuit model described in the text.
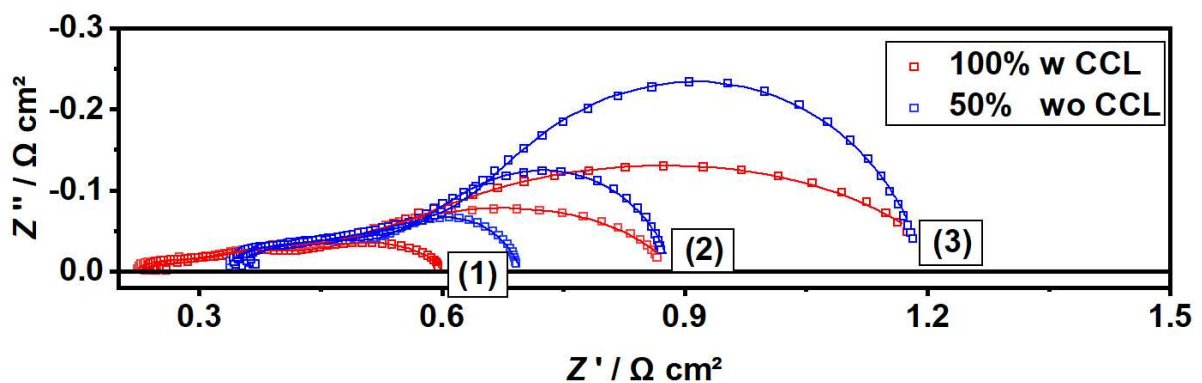


Figure S-4: Impedance spectra of full button cells with single-phase (100%) LPNSSF air electrode with CCL and 50% LPNSSF – 50% LNF composite electrode without CCL. The spectra were acquired in SOFC mode at 0.7 V and 800 °C for different air flows of 100 (1), 50 (2) and 33 (3) mL min$^{-1}$ (20% $O_2$, rest Ar). Fuel gas flow is 40 mL min$^{-1}$ $H_2$ in all cases. Lines are fits with the equivalent circuit model described in the text.
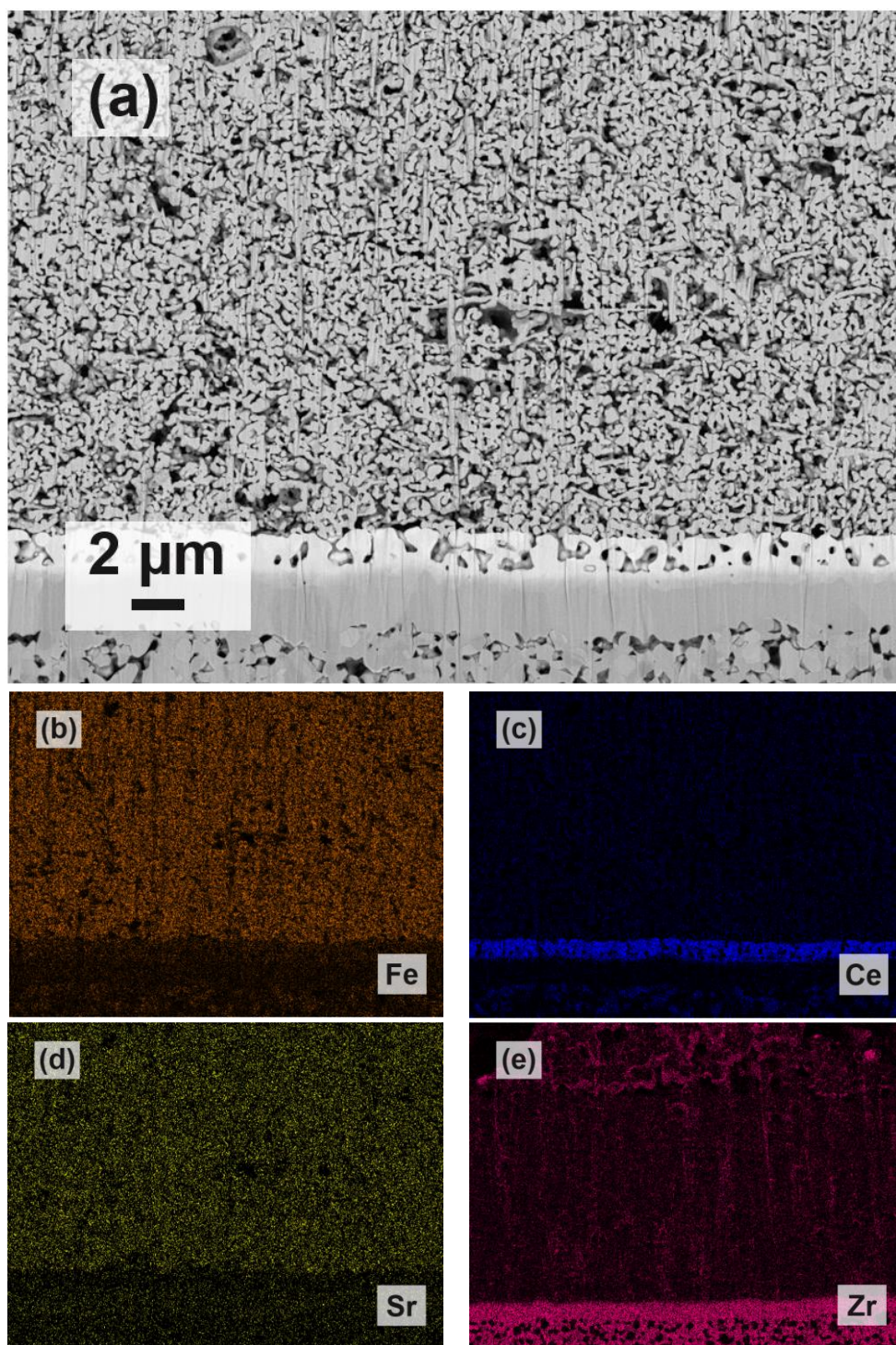
Figure S-5: Cross-section microstructural image of an ASC button cell with (a) a single-phase LPNSSF air electrode acquired by FESEM-BSE, and (b) – (e) elemental maps for Fe, Ce, Sr and Zr acquired by EDX.
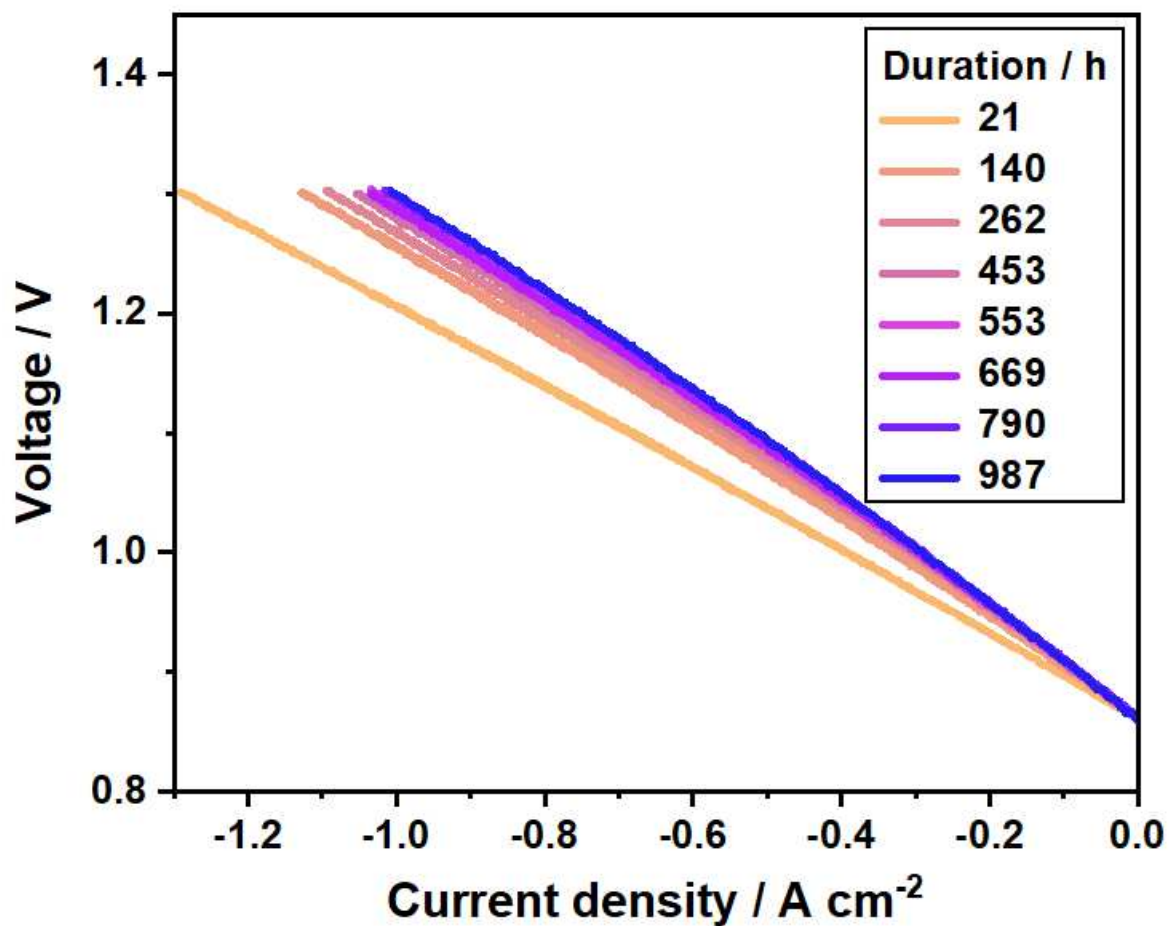
## S-3. Characterization of 5×5 cm² cells



Figure S-6: Current-voltage curves of a 5×5 cm² ASC with single-phase LPNSSF air electrode and LNF CCL recorded at 800 °C in between long-term electrolysis operation (continuous polarization –0.688 A cm$^{-2}$) with 80 vol.% $H_2O$ (rest $H_2$) and 1 L min$^{-1}$ fuel gas flow at the specified times during the long-term test.
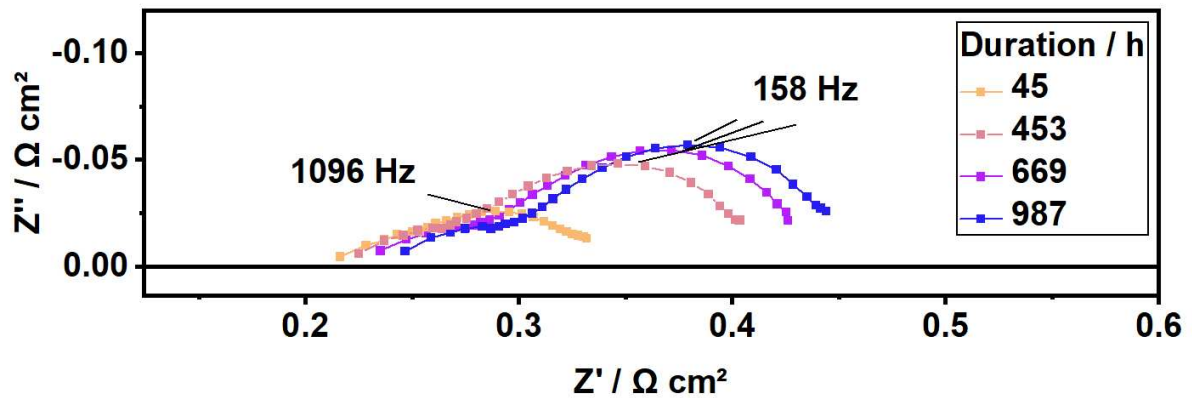
Figure S-7: Impedance spectra of a 5×5 cm² ASC with single-phase LPNSSF air electrode and LNF CCL recorded at OCV and 800 °C at the specified times during the long-term test. Fuel gas humidification is 80 vol.% $H_2O$ (rest $H_2$) at a gas flow of 1 L min$^{-1}$.
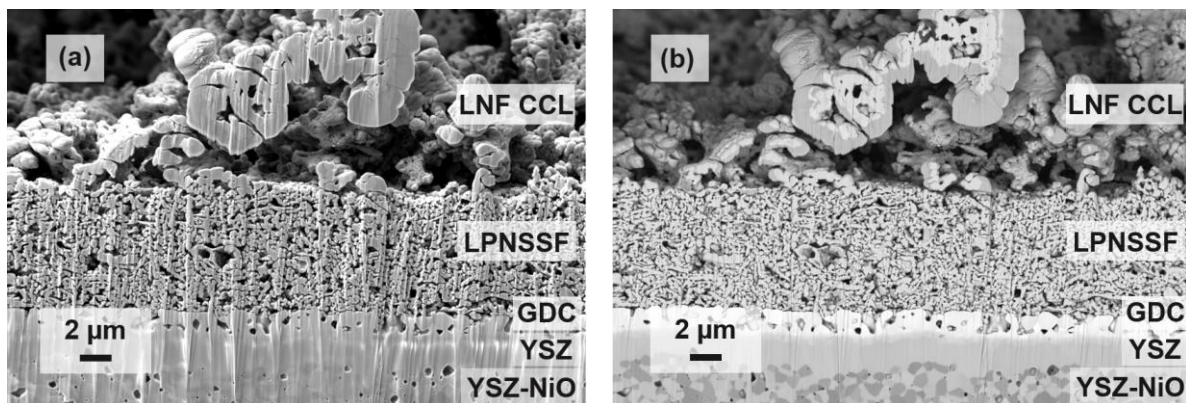


Figure S-8: FESEM cross section images of a fresh 5×5 cm² ASC with single-phase LPNSSF air electrode and LNF CCL in (a) SE and (b) BSE mode, showing the LNF current collector, LPNSSF air electrode, GDC diffusion barrier, YSZ electrolyte and YSZ-NiO fuel electrode layers and their interfaces.

**(a)**

LNF CCL

LPNSSF

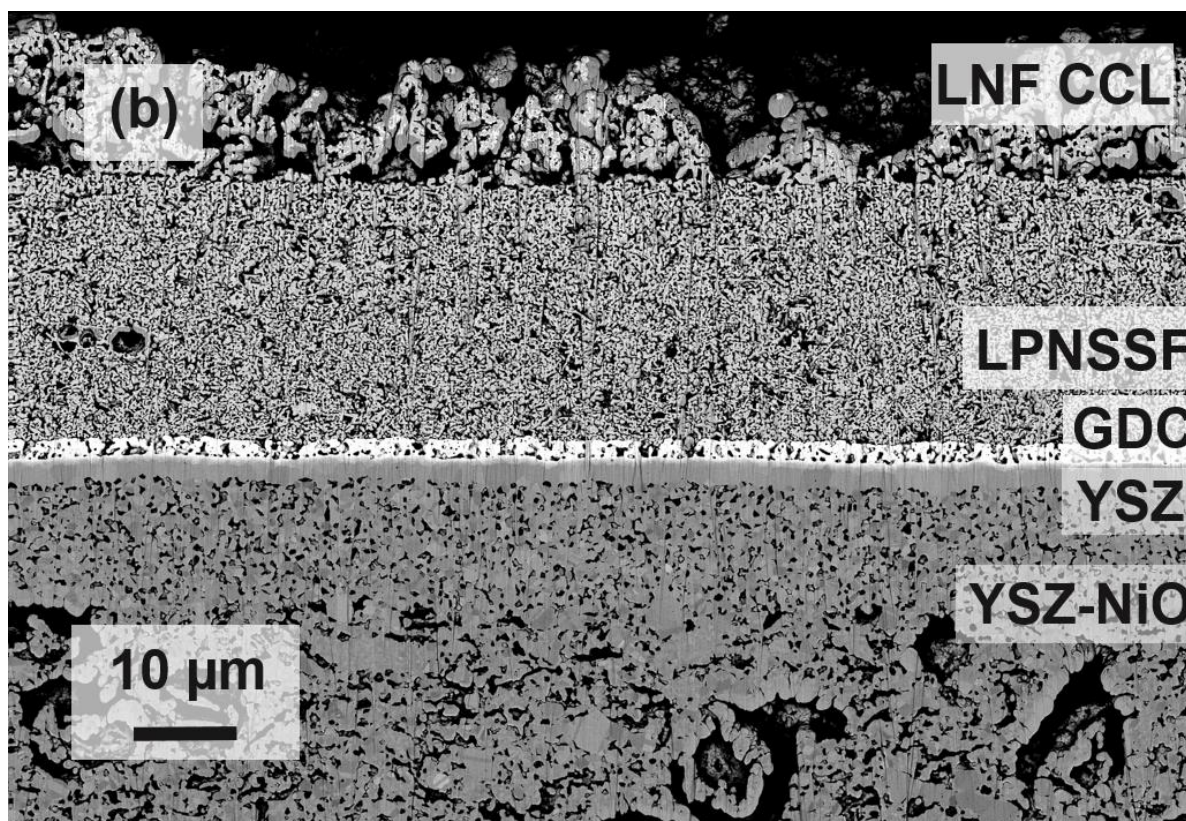GDC

YSZ

YSZ-NiO

10 μm

**(b)**

LNF CCL

LPNSSF

GDC

YSZ

YSZ-NiO

10 μm
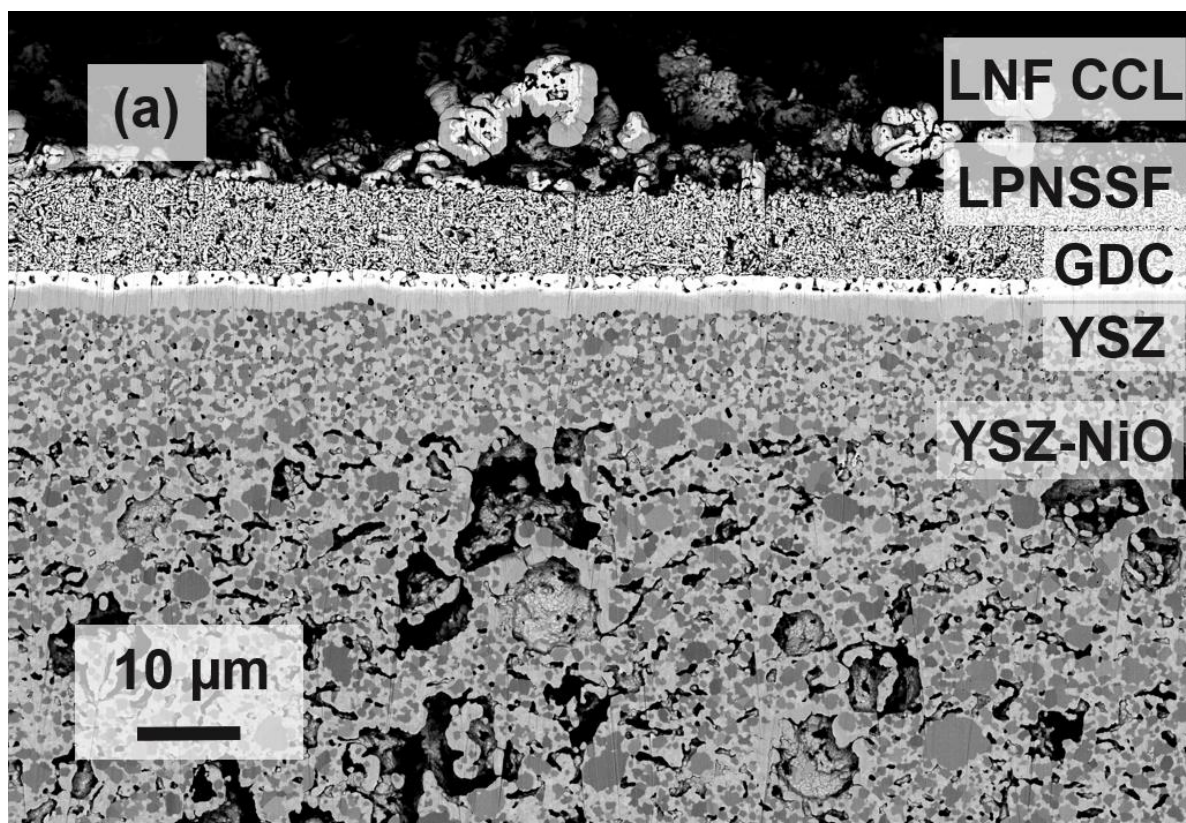
Figure S-9: FESEM-BSE cross section images of 5×5 cm² ASCs with single-phase LPNSSF air electrode and LNF CCL in the fresh state (a) and after long-term polarization (b).
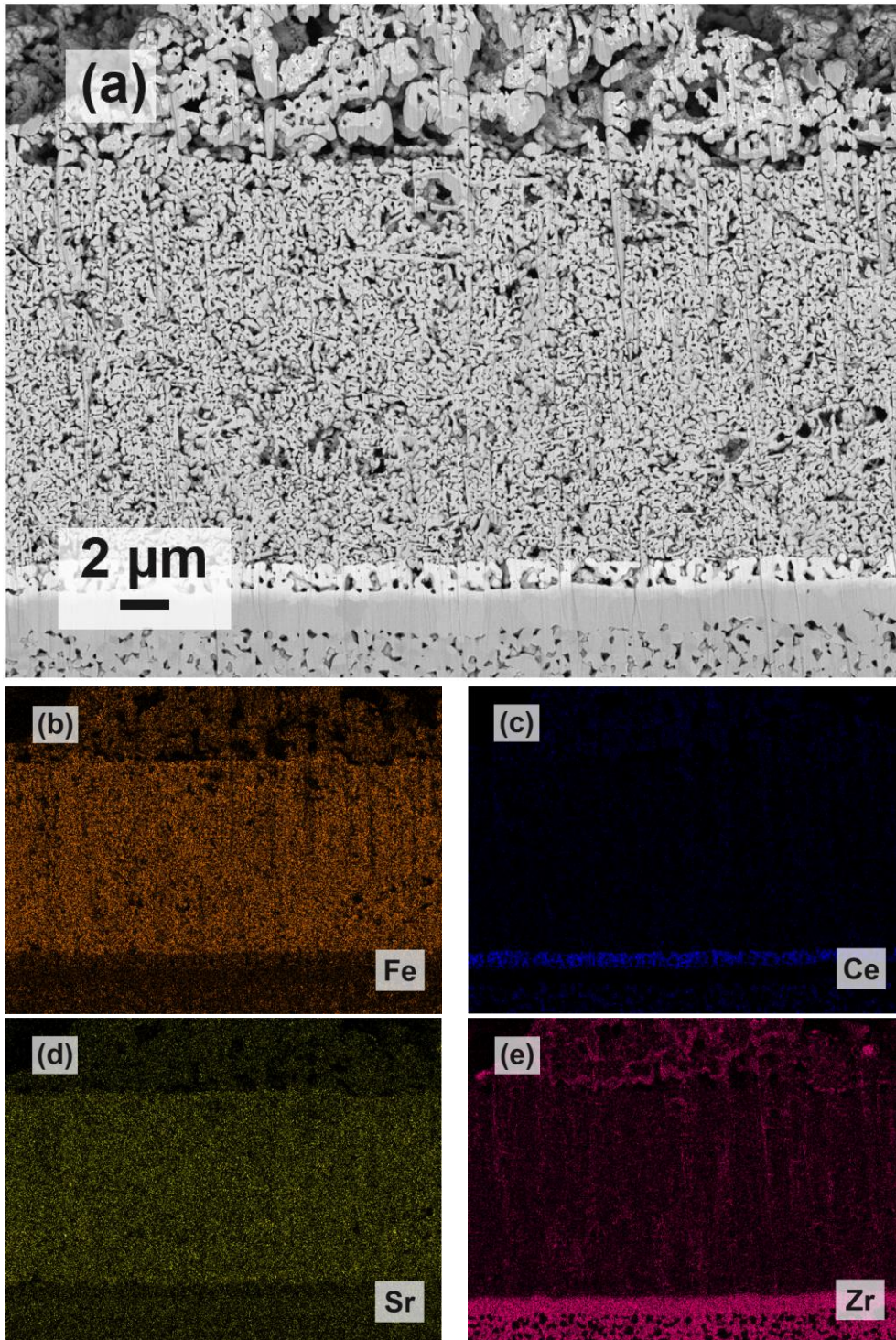
Figure S-10: Post-test microstructure image of the cross section of (a) a single-phase LPNSSF air electrode acquired by FESEM-BSE after long-term polarization of a 5×5 cm² ASC in SOEC mode; (b) – (e) are elemental maps for Fe, Ce, Sr and Zr acquired by EDX.

**References**

[1]   A. Sarkar, Q. Wang, A. Schiele, M.R. Chellali, S.S. Bhattacharya, D. Wang, T. Brezesinski,
      H. Hahn, L. Velasco, B. Breitung, *Advanced Materials* **2019**, *31*, 1806236.

# Solid State Ionics

## Crystal structure, electronic conductivity and oxygen exchange kinetics of high-entropy perovskites La0.2Pr0.2Nd0.2Sm0.2Sr0.2Co1-xFexO3-δ (x = 0, 0.5, 1)
### --Manuscript Draft--

| | |
|---|---|
| Manuscript Number: | |
| Article Type: | Research Paper |
| Keywords: | high-entropy perovskite; solid oxide cell; electronic conductivity; oxygen exchange kinetics; crystal structure; lattice distortion |
| Corresponding Author: | Edith Bucher<br>Montanuniversität Leoben<br>Leoben, Austria |
| First Author: | Patrick Pretschuh |
| Order of Authors: | Patrick Pretschuh |
| | Andreas Egger |
| | Edith Bucher |
| Abstract: | High-entropy perovskites (HEPs) are attracting increasing attention as air electrode materials for solid oxide cells (SOCs). In this work, three different HEPs from the series La0.2Pr0.2Nd0.2Sm0.2Sr0.2Co1-xFexO3-δ (x = 0, 0.5, 1) are synthesized using the citric acid- ethylenediaminetetraacetate (EDTA) method. X-ray diffraction analysis finds crystal structures with the orthorhombic space group 62 (Pnma) at room temperature. The lattice distortion increases with increased Fe-substitution at the B-site. The electrical conductivity ($\sigma$e) is determined at temperatures from 600 to 850°C and oxygen partial pressures (pO2) between 0.001 and 0.15 bar. For the pure cobaltate, $\sigma$e is 1469 S cm-1 at 800°C and 0.15 bar pO2. The conductivity is significantly reduced with Fe-doping, reaching 87 S cm-1 for the pure ferrate at 800°C. The chemical oxygen surface exchange coefficient (kchem) and the chemical oxygen diffusion coefficient (Dchem) are determined by the electrical conductivity relaxation technique. Dchem is found to be quite independent of B-site doping and pO2, with values of approx. 5×10-6 cm2 s-1 at 800°C. In contrast, kchem is strongly influenced by the B-site composition, which results in an increase of more than one order of magnitude from the ferrate (3.4×10-5 cm s-1) to the cobaltate (7.7×10-4 cm s-1) at 800°C and 0.001 bar pO2. This clearly demonstrates the beneficial effects of Co on the electronic conductivity as well as on the catalytic activity for the oxygen surface exchange reaction. |
| Suggested Reviewers: | Clement Nicollet<br>Clement.Nicollet@univ-nantes.fr |
| | Peter Vang Hendriksen<br>pvhe@dtu.dk |
| | Vaibhav Vibhu<br>v.vibhu@fz-juelich.de |

# Crystal structure, electronic conductivity and oxygen exchange kinetics of high-entropy perovskites La$_{0.2}$Pr$_{0.2}$Nd$_{0.2}$Sm$_{0.2}$Sr$_{0.2}$Co$_{1-x}$Fe$_x$O$_{3-\delta}$ (x = 0, 0.5, 1)

Patrick Pretschuh, Andreas Egger, Edith Bucher*

Chair of Physical Chemistry, Montanuniversitaet Leoben, Franz-Josef-Straße 18,

8700 Leoben, Austria

## Abstract

High-entropy perovskites (HEPs) are attracting increasing attention as air electrode materials for solid oxide cells (SOCs). In this work, three different HEPs from the series La$_{0.2}$Pr$_{0.2}$Nd$_{0.2}$Sm$_{0.2}$Sr$_{0.2}$Co$_{1-x}$Fe$_x$O$_{3-\delta}$ (x = 0, 0.5, 1) are synthesized using the citric acid-ethylenediaminetetraacetate (EDTA) method. X-ray diffraction analysis finds crystal structures with the orthorhombic space group 62 (*Pnma*) at room temperature. The lattice distortion increases with increased Fe-substitution at the B-site. The electrical conductivity ($\sigma_e$) is determined at temperatures from 600 to 850°C and oxygen partial pressures ($pO_2$) between 0.001 and 0.15 bar. For the pure cobaltate, $\sigma_e$ is 1469 S cm$^{-1}$ at 800°C and 0.15 bar $pO_2$. The conductivity is significantly reduced with Fe-doping, reaching 87 S cm$^{-1}$ for the pure ferrate at 800°C. The chemical oxygen surface exchange coefficient ($k_{chem}$) and the chemical oxygen diffusion coefficient ($D_{chem}$) are determined by the electrical conductivity relaxation technique. $D_{chem}$ is found to be quite independent of B-site doping and $pO_2$, with values of approx. 5×10$^{-6}$ cm$^2$ s$^{-1}$ at 800°C. In contrast, $k_{chem}$ is strongly influenced by the B-site composition, which results in an increase of more than one order of magnitude from the ferrate (3.4×10$^{-5}$ cm s$^{-1}$) to the cobaltate (7.7×10$^{-4}$ cm s$^{-1}$) at 800°C and 0.001 bar $pO_2$. This clearly demonstrates the beneficial effects of Co on the electronic conductivity as well as on the catalytic activity for the oxygen surface exchange reaction.

**Keywords:** high-entropy perovskite; solid oxide cell; electronic conductivity; oxygen exchange kinetics; crystal structure; lattice distortion

*Corresponding author: Edith Bucher, Chair of Physical Chemistry, Montanuniversitaet Leoben, Franz-Josef-Straße 18, 8700 Leoben, Austria; tel.: +43 3842 402 4813; e-mail address: edith.bucher@unileoben.ac.at

# 1. Introduction

Solid oxide fuel cells (SOFCs) and solid oxide electrolysis cells (SOECs) are promising technologies for the efficient conversion between chemical energy and electrical energy at a large scale. For a widespread application of these technologies, many requirements must be met. Several of those refer to material benchmarks of the air electrode material such as fast surface exchange and transport kinetics of oxygen, high electronic and ionic conductivity and chemical stability in operational environments [1-3].

The growing demand for renewable energy underlines the importance of advances in material science. High-entropy perovskites (HEPs) are an emerging class of materials that have the potential to play an important role as a choice for air electrode materials. The underlying concept of introducing five or more cations onto the A- and/or B-sites within the crystal lattice has been successfully applied to alloys and oxides [4-7]. The increased configurational entropy may induce phase-stabilization effects such as slowed down cation diffusion and thereby enhance thermodynamic stability [8,9]. A term often used in the context of high-entropy stabilization is the so-called "cocktail effect". According to this effect, high-entropy compounds can exhibit material properties, which are beyond of what would be expected from averaging over the material properties of the single-ion compounds [10,11]. However, few systematic studies on fundamental structure-property relationships of these novel compounds are available. With respect to applications, recent studies show impressive progress in solid oxide cells (SOCs) using high-entropy perovskite and medium-entropy perovskite (MEP) air electrodes, demonstrating excellent electrochemical performance and stability, which exceed the state of the art [12-15].

This study investigates the crystal structure, electronic conductivity, oxygen surface exchange kinetics, and oxygen diffusivity in a series of high-entropy perovskites: $La_{0.2}Pr_{0.2}Nd_{0.2}Sm_{0.2}Sr_{0.2}CoO_{3-\delta}$ (LPNSSC), $La_{0.2}Pr_{0.2}Nd_{0.2}Sm_{0.2}Sr_{0.2}Co_{0.5}Fe_{0.5}O_{3-\delta}$ (LPNSSCF) and $La_{0.2}Pr_{0.2}Nd_{0.2}Sm_{0.2}Sr_{0.2}FeO_{3-\delta}$ (LPNSSF). These materials are high-entropy analogs of the previously investigated state-of-the-art perovskites $La_{0.8}Sr_{0.2}CoO_{3-\delta}$ (LSC82),

La$_{0.8}$Sr$_{0.2}$Co$_{0.5}$Fe$_{0.5}$O$_{3-\delta}$ (LSCF8255) and La$_{0.8}$Sr$_{0.2}$FeO$_{3-\delta}$ (LSF82). Since material data of high-entropy perovskites is scarce, this work aims to contribute to the development of more efficient and durable air electrodes by investigating the compounds in terms of their fundamental material properties. The results obtained in this work are then examined and compared with the state of the art.

## 2. Experimental

### 2.1 Sample preparation

All compounds were synthesized via the citric acid-ethylenediaminetetraacetate (EDTA) sol-gel method. Stoichiometric amounts of the metal nitrates (purchased from Merck KGaA) were mixed with deionized water at a temperature of 80°C. After complete dissolution, citric acid and EDTA were added. To adjust the pH of the mixture to ~8, an aqueous NH$_3$ solution was used. Depending on the composition, the resulting solution turned violet (cobalt) to brown (iron). The temperature of the mixture was raised until the water had completely evaporated and self-ignition occurred. The obtained raw ash was ground in a mortar and the resulting powders calcined at 1100°C for 2 h with heating and cooling rates of 2 K min$^{-1}$. The calcined powders were then ball-milled with zirconia balls in ethanol until a particle size of $d_{50} = 1.5 - 2$ µm was reached. Subsequently, the dried powders were isostatically pressed at 250 MPa into pellets with a cylindrical shape and then sintered for 10 h at different temperatures (see Tab. 1) with heating and cooling rates of 1 K min$^{-1}$. From the sintered bodies, rectangular samples were cut with a diamond wire saw and all sides were treated using SiC grinding disks with 40 µm particle size. All material parameters were obtained from bar-shaped samples, with the exception of oxygen surface exchange measurements on LPNSSC, where a thin slab was used. Geometric densities were calculated from mass and sample dimensions. A comparison with theoretical density values obtained by Rietveld refinement showed relative densities ≥ 93% for all compounds (Tab. 1). Two thin grooves were cut symmetrically along the circumference of the bars for easier attachment of the voltage probes. The front faces were

contacted with gold foils and gold wires attached with gold paste. In case of LPNSSC, a thin slab with a cross section of 5×5 mm² and a thickness of 0.358 mm was cut from the pellet with a diamond wire saw. The specimen was equipped with gold wires at its corners and used to determine the surface exchange coefficient of oxygen in van der Pauw geometry [16,17].

Tab. 1. Sintering temperatures and density values of the investigated HEPs.

| Sample | Sintering temperature | Geometric density | XRD density | Relative density |
|--------|:---:|:---:|:---:|:---:|
| | °C | g cm$^{-3}$ | g cm$^{-3}$ | % |
| **LPNSSC** | 1200 | 7.075 | 7.211 | 98 |
| **LPNSSCF** | 1200 | 6.761 | 6.927 | 97 |
| **LPNSSF** | 1350 | 6.190 | 6.651 | 93 |

## 2.2 Structural analysis

The calcined powders were examined by X-ray diffraction (XRD) analysis at room temperature. A powder diffractometer (Bruker AXS, model D8 Advance) using Cu-Kα radiation was used in the 2θ range of 10° to 100° with a resolution of 0.020° and 2 s acquisition time per step. The X-ray source was operated at 40 kV and 25 mA. The commercial crystallographic database PDF-4+ (ICDD) and the integrated software SIeve+ were used to analyze the X-ray patterns. Structural evaluation was performed by Rietveld refinement using the TOPAS software package (Bruker AXS). Graphical illustrations of the crystal structure were created using Vesta [18].

## 2.3 Electronic conductivity and conductivity relaxation measurements

The bar-shaped samples were electrically contacted and mounted in a quartz glass reactor placed inside a tubular furnace with gas inlet and outlet. The electronic conductivity ($\sigma_e$) was determined in linear four-point geometry at different temperatures and oxygen partial pressures. This was accomplished using a combination of a current source and nano-voltmeter (Keithley, models 2400 and 182). Oxygen partial pressures were varied by supplying pre-mixed $O_2$/Ar test gases at flow rates of 3 L $h^{-1}$. Equilibration periods of typically 12 to 24 hours were implemented after each temperature change. The electronic conductivity was calculated from the resistance and the geometric characteristics of the samples according to Eq. 1

$$\sigma_e = \frac{1}{R} \cdot \frac{d}{A} \quad \text{(Eq. 1)}$$

where $d$ represents the distance between the voltage probes, $A$ denotes the cross-sectional area of the sample and $R$ is the resistance. Several measurements were performed at different current levels and the resistance was derived from the slope of the regression line fitted to the voltage-current data in accordance with Ohm's law.

Chemical surface exchange coefficients ($k_{chem}$) and chemical diffusion coefficients ($D_{chem}$) of oxygen were determined by means of dc-conductivity relaxation measurements at various temperatures and oxygen partial pressures. After equilibration, the oxygen partial pressure was abruptly altered by manual switching of a four-way valve. Since the electronic conductivity of the sample depends on the oxygen content, this procedure leads to a gradual relaxation of $\sigma_e$ over time while approaching the new equilibrium state. For LPNSSF, the oxygen partial pressure was changed by a factor of 1.5. For LPNSSC and LPNSSCF, $pO_2$ steps were increased to a factor of 10 in order to obtain a sufficient signal-to-noise ratio in the relaxation curves. Kinetic parameters associated with the oxygen exchange were determined by fitting appropriate solutions of the diffusion equation to the conductivity transients using non-linear least squares regression analysis [19]. Bar-shaped samples were used for almost all conductivity relaxation experiments. As mentioned above, $k_{chem}$ of LPNSSC was obtained on

6

a separate sample prepared as thin square slab and measured in van der Pauw geometry [16,17]. For such thin samples, the surface reaction kinetics becomes more dominant in the overall oxygen exchange and thus $k_{chem}$ can be determined with higher accuracy [20].

## 3. Results and discussion

### 3.1 Crystal structure and phase purity

Structural refinement of the XRD-patterns was performed by the Rietveld method. In all cases, the perovskite phase was confirmed with high phase purity. The room-temperature patterns show an orthorhombic lattice distortion corresponding to the space group 62 (*Pnma*), which agrees with results of the low-entropy analogs LSC82 and LSF82 [21,22]. XRD patterns and results from Rietveld refinements are shown in Fig. 1. The lattice parameters of the investigated compounds are given in Tab. 2, atomic positions and selected bond lengths are listed in Tab. S-1 in the supplementary material. The lattice parameters and unit cell volumes increase with increasing Fe content, which is due to the larger ionic radius of $Fe^{3+}$ (0.645 Å) as compared to $Co^{3+}$ (0.61 Å) [23]. In Tab. 2, the pure cobaltate and ferrate HEPs are compared with their low-entropy analogs having the same composition with respect to Sr and Co/Fe, but containing only La as rare earth element on the A-site. The lattice parameters of LPNSSC and LPNSSF are consistently smaller than those of LSC82 and LSF82, respectively, and thus the cell volumes of the high-entropy compositions are also smaller. This is a consequence of the smaller ionic radii of $Pr^{3+}$ (1.32 Å) [24], $Nd^{3+}$ (1.27 Å) and $Sm^{3+}$ (1.24 Å) as compared to $La^{3+}$ (1.36 Å) [23]. It is interesting to note that the reduction in unit cell dimensions with the addition of Pr, Nd and Sm is more pronounced in LPNSSF than in LPNSSC. Based on the Goldschmidt's tolerance factors (deviation from unity), the lattice distortion increases with increasing Fe content, which has also been reported by other groups [25-27].
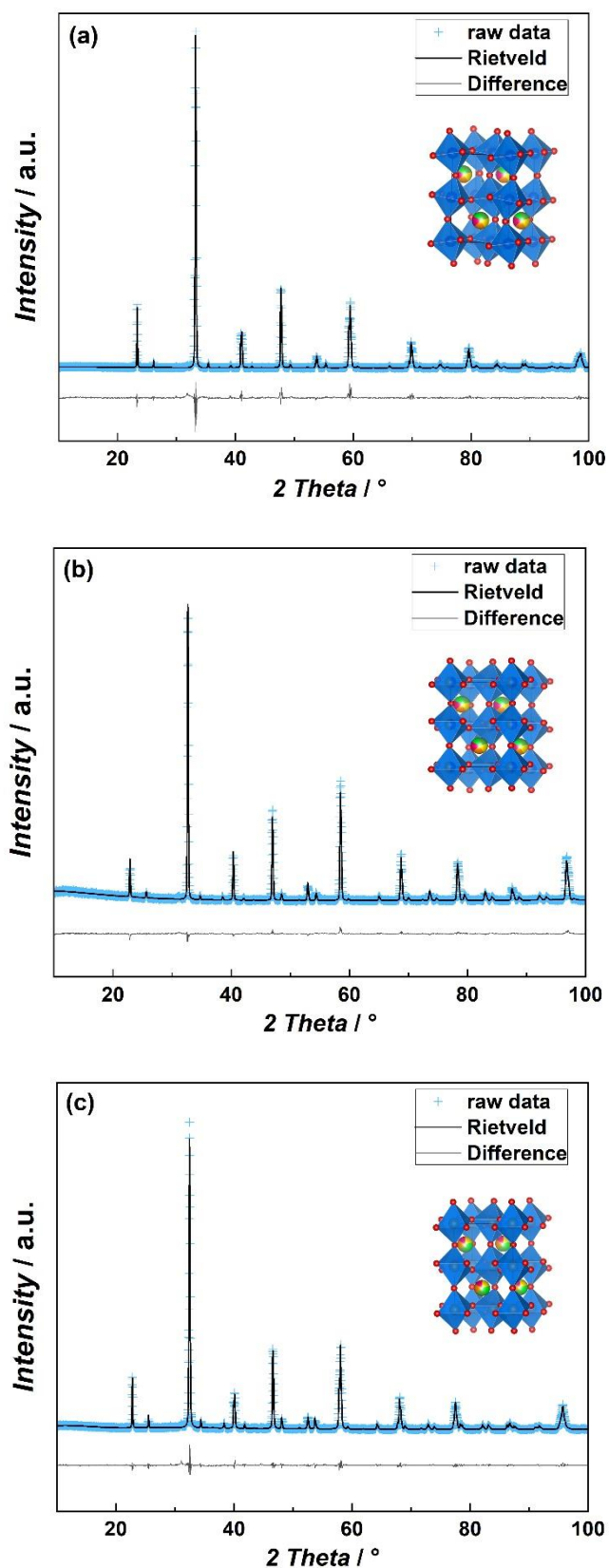
Fig. 1. Powder diffraction patterns (crosses) of LPNSSC (a), LPNSSCF (b) and LPNSSF (c).

The insets show the perovskite-type crystal structures obtained by Rietveld refinement.

Tab. 2. Lattice parameters and unit cell volumes of LPNSSC, LPNSSCF and LPNSSF obtained by Rietveld refinement in comparison with low-entropy analogs. $Z$ refers to the number of formula units per unit cell and $t$ is the Goldschmidt tolerance factor. All compounds have space group 62 (*Pnma*).

| Sample | $a$ / Å | $b$ / Å | $c$ / Å | $V$ / Å$^3$ | $Z$ | $t$ | Ref. |
|---|---|---|---|---|---|---|---|
| LPNSSC | 5.36704(7) | 7.60240(10) | 5.40271(6) | 220.44(5) | 4 | 0.960 | this work |
| LPNSSCF | 5.4411(2) | 7.6898(4) | 5.4486(3) | 227.98(2) | 4 | 0.951 | this work |
| LPNSSF | 5.52592(8) | 7.77630(14) | 5.49082(9) | 235.95(7) | 4 | 0.943 | this work |
| LSC82 | 5.3881(3) | 7.6543(5) | 5.4365(4) | 224.2 | 4 | 0.977 | [21]* |
| LSF82 | 5.551(4) | 7.865(9) | 5.544(3) | 242.03 | 4 | 0.960 | [22,28] |

* axis labels were permuted for easier comparison with LPNSSC

## 3.2 Electronic conductivity

Fig. 2 shows the electronic conductivity ($\sigma_e$) of the studied HEPs at different temperatures and oxygen partial pressures. The data sets are also displayed in a single diagram in Fig. S-1 of the supplementary material for comparison. For LPNSSC (Fig. 2a), $\sigma_e$ ranges from 1270 S cm$^{-1}$ (800°C, 0.001 bar $p$O$_2$) to 1660 S cm$^{-1}$ (600°C, 0.15 bar $p$O$_2$). Within the investigated temperature and $p$O$_2$ range, the electronic conductivity of LPNSSC decreases with increasing temperature and decreasing oxygen partial pressure. The observed $p$O$_2$ dependence is characteristic for a p-type electronic conductor, where the concentration of electron holes is reduced with the release of oxygen ions from the lattice [29]. The electrical conductivity shows much less variation with $p$O$_2$ at 600°C as compared to 800°C and the dependency of $\sigma_e$ on $p$O$_2$ is more sensitive for gas atmospheres with low oxygen content. Compared with the low-entropy compound LSC82, the electrical conductivity of LPNSSC seems to be higher by

approx. 200 S cm$^{-1}$ [30-32]. The characteristics of the $\sigma_e - T - pO_2$ relationship appears to be similar to LSC82, thus a maximum in $\sigma_e$ is expected to occur at temperatures below 600°C [31,32].

Substitution of Co with Fe significantly reduces the electronic conductivity. For example, at 800°C and 0.01 bar $pO_2$, $\sigma_e$ is 1390 S cm$^{-1}$ for LPNSSC, 240 S cm$^{-1}$ for LPNSSCF and 75 S cm$^{-1}$ for LPNSSF. Compared with LPNSSC, the conductivity maximum of LPNSSCF is shifted to higher temperatures and falls within the temperature range studied in this work (Fig. 2b). A similar shift has also been reported by Tai et al. for $La_{0.8}Sr_{0.2}Co_{0.5}Fe_{0.5}O_{3-\delta}$ (LSCF8255) [31]. Interestingly, upon further increase of the Fe content (LPNSSF) the conductivity maximum reverts back to lower temperatures (Fig. 2c). Similar to the cobaltite, the conductivity of the Fe-containing HEPs decreases with decreasing $pO_2$, which again indicates a p-type conduction mechanism. Both LPNSSCF and LPNSSF show little difference in $\sigma_e$ to their low-entropy analogs [31].

It is well known that Fe-substitution in Co-rich perovskites reduces the electronic conductivity (e.g. [31,33,34]). It has been suggested in the literature that iron ions act as traps for the defect electrons, thus leading to a decrease in the hole mobility [31]. This implies that, instead of $Co^{4+}$ ions, $Fe^{4+}$ ions are preferentially formed as charge compensation of the acceptor dopant ($Sr^{2+}$). When the iron content exceeds the percolation threshold, the dominant mode of electrical conduction transitions to short-range hopping between neighboring $Fe^{4+}$-$Fe^{3+}$ couples, i.e. a small polaron conduction mechanism [31].
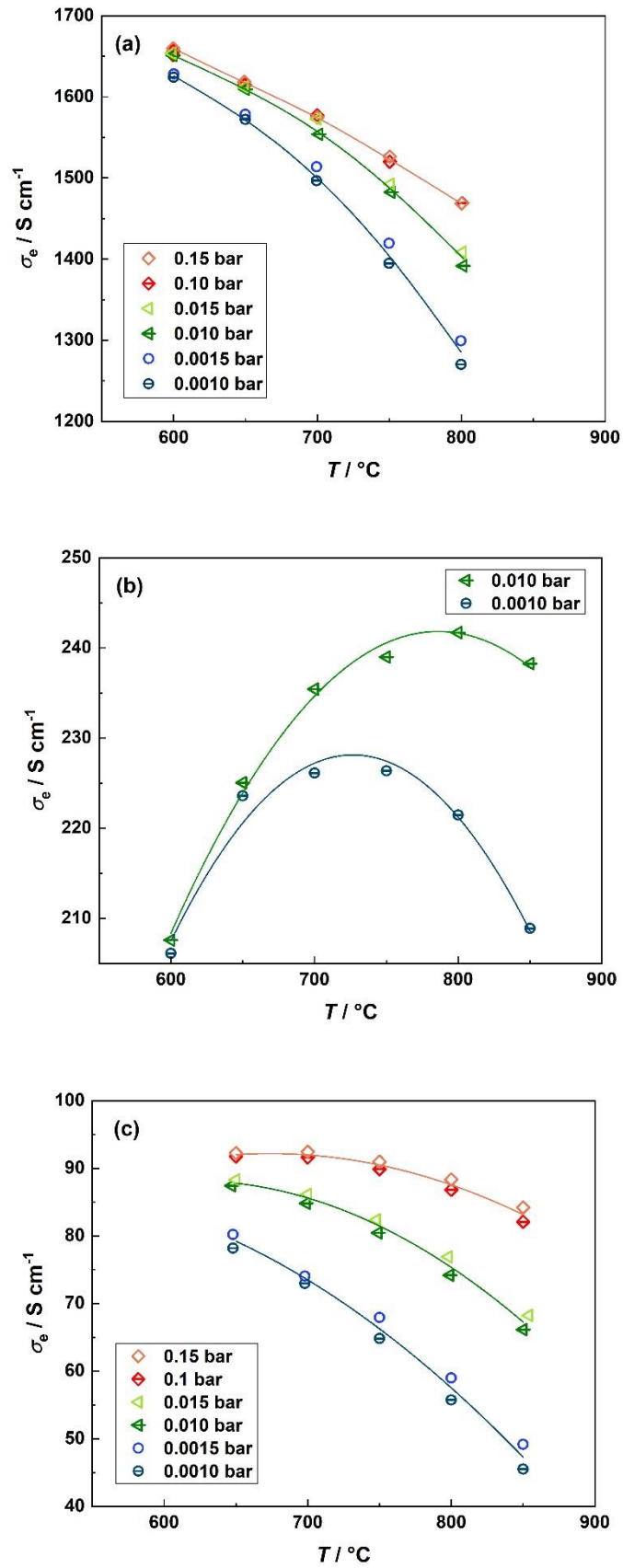
Fig. 2. Electronic conductivity ($\sigma_e$) of LPNSSC (a), LPNSSCF (b) and LPNSSF (c) at different temperatures and oxygen partial pressures. Lines are a guide to the eye.

### 3.3 Oxygen exchange kinetics

Chemical diffusion coefficients of oxygen $D_{chem}$ (Fig. 3) and surface exchange coefficients of oxygen $k_{chem}$ (Fig. 4) were determined in the temperature range of 650 to 850°C and oxygen partial pressures of 0.1, 0.01 and 0.001 bar. Activation energies ($E_a$) were obtained by linear regression analysis of the data in Arrhenius representation. To check the consistency of the data, results obtained from steps in oxygen partial pressure from lower to higher $pO_2$ (oxidation) and from higher to lower $pO_2$ (reduction) are displayed in the diagrams. In general, the agreement between oxidation and reduction runs is excellent. Tab. 3 gives a comparison of diffusion coefficients and surface exchange coefficient of the investigated HEPs at $10^{-3}$ bar $pO_2$.

Fig. 3 presents chemical diffusion coefficients at different temperatures and oxygen partial pressures. The $D_{chem}$ values of all three HEPs increase with increasing temperature, which is as expected since diffusion is a thermally activated process [35]. At constant temperature, the diffusivities of LPNSSC, LPNSSCF and LPNSSF are practically independent of the oxygen partial pressure ($0.001 \leq pO_2$ / bar $\leq 0.15$). The $pO_2$-dependence of $D_{chem}$ of mixed ionic-electronic conducting perovskites is not trivial, since not only the A- and B-site composition, but also the $pO_2$-dependences of the concentration and mobility of the oxygen vacancies play a role. At constant temperature and a given A- and B-site composition, the oxygen nonstoichiometry $\delta$ increases with decreasing oxygen partial pressure (refer to e.g. [36-42]), which would lead – if no other factors play a role – to an increase in $D_{chem}$. However, several experimental investigations showed that this is not the case. In various studies (including the present work), $D_{chem}$ was found to be almost independent the oxygen partial pressure, or even to decrease with decreasing $pO_2$ [40,42-48]. An interplay of two factors, (i) the increase in the *total* number of oxygen vacancies, and (ii) a decrease in the number of *mobile* oxygen with decreasing oxygen partial pressure has been assumed to be responsible for this effect [42,43]. Thus, a comprehensive study of the oxygen nonstoichiometry of the three investigated HEPs

as a function of temperature and oxygen partial pressure and defect chemical analysis (which are beyond the scope of the present study) would be required to deconvolute the above-mentioned effects.

Comparing the investigated HEPs, very similar results of $D_{chem}$ are observed for LPNSSC, LPNSSCF and LPNSSF. The activation energies of $D_{chem}$ are also quite similar, with the lowest value of 92 kJ mol$^{-1}$ found for LPNSSF and the highest value of 124 kJ mol$^{-1}$ for LPNSSCF. At 850°C, $D_{chem}$ of all three compounds is close to $1 \times 10^{-5}$ cm s$^{-1}$. Diffusion coefficients of the studied compounds are compared with those of low-entropy analogs with the same B-site composition and the same (or similar) Sr content on the A-site. Good agreement between LPNSSC and $La_{0.85}Sr_{0.15}CoO_{3-\delta}$ [49] is found (Fig. 3a). $D_{chem}$ of $La_{0.6}Sr_{0.4}Co_{0.5}Fe_{0.5}O_{3-\delta}$ (LSCF6455) [42] is almost one order of magnitude higher than that of LPNSSCF (Fig. 3b). This, however, can be attributed to the higher level of acceptor-doping (40% Sr) in LSCF6455 and the corresponding increase in the concentration of oxygen vacancies [42]. For LPNSSF, good agreement with the low-entropy analog LSF82 [50] is observed (Fig. 3c). Within the limits of experimental errors, the activation energies of $D_{chem}$ obtained for the HEPs in this study agree well with literature data of the corresponding low-entropy analogs (Figs. 3a–3c).

When discussing the dependence of $D_{chem}$ on the B-site composition at a given A-site occupancy as with $La_{0.2}Pr_{0.2}Nd_{0.2}Sm_{0.2}Sr_{0.2}Co_{1-x}Fe_xO_{3-\delta}$ (x = 0, 0.5, 1), one has to consider the influence of the B-site elements on the concentration and mobility of oxygen vacancies. In the case of mixed ionic-electronic conducting low-entropy perovskites, the oxygen nonstoichiometry increases in the order $AFeO_{3-\delta} < A(Co,Fe)O_{3-\delta} < ACoO_{3-\delta}$ (see Fig. S-2) [31,36-39,41,51], which should lead to an increase in $D_{chem}$ in the same order. However, the interpretation is not this straightforward. It has been shown that especially for those compounds which exhibit a large concentration of oxygen vacancies, such as $(La,Sr)CoO_{3-\delta}$, oxygen vacancy ordering can lead to a decrease in $D_{chem}$ and in ionic conductivity with increasing oxygen vacancy concentration at high values of $\delta$ [39,41,52,53]. Therefore, an in-depth analysis of the complex influence of the B-site elements on $D_{chem}$ of LPNSSC, LPNSSCF, and

LPNSSF would require defect chemical analysis, which is beyond the scope of the present study.
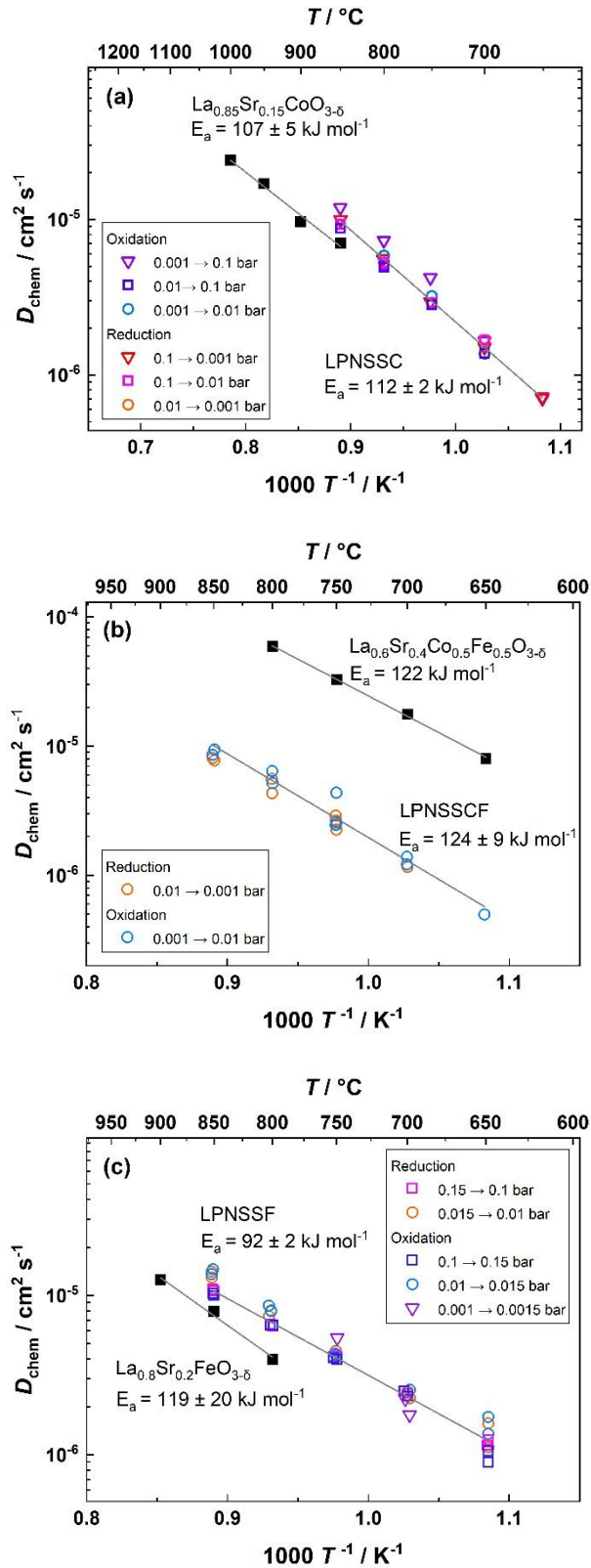
Fig. 3. Arrhenius plots of chemical diffusion coefficients of oxygen ($D_{chem}$) of LPNSSC (a), LPNSSCF (b) and LPNSSF (c) at various oxygen partial pressures with calculated activation energies ($E_a$). The results are compared with literature data of similar low-entropy perovskites $La_{0.85}Sr_{0.15}CoO_{3-\delta}$ [49], LSCF6455 [42] and LSF82 [50].

Chemical surface exchange coefficients of oxygen ($k_{chem}$) are shown in Fig. 4 as a function of temperature and oxygen partial pressure. The surface exchange coefficients increase with increasing temperature. At $10^{-3}$ bar $pO_2$, the activation energies of $k_{chem}$ range from ~70 kJ mol$^{-1}$ for the cobaltate LPNSSC to ~120 kJ mol$^{-1}$ for LPNSSCF and LPNSSF. These values lie within the range of activation energies found in literature, which vary from 67 to 216 kJ mol$^{-1}$ for similar low-entropy perovskites with Co or Fe on the B-site [36,42,43,48,54]. The $pO_2$-dependence of $k_{chem}$ could only be studied in the case of LPNSSF, where a decrease in the surface exchange coefficient by an order of magnitude was found when the $pO_2$ was decreased from $10^{-2}$ to $10^{-3}$ bar. Similar results were reported in the literature for the low-entropy analogs $La_{0.85}Sr_{0.15}CoO_{3-\delta}$ [49], LSC82 [43], LSCF6455 [42], and LSF82 [50]. This trend and the slope of log($k_{chem}$) vs. log($pO_2$) are determined by the $pO_2$-dependences of the concentrations and mobilities of the electronic and ionic charge carriers (electron holes and oxygen vacancies, respectively) as well as by the rate-determining step of the surface exchange reaction [46,47,55]. An in-depth analysis is, however, beyond the scope of the present work.

A comparison between the investigated HEPs at $10^{-3}$ bar $pO_2$ shows an increase in oxygen surface exchange coefficients upon the substitution of Fe with Co. This effect is evident across the entire investigated temperature range. For example, at 800°C and $10^{-3}$ bar $pO_2$, $k_{chem}$ is increased by a factor of more than 20 from $3.4 \times 10^{-5}$ cm s$^{-1}$ (LPNSSF) to $7.7 \times 10^{-4}$ cm s$^{-1}$ (LPNSSC). The enhancement is even more pronounced at lower temperatures, since the pure cobaltate has a lower activation energy as compared to the iron-containing HEPs. As expected, oxygen surface exchange rates of LPNSSCF are found to lie between those of the two end members LPNSSC and LPNSSF. These findings suggest that cobalt strongly promotes the kinetics of the surface exchange reaction, which is in line with literature results. For a fixed A-site composition, Co-rich perovskites usually have higher surface exchange coefficients than the Fe-rich analogs [36,40,42,56-58]. A comparison of $k_{chem}$ values with literature results is often difficult, since not only A- and B-site composition but also experimental issues such as

surface pretreatment, sample history, or impurities introduced by process gases or setup components, can have a strong influence on the surface exchange coefficients often leading to differences of 1-2 orders of magnitude [59-62]. However, the HEPs investigated in the present study show $k_{chem}$ values in the range of those reported in literature for the low-entropy perovskites $(La,Sr)FeO_{3-\delta}$ [46,47], $(La,Sr)(Co,Fe)O_{3-\delta}$ [56,57], $(La,Sr)CoO_{3-\delta}$ [36,40,58,63], compare Tab. 3 ($k_{chem}$ at 700°C) and data in Fig. S-3 of the supplementary material.
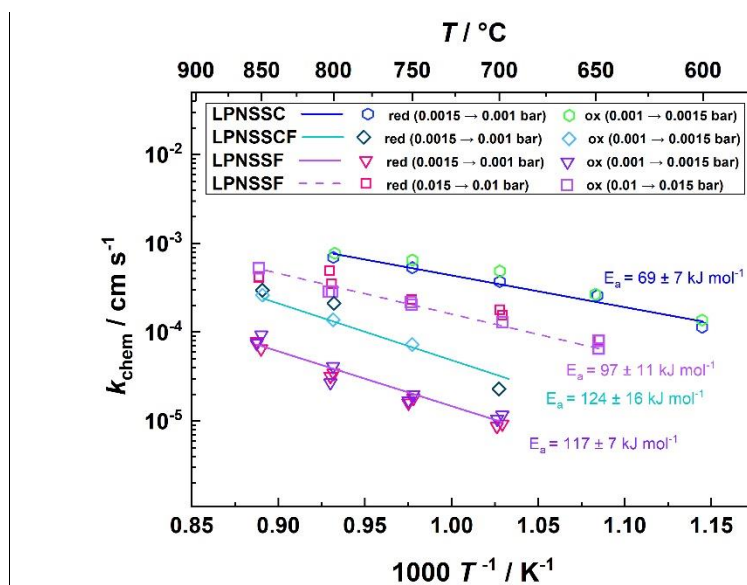


Fig. 4. Arrhenius plot of the chemical oxygen surface exchange coefficients ($k_{chem}$) of LPNSSC, LPNSSCF and LPNSSF at different oxygen partial pressures. Activation energies ($E_a$) are given in the diagram.

Tab. 3. Chemical diffusion coefficients ($D_{chem}$) and chemical surface exchange coefficients ($k_{chem}$) of oxygen of LPNSSC, LPNSSCF and LPNSSF at different temperatures at $10^{-3}$ bar $pO_2$.

| | LPNSSC | | LPNSSCF | | LPNSSF | |
|---|---|---|---|---|---|---|
| $T$ | $D_{chem}$ | $k_{chem}$ | $D_{chem}$ | $k_{chem}$ | $D_{chem}$ | $k_{chem}$ |
| °C | $cm^2\ s^{-1}$ | $cm\ s^{-1}$ | $cm^2\ s^{-1}$ | $cm\ s^{-1}$ | $cm^2\ s^{-1}$ | $cm\ s^{-1}$ |
| 850 | $1.0 \times 10^{-5}$ | – | $9.41 \times 10^{-6}$ | $2.6 \times 10^{-4}$ | $1.07 \times 10^{-5}$ | $7.45 \times 10^{-5}$ |
| 800 | $5.27 \times 10^{-6}$ | $7.70 \times 10^{-4}$ | $5.34 \times 10^{-6}$ | $1.37 \times 10^{-4}$ | $6.49 \times 10^{-6}$ | $3.44 \times 10^{-5}$ |
| 750 | $2.90 \times 10^{-6}$ | $5.31 \times 10^{-4}$ | $2.71 \times 10^{-6}$ | $7.25 \times 10^{-5}$ | $4.01 \times 10^{-6}$ | $1.81 \times 10^{-5}$ |
| 700 | $1.51 \times 10^{-6}$ | $3.71 \times 10^{-4}$ | $1.21 \times 10^{-6}$ | $2.3 \times 10^{-5}$ | $2.21 \times 10^{-6}$ | $8.65 \times 10^{-6}$ |
| 650 | $7.24 \times 10^{-7}$ | $2.19 \times 10^{-4}$ | – | – | $1.24 \times 10^{-6}$ | – |
| 600 | – | $1.13 \times 10^{-4}$ | – | – | – | – |

## 4. Summary and conclusions

Three high-entropy perovskites (HEPs) $La_{0.2}Pr_{0.2}Nd_{0.2}Sm_{0.2}Sr_{0.2}Co_{1-x}Fe_xO_{3-\delta}$ ($x = 0$, 0.5, 1) were synthesized via the citric acid-EDTA route. The crystal structures of the compounds were determined via XRD and Rietveld refinement. In addition, the electronic conductivity, chemical surface exchange coefficient and chemical diffusion coefficient of oxygen were determined as functions of temperature and oxygen partial pressures at conditions relevant for operation in solid oxide cells. The effect of the Co/Fe substitution in these HEPs is highlighted and the material properties are compared with their state-of-the-art low-entropy analogs.

At room temperature, all compounds exhibit an orthorhombic lattice distortion consistent with space group 62 (*Pnma*). Compared to low-entropy lanthanum cobaltates or ferrates with the

same Sr content, the lattice parameters and unit cell volumes of the HEPs are slightly smaller, which is caused by the lower ionic radii of the additional A-site dopants Pr, Nd and Sm as compared to La. The highest electronic conductivity is found for $La_{0.2}Pr_{0.2}Nd_{0.2}Sm_{0.2}Sr_{0.2}CoO_{3-\delta}$ (LPNSSC) with a maximum of 1660 S cm$^{-1}$ at 600°C and 0.15 bar $pO_2$. It surpasses the conductivity of $La_{0.8}Sr_{0.2}CoO_{3-\delta}$ at the same temperature and oxygen partial pressure by approximately 200 S cm$^{-1}$. Substitution of Co with Fe reduces the electronic conductivity, which falls below 100 S cm$^{-1}$ for the high-entropy ferrate $La_{0.2}Pr_{0.2}Nd_{0.2}Sm_{0.2}Sr_{0.2}FeO_{3-\delta}$ (LPNSSF). The chemical diffusion coefficients of oxygen ($D_{chem}$) range from $7 \times 10^{-7}$ to $1 \times 10^{-5}$ cm$^2$ s$^{-1}$ between 650 and 850°C and show no dependence on the Fe/Co ratio or the oxygen partial pressure. The chemical surface exchange coefficients ($k_{chem}$) do increase significantly with increasing Co content, demonstrating the catalytic effect of cobalt on the surface exchange kinetics. For LPNSSC, $k_{chem}$ reaches $7.7 \times 10^{-4}$ cm s$^{-1}$ at 800°C and $10^{-3}$ bar $pO_2$, which is an increase by more than a factor of 20 compared to LPNSSF ($3.4 \times 10^{-5}$ cm s$^{-1}$). The diffusivities and the surface exchange coefficients of the HEPs are the same order of magnitude as for state-of-the-art perovskites with 20% Sr at the A-site (e.g. $La_{0.8}Sr_{0.2}CoO_{3-\delta}$ or $La_{0.8}Sr_{0.2}FeO_{3-\delta}$).

In conclusion, the investigated high entropy perovskites show good electronic conductivity, high oxygen diffusivities as well as fast surface oxygen exchange kinetics and are therefore promising materials for application in solid oxide cell air electrodes. Although the fundamental material parameters are quite similar to conventional low-entropy perovskites from the $(La,Sr)(Co,Fe)O_{3-\delta}$ series, the HEPs may offer the benefits of increased long-term stability under application-relevant conditions [13,15,64-66].

## CRediT authorship contribution statement

**P. Pretschuh:** Investigation, Visualization, Validation, Writing – Original Draft.

**A. Egger:** Investigation, Validation, Writing – Review & Editing.

**E. Bucher:** Conceptualization, Validation, Writing – Review & Editing, Supervision, Project administration, Funding acquisition.

## Acknowledgments

## References

[1]     A. Niemczyk, K. Świerczek, E3S Web of Conferences 108 (2019) 01019. https://doi.org/10.1051/e3sconf/201910801019.

[2]     S.E. Wolf, F.E. Winterhalder, V. Vibhu, L.B. de Haart, O. Guillon, R.-A. Eichel, N.H. Menzler, Journal of Materials Chemistry A 11 (2023) 17977-18028. https://doi.org/10.1039/D3TA02161K.

[3]     H. Kozuka, K. Ohbayashi, K. Koumoto, Science and Technology of Advanced Materials 16 (2015) 026001. https://doi.org/10.1088/1468-6996/16/2/026001.

[4]     E.P. George, D. Raabe, R.O. Ritchie, Nature Reviews Materials 4 (2019) 515-534. https://doi.org/10.1038/s41578-019-0121-4.

[5]     Y.F. Ye, Q. Wang, J. Lu, C.T. Liu, Y. Yang, Materials Today 19 (2016) 349-362. https://doi.org/10.1016/j.mattod.2015.11.026.

[6]     C.M. Rost, E. Sachet, T. Borman, A. Moballegh, E.C. Dickey, D. Hou, J.L. Jones, S. Curtarolo, J.-P. Maria, Nature Communications 6 (2015) 8485. https://doi.org/10.1038/ncomms9485.

[7]     A. Sarkar, L. Velasco, D. Wang, Q. Wang, G. Talasila, L. de Biasi, C. Kübel, T. Brezesinski, S.S. Bhattacharya, H. Hahn, B. Breitung, Nature Communications 9 (2018) 3400. https://doi.org/10.1038/s41467-018-05774-5.

[8]     P.A. Krawczyk, M. Jurczyszyn, J. Pawlak, W. Salamon, P. Baran, A. Kmita, Ł. Gondek, M. Sikora, C. Kapusta, T. Strączek, J. Wyrwa, A. Żywczak, ACS Applied Electronic Materials 2 (2020) 3211-3220. https://doi.org/10.1021/acsaelm.0c00559.

[9]     A. Sarkar, Q. Wang, A. Schiele, M.R. Chellali, S.S. Bhattacharya, D. Wang, T. Brezesinski, H. Hahn, L. Velasco, B. Breitung, Advanced Materials 31 (2019) 1806236. https://doi.org/10.1002/adma.201806236.

[10]    H. Nan, S. Lv, Z. Xu, Y. Feng, Y. Zhou, M. Liu, T. Wang, X. Liu, X. Hu, H. Tian, Chemical Engineering Journal 452 (2023) 139501. https://doi.org/10.1016/j.cej.2022.139501.

[11]    W.-L. Hsu, C.-W. Tsai, A.-C. Yeh, J.-W. Yeh, Nature Reviews Chemistry (2024) https://doi.org/10.1038/s41570-024-00602-5.

[12]    V. Prabhahari, R. Praveena, K.S. Babu, Journal of Alloys and Compounds 986 (2024) 174152. https://doi.org/10.1016/j.jallcom.2024.174152.

[13]    P. Pretschuh, A. Egger, R. Brunner, E. Bucher, Fuel Cells 23 (2023) 377–386. https://doi.org/10.1002/fuce.202300036.

[14]    L. Shen, Z. Du, Y. Zhang, X. Dong, H. Zhao, Applied Catalysis B: Environmental 295 (2021) 120264. https://doi.org/10.1016/j.apcatb.2021.120264.

[15]    P. Pretschuh, A. Egger, P. Paulachan, J. Schöggl, R. Brunner, E. Bucher, Fuel Cells (2024) accepted for publication. https://doi.org/10.1002/fuce.202400068.

[16]    L.J. van der Pauw, Philips Research Reports 13 (1958) 1-9.

[17] W. Preis, M. Holzinger, W. Sitte in: J.O. Besenhard, W. Sitte, F. Stelzer, H. Gamsjäger (Eds.), Electroactive Materials, Springer Vienna, 2001, p. 79-88.

[18] K. Momma, F. Izumi, Journal of Applied Crystallography 44 (2011) 1272-1276. https://doi.org/10.1107/S0021889811038970.

[19] M.W. den Otter, H.J.M. Bouwmeester, B.A. Boukamp, H. Verweij, Journal of the Electrochemical Society 148 (2001) J1. https://doi.org/10.1149/1.1337604.

[20] H.J.M. Bouwmeester, H. Kruidhof, A.J. Burggraaf, Solid State Ionics 72 (1994) 185-194. https://doi.org/10.1016/0167-2738(94)90145-7.

[21] Y. Wang, Y. Sui, P. Ren, L. Wang, X. Wang, W. Su, H.J. Fan, Inorganic Chemistry 49 (2010) 3216-3223. https://doi.org/10.1021/ic902072v.

[22] A. Nadeev, S. Tsybulya, A. Shmakov, G. Kryukova, I. Yakovleva, L. Isupova, Journal of Structural Chemistry 48 (2007) 1105-1109. https://doi.org/10.1007/s10947-007-0177-7.

[23] R. Shannon, Acta Crystallographica Section A 32 (1976) 751-767. https://doi.org/10.1107/S0567739476001551.

[24] Y.Q. Jia, Journal of Solid State Chemistry 95 (1991) 184-187. https://doi.org/10.1016/0022-4596(91)90388-X.

[25] V.M. Goldschmidt, Die Naturwissenschaften 14 (1926) 477-485. https://doi.org/10.1007/BF01507527.

[26] W. Yang, Z. Han, G. Zheng, Scripta Materialia 203 (2021) 114096. https://doi.org/10.1016/j.scriptamat.2021.114096.

[27] L. Su, H. Huyan, A. Sarkar, W. Gao, X. Yan, C. Addiego, R. Kruk, H. Hahn, X. Pan, Nature Communications 13 (2022) 2358. https://doi.org/10.1038/s41467-022-30018-y.

[28] V.G. Sathe, S.K. Paranjpe, V. Siruguri, A.V. Pimpale, Journal of Physics: Condensed Matter 10 (1998) 4045. https://doi.org/10.1088/0953-8984/10/18/014.

[29] A.N. Petrov, O.F. Kononchuk, A.V. Andreev, V.A. Cherepanov, P. Kofstad, Solid State Ionics 80 (1995) 189-199. https://doi.org/10.1016/0167-2738(95)00114-L.

[30] T. Bak, J. Nowotny, M. Rekas, S. Ringer, C.C. Sorrell, Ionics 7 (2001) 388-393. https://doi.org/10.1007/BF02373574.

[31] L.W. Tai, M.M. Nasrallah, H.U. Anderson, D.M. Sparlin, S.R. Sehlin, Solid State Ionics 76 (1995) 259-271. https://doi.org/10.1016/0167-2738(94)00244-M.

[32] J. Mizusaki, J. Tabuchi, T. Matsuura, S. Yamauchi, K. Fueki, Journal of the Electrochemical Society 136 (1989) 2082. https://doi.org/10.1149/1.2097187.

[33] Y. Teraoka, H.M. Zhang, K. Okamoto, N. Yamazoe, Materials Research Bulletin 23 (1988) 51-58. https://doi.org/10.1016/0025-5408(88)90224-3.

[34] C. Sun, R. Hui, J. Roller, Journal of Solid State Electrochemistry 14 (2010) 1125-1144. http://dx.doi.org/10.1007/s10008-009-0932-0.

[35] R.J.D. Tilley, Defects in solids, John Wiley & Sons, Inc., Hoboken, New Jersey, 2008.

[36] A. Egger, E. Bucher, M. Yang, W. Sitte, Solid State Ionics 225 (2012) 55-60. https://doi.org/10.1016/j.ssi.2012.02.050.

[37] J. Mizusaki, M. Yoshihiro, S. Yamauchi, K. Fueki, Journal of Solid State Chemistry 58 (1985) 257-266. https://doi.org/10.1016/0022-4596(85)90243-9.

[38] E. Bucher, W. Sitte, G.B. Caraman, V.A. Cherepanov, T.V. Aksenova, M.V. Ananyev, Solid State Ionics 177 (2006) 3109-3115. https://doi.org/10.1016/j.ssi.2006.07.062.

[39] W. Sitte, E. Bucher, A. Benisek, W. Preis, Spectrochimica Acta A 57 (2001) 2071-2076. https://doi.org/10.1016/S1386-1425(01)00489-9.

[40] W. Sitte, E. Bucher, W. Preis, Solid State Ionics 154-155 (2002) 517-522. https://doi.org/10.1016/S0167-2738(02)00503-9.

[41] M.V. Patrakeev, I.A. Leonidov, E.B. Mitberg, A.A. Lakhtin, V.G. Vasiliev, V.L. Kozhevnikov, K.R. Poeppelmeier, Ionics 5 (1999) 444-449. https://doi.org/10.1007/BF02376011.

[42] H.J.M. Bouwmeester, M.W. Den Otter, B.A. Boukamp, Journal of Solid State Electrochemistry 8 (2004) 599-605. https://doi.org/10.1007/s10008-003-0488-3.

[43] L.M. van der Haar, M.W. den Otter, M. Morskate, H.J.M. Bouwmeester, H. Verweij, Journal of the Electrochemical Society 149 (2002) J41. https://doi.org/10.1149/1.1446874.

[44] J.A. Lane, J.A. Kilner, Solid State Ionics 136-137 (2000) 997-1001. https://doi.org/10.1016/S0167-2738(00)00554-3.

[45] M. Sahibzada, W. Morton, A. Hartley, D. Mantzavinos, I.S. Metcalfe, Solid State Ionics 136-137 (2000) 991-996. https://doi.org/10.1016/S0167-2738(00)00517-8.

[46] W. Preis, E. Bucher, W. Sitte, Solid State Ionics 175 (2004) 393-397. https://doi.org/10.1016/j.ssi.2003.12.045.

[47] J.E. ten Elshof, M.H.R. Lankhorst, H.J.M. Bouwmeester, Journal of the Electrochemical Society 144 (1997) 1060. https://doi.org/10.1149/1.1837531.

[48] J. Yoo, A. Verma, S. Wang, A.J. Jacobson, Journal of the Electrochemical Society 152 (2005) A497. https://doi.org/10.1149/1.1854617.

[49] M. Søgaard, P.V. Hendriksen, F.W. Poulsen, M. Mogensen, Journal of Electroceramics 13 (2004) 811-816. https://doi.org/10.1007/s10832-004-5197-5.

[50] H. Bae, B. Singh, I.-H. Kim, H.-N. Im, S.-J. Song, Journal of the Electrochemical Society 165 (2018) F641. https://doi.org/10.1149/2.0771809jes.

[51] E. Bucher, W. Sitte, Solid State Ionics 173 (2004) 23-28. https://doi.org/10.1016/j.ssi.2004.07.047.

[52] R.H.E. van Doorn, A.J. Burggraaf, Solid State Ionics 128 (2000) 65-78. https://doi.org/10.1016/S0167-2738(99)00282-9.

[53] E. Bucher, A. Benisek, W. Sitte, Solid State Ionics 157 (2003) 39-44. https://doi.org/10.1016/S0167-2738(02)00187-X.

[54] S. Wang, A. Verma, Y.L. Yang, A.J. Jacobson, B. Abeles, Solid State Ionics 140 (2001) 125-133. https://doi.org/10.1016/S0167-2738(01)00709-3.

[55] R. Merkle, J. Maier, Physical Chemistry Chemical Physics 4 (2002) 4140-4148. https://doi.org/10.1039/B204032H .

[56] E. Bucher, G.B. Caraman, A. Egger, W. Sitte, Proc. 8th European Solid Oxide Fuel Cell Forum, edited by R. Steinberger-Wilckens, Lucerne, Switzerland (2008) p. A0406.

[57] E. Bucher, W. Sitte, Solid State Ionics 192 (2011) 480-482. http://dx.doi.org/10.1016/j.ssi.2010.01.006.

[58] A. Egger, E. Bucher, W. Sitte, Journal of the Electrochemical Society 158 (2011) B573-B579. http://dx.doi.org/10.1149/1.3569697.

[59] E. Bucher, W. Sitte, F. Klauser, E. Bertel, Solid State Ionics 208 (2012) 43-51. http://dx.doi.org/10.1016/j.ssi.2011.12.005.

[60] E. Bucher, C. Gspan, F. Hofer, W. Sitte, Solid State Ionics 238 (2013) 15-23. https://doi.org/10.1016/j.ssi.2013.03.007.

[61] C.C. Wang, T. Becker, K. Chen, L. Zhao, B. Wei, S.P. Jiang, Electrochimica Acta 139 (2014) 173-179. http://dx.doi.org/10.1016/j.electacta.2014.07.028.

[62] Đ. Tripković, R. Küngas, M.B. Mogensen, P.V. Hendriksen, Journal of Materials Chemistry A (2019) http://dx.doi.org/10.1039/C9TA02607J.

[63] W. Preis, E. Bucher, W. Sitte, Journal of Power Sources 106 (2002) 116-121. https://doi.org/10.1016/S0378-7753(01)01036-9.

[64] Y. Yang, H. Bao, H. Ni, X. Ou, S. Wang, B. Lin, P. Feng, Y. Ling, Journal of Power Sources 482 (2021) 228959. https://doi.org/10.1016/j.jpowsour.2020.228959.

[65] F. He, F. Zhu, D. Liu, Y. Zhou, K. Sasaki, Y. Choi, M. Liu, Y. Chen, Materials Today 63 (2023) 89-98. https://doi.org/10.1016/j.mattod.2023.02.006.

[66] L. Chunjiao, S. Liping, L. Qiang, H. Lihua, Z. Hui, Journal of Electroanalytical Chemistry 941 (2023) 117546. https://doi.org/10.1016/j.jelechem.2023.117546.

# Supplementary Material

**Crystal structure, electronic conductivity and oxygen exchange kinetics of high-entropy perovskites La$_{0.2}$Pr$_{0.2}$Nd$_{0.2}$Sm$_{0.2}$Sr$_{0.2}$Co$_{1-x}$Fe$_x$O$_{3-δ}$ (x = 0, 0.5, 1)**

Patrick Pretschuh, Andreas Egger, Edith Bucher

Montanuniversitaet Leoben, Chair of Physical Chemistry, Franz-Josef-Straße 18, AT-8700 Leoben, Austria

Tab. S-1. Atomic positions and bond lengths of $La_{0.2}Pr_{0.2}Nd_{0.2}Sm_{0.2}Sr_{0.2}Co_{1-x}Fe_xO_{3-\delta}$ (x = 0, 0.5, 1) obtained by XRD and Rietveld refinement.

| | x | y | z | Co-O1/Å | Co-O2/Å |
|---|---|---|---|---|---|
| **LPNSSC (x = 0)** | | | | | |
| La/Pr/Nd/Sm/Sr | 0.47827 | 0.25 | 0.00008 | | |
| Co | 0 | 0 | 0 | 1.92834(3) | 1.87356(0) |
| O1 | 0.00485 | 0.25 | 0.06013 | | |
| O2 | 0.25699 | -0.02855 | 0.23123 | | |

| | x | y | z | Co/Fe-O1/Å | Co/Fe-O2/Å |
|---|---|---|---|---|---|
| **LPNSSCF (x = 0.5)** | | | | | |
| La/Pr/Nd/Sm/Sr | 0.47451 | 0.025 | -0.00188 | | |
| Co/Fe | 0 | 0 | 0 | 1.95076(0) | 1.88301(0) |
| O1 | 0.00885 | 0.25 | 0.06013 | | |
| O2 | 0.28113 | -0.03373 | 0.23656 | | |

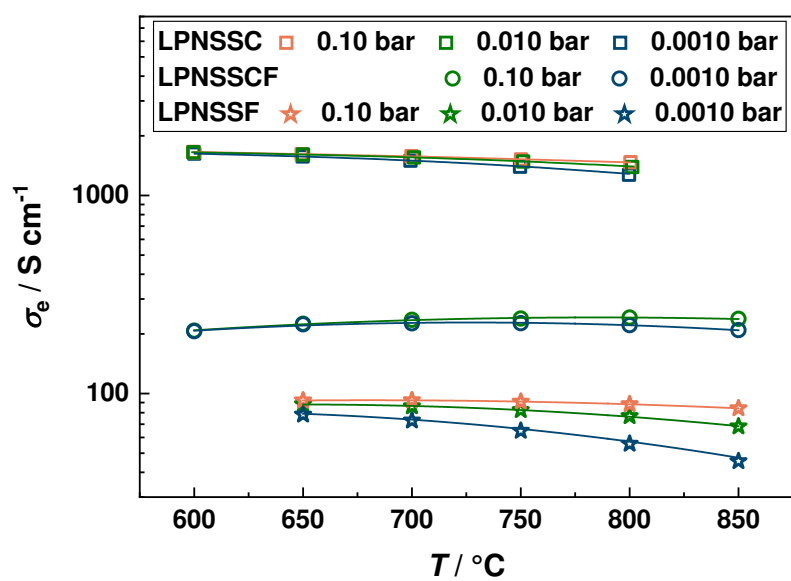| | x | y | z | Fe-O1/Å | Fe-O2/Å |
|---|---|---|---|---|---|
| **LPNSSF (x = 1)** | | | | | |
| La/Pr/Nd/Sm/Sr | 0.46743 | 0.25 | -0.00538 | | |
| Fe | 0 | 0 | 0 | 1.98466(0) | 1.96418(0) |
| O1 | 0.01213 | 0.25 | 0.07169 | | |
| O2 | 0.28103 | -0.04125 | 0.22434 | | |

Fig. S-1. Electronic conductivity of LPNSSC, LPNSSCF and LPNSSF at different temperatures and oxygen partial pressures. Lines are a guide to the eye.
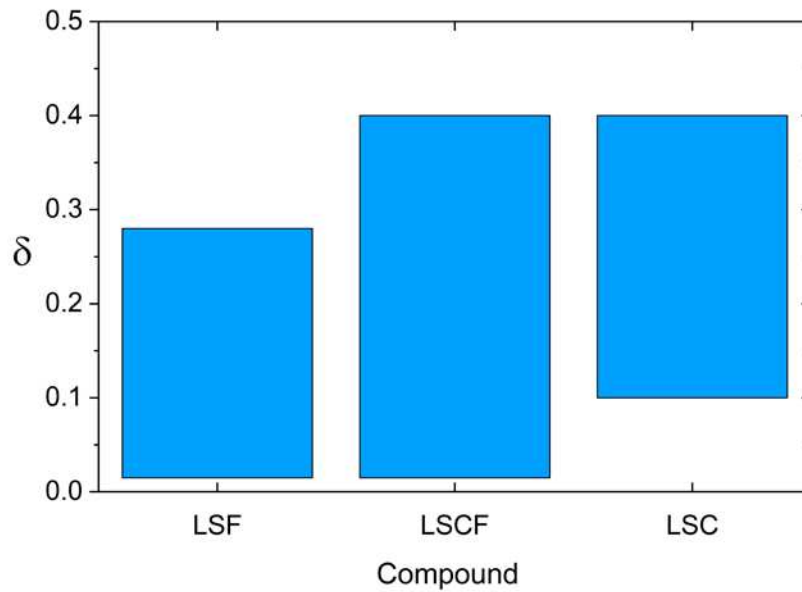
Fig. S-2. Oxygen nonstoichiometry of low-entropy perovskites $(La,Sr)FeO_{3-\delta}$ (LSF) [1,2], $(La,Sr)(Co,Fe)O_{3-\delta}$ (LSCF) [3-5] and $(La,Sr)CoO_{3-\delta}$ (LSC) [6,7] at $10^{-5} < pO_2$ / bar < 1 and 600-900°C.
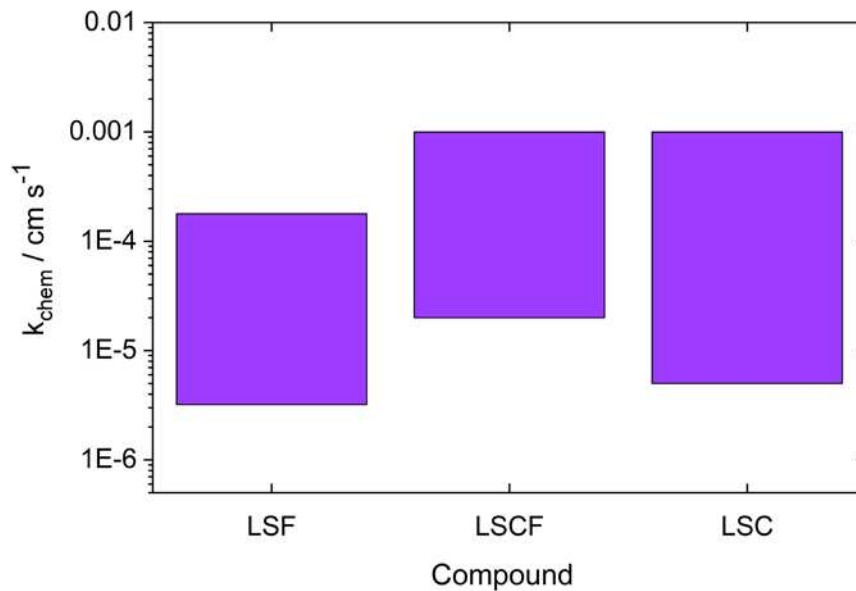


Fig. S-3. Chemical oxygen surface exchange coefficients of low-entropy perovskites $(La,Sr)FeO_{3-\delta}$ (LSF) [8,9], $(La,Sr)(Co,Fe)O_{3-\delta}$ (LSCF) [10,11] and $(La,Sr)CoO_{3-\delta}$ (LSC) [7,12-14] at $10^{-3} < pO_2$ / bar < $10^{-1}$ and 700-725°C.

## References

[1] J. Mizusaki, M. Yoshihiro, S. Yamauchi, K. Fueki, Journal of Solid State Chemistry 58 (1985) 257-266. https://doi.org/10.1016/0022-4596(85)90243-9.

[2] E. Bucher, W. Sitte, Solid State Ionics 173 (2004) 23-28. https://doi.org/10.1016/j.ssi.2004.07.047.

[3] E. Bucher, W. Sitte, G.B. Caraman, V.A. Cherepanov, T.V. Aksenova, M.V. Ananyev, Solid State Ionics 177 (2006) 3109-3115. https://doi.org/10.1016/j.ssi.2006.07.062.

[4] W. Sitte, E. Bucher, A. Benisek, W. Preis, Spectrochimica Acta A 57 (2001) 2071-2076. https://doi.org/10.1016/S1386-1425(01)00489-9.

[5] L.-W. Tai, M.M. Nasrallah, H.U. Anderson, D.M. Sparlin, S.R. Sehlin, Solid State Ionics 76 (1995) 273-283. https://doi.org/10.1016/0167-2738(94)00245-N.

[6] M.V. Patrakeev, I.A. Leonidov, E.B. Mitberg, A.A. Lakhtin, V.G. Vasiliev, V.L. Kozhevnikov, K.R. Poeppelmeier, Ionics 5 (1999) 444-449. https://doi.org/10.1007/BF02376011.

[7] A. Egger, E. Bucher, M. Yang, W. Sitte, Solid State Ionics 225 (2012) 55-60. http://dx.doi.org/10.1016/j.ssi.2012.02.050.

[8] J.E. ten Elshof, M.H.R. Lankhorst, H.J.M. Bouwmeester, J. Electrochem. Soc. 144 (1997) 1060-1067. https://doi.org/10.1149/1.1837531.

[9] W. Preis, E. Bucher, W. Sitte, Solid State Ionics 175 (2004) 393-397. https://doi.org/10.1016/j.ssi.2003.12.045.

[10] E. Bucher, G.B. Caraman, A. Egger, W. Sitte, Proc. 8th European Solid Oxide Fuel Cell Forum, edited by R. Steinberger-Wilckens, Lucerne, Switzerland (2008) p. A0406.

[11] E. Bucher, W. Sitte, Solid State Ionics 192 (2011) 480-482. http://dx.doi.org/10.1016/j.ssi.2010.01.006.

[12] W. Preis, E. Bucher, W. Sitte, J. Power Sources 106 (2002) 116-121. https://doi.org/10.1016/S0378-7753(01)01036-9.

[13] W. Sitte, E. Bucher, W. Preis, Solid State Ionics 154-155 (2002) 517-522. https://doi.org/10.1016/S0167-2738(02)00503-9.

[14] A. Egger, E. Bucher, W. Sitte, Journal of the Electrochemical Society 158 (2011) B573-B579. http://dx.doi.org/10.1149/1.3569697.